DISSERTAÇÂO DE MESTRADO Nº:1115

POWER CONTROL STRATEGIES FOR GRID-CONNECTED CONVERTERS DURING LOW VOLTAGE RIDE THROUGH OPERATION

Rafael Mario da Silva

DATA DA DEFESA: 22/02/2019

UNIVERSIDADE FEDERAL DE MINAS GERAIS - UFMG

ESCOLA DE ENGENHARIA

PROGRAMA DE PÓS GRADUAÇÃO EM ENGENHARIA ELÉTRICA

POWER CONTROL STRATEGIES FOR GRID-CONNECTED CONVERTERS DURING LOW VOLTAGE RIDE THROUGH OPERATION

Rafael Mario da Silva.

Dissertação de mestrado submetido à Banca Examinadora designada pelo Colegiado do Programa de Pós-Graduação em Engenharia Elétrica da Escola de Engenharia da Universidade Federal de Minas Gerais, como requisito para obtenção do Título de Mestre em Engenharia Elétrica.

Orientador: Prof. Dr. Victor Flores Mendes.
Coorientador: Prof. Dr. Clodualdo V. de Sousa

Belo Horizonte, fevereiro de 2019.

Silva, Rafael Mario da.
S586p Power control strategies for grid-connected converters during low voltage ride through [manuscrito] / Rafael Mario da Silva. - 2019.
xiii, 104 f., enc.: il.

Orientador: Victor Flores Mendes.
Coorientador: Clodualdo Venicio de Sousa.

Dissertação (mestrado) Universidade Federal de Minas Gerais, Escola de Engenharia.

Apêndices: f.91 – 104.

Bibliografia: f. 86 – 90.

1. Engenharia elétrica - Teses. 2. Fator de potência - Teses. 3. Conversores de corrente elétrica - Teses. I. Mendes, Victor Flores. II. Sousa, Clodualdo Venicio de. III. Universidade Federal de Minas Gerais. Escola de Engenharia. IV. Título.

CDU:621.3(043)

Acknowledgements

First, I would like to thank my family, especially my mother Edilene for her great support and patient during my graduation and the post-graduation studies.

I also would like to thank:

The researchers who had a directly participation in this work, Professor Dr. Victor Flores and Clodualdo Sousa (master's supervisors) by the great support and guidance, Professors Allan Fagner and Guilherme Monteiro by the immensurable contributions in the elaboration of this work;

The lords of power electronics from UNIFEI-Itabira, the Professors Waner Wodson, João Lucas, Frederico Matos, Tiago Sá, Geovane Reis and Eben Ezer the master's students Moisés Martins, Luis Guedes, Camilo Lellis for the great support and friendship;

All my graduation friends and classmates from UNIFEI and the Post-Graduation at UFMG my Student Republic fellows Lucas Santana, André Badaia and José and my Laboratory partners Modesto Teixeira, Mauricio, Hugo and Igor;

My Graduation and Post-Graduation professors especially to the Dr. Clodualdo Sousa and Dr. Frederico Matos.

Finally, I would like to thank you, who are reading this master's thesis, I hope it is useful to meet the objectives are you looking for

The knowledge must be shared and used in the elaboration of something greater to the construction of a better word.

"42"

Deep Thought - The Hitchhiker's Guide to the Galaxy

Resumo

Afundamentos momentâneos de tensão são fenômenos muito recorrentes em redes elétricas. Assim, os operadores do sistema elétrico exigem que as unidades geradoras permaneçam conectadas ao sistema de transmissão enquanto a tensão estiver dentro dos valores definidos pelos códigos de rede, evitando a perda súbita de grandes blocos de energia.

Além da não desconexão, os códigos de rede atuais estabelecem que os geradores eólicos e fotovoltaicos auxiliem na recuperação da tensão através da injeção de corrente reativa de sequência positiva, aumentando a tensão no ponto de acoplamento comum. Os conversores eletrônicos possuem uma maior flexibilidade no controle de corrente em relação às máquinas síncronas convencionais possibilitando, por exemplo, sintetizar correntes desbalanceadas ou com componentes harmônicas específicas. Logo, o cálculo das correntes de referência pode ser modificado para atenuar outros problemas de qualidade da energia, durante a ocorrência de faltas.

O presente trabalho avalia diferentes técnicas de controle de potência, ou seja, formas de calcular os valores de referência de corrente para injetar determinados valores de potência, com foco em sistemas trifásicos a três fios. Onde as mesmas serão comparadas com relação à oscilação de potência e perfil de corrente, de modo a estudar como estas estratégias podem atenuar os efeitos do afundamento para o conversor, reduzindo a flutuação de tensão e o ripple de corrente nos capacitores do barramento c.c.. Além disso, é investigado como estas estratégias afetam o suporte de tensão no ponto de acoplamento comum. Desta forma, são propostos equacionamentos que embasam as análises realizadas, onde as mesmas são validadas através de simulações computacionais. Dois estudos de caso são realizados, o primeiro de um sistema de geração eólico de 2(MW) para avaliar os efeitos para o conversor e o segundo de uma planta de geração de 118(MW) que possibilite investigar o suporte de tensão no ponto de conexão da usina.

Palavras chave: afundamentos de tensão, conversores eletrônicos de potência, injeção de corrente reativa, qualidade da energia, suporte de tensão, *voltage ride through*.

Abstract

Momentary voltage sags are very common phenomena in electrical power systems. Thus, the transmission system operators require that the generation units remain connected to the transmission mains while the voltage is within the values outlined by the grid codes, preventing the sudden loss of large generation energy blocks.

In addition to non-disconnection, the current grid codes establish that wind and photovoltaic generators must assist in the voltage recovery through the positive sequence reactive current injection, increasing the positive sequence voltage at the point of common coupling. Grid-connected converters have greater current control flexibility in relation to conventional synchronous machines allowing, for example, unbalanced currents synthesize or with specific harmonic components. Hence, the calculation of reference currents can be modified to mitigate other quality issues during the fault occurrence.

The present work evaluates different power control strategies, i.e., the calculus of the reference currents values for injecting certain power set-points, focusing on three-phase three-wire systems. Where they will be compared in relation to the power oscillation and currents profiles, in order to study how these strategies can attenuate the effects of the voltage sags to the grid converters, reducing the voltage fluctuation and current ripple in the d.c. bus capacitors. In addition, is investigated how these strategies affect the voltage support at the point of common coupling. For this, equations, that are the basis of the analysis, are proposed, and they are validated through computational simulations. Two case studies are performed, the first one of a 2(MW) wind energy conversion system, to evaluate the impacts to the grid-connected converter and the second one of a 118(MW) generation plant to investigate the voltage support at the point of common coupling.

Keywords: grid-connected converters, power quality, reactive current injection, voltage sag,, voltage support, voltage ride through.

Figure list

Table list

List of acronyms

PV	Photovoltaic
GC	Grid Codes
TSO	Transmission System Operator
GU	Generating Units
WEC	Wind Energy Conversion System
RCI	Reactive Current Injection
RPP	Renewable Power Plant
PCC	Point of Common Coupling
POC	Point of Connection
PGC	Point of Generator Connection
GSC	Grid Side Converter
MSC	Machine Side Converter
LVRT	Low-voltage Ride Through
DFIG	Doubly-Fed Induction Generators
MPPT	Maximum Power Point Tracking
HVDC	High Voltage Direct Current
PLL	Phase Locked Loop
FLL	Frequency Locked Loop.
PR	Proportional Resonant Controller
PWM	Pulse Width Modulation
HVDC	High Voltage Direct Current
IARC	Instantaneous Active and Reactive Control
ICPS	Instantaneously Controlled Positive Sequence
AARC	Average Active and Reactive Control
PNSC	Positive and Negative Sequence Compensation
APOC	Active Power Cancellation
RPOC	Reactive Power Cancellation
FPNSC	Flexible Positive Negative Sequence Control
PARPC	Pliant Active and Reactive Power Control
GFPC	Generalized Flexible Power Control

Summary

Chapter I

INTRODUCTION

ONE of the main requirements for the integration of renewable power sources to the electrical mains is the voltage ride through capability, i.e., the ability to remain connected to the grid during the voltage transients, and it is the focus of this work. In this chapter is presented the motivations and objectives of this thesis. For this, a contextualization of the voltage ride through requirements in different countries is presented, and the main aspects about this subject in the technical literature are addressed.

1.1 Renewable power integration scenario

In the last decades, several countries around the world have been applying alternative sources to diversify and consequently decrease the dependence on fossil fuels, amortizing the operational costs and environmental impacts. Due to the reduction of the implementation costs, continuous technological advances and resources availability, wind energy conversion (WEC) and photovoltaic (PV) systems, have grown in recent years [1]. Fig. 1.1 presents the evolution of wind and PV power plants in comparison to the nonrenewable thermoelectric in Brazil (Fig. 1.1(a)), Denmark (Fig. 1.1(b)), Deutschland (Fig. 1.1(c)) and Spain (Fig. 1.1(d)), respectively. The data series refer from 2007 to 2017 and the percentage values related to the total generated power in that year.

Despite the economic and environmental benefits, the seasonal and stochastic generation pattern make that high rates of renewable sources penetration, entails negative impacts on the electrical power system since, according to [2], the dispatchable generation will be subjected to additional ramps (quick changes in generator power output), cycling (powering down and up in short-time periods), and others operational difficulties called "flexibility requirements" in order to equalize the load and generation balancing, reducing the quality and stability of grid voltage and frequency.

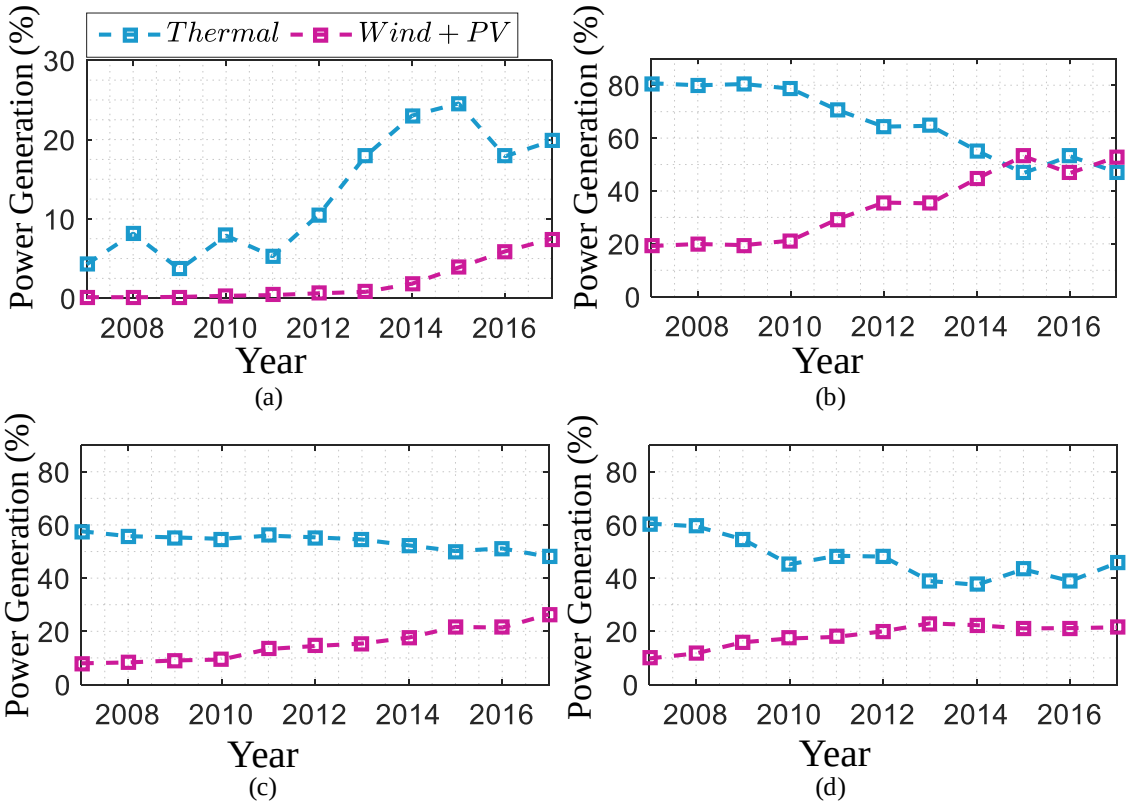

Fig. 1.1: Comparison of different energy sources evolution (a) Brazil, (b) Danish, (c) Deutschland and (d) Spain.
Source: Data obtained from [3–6]

1.2 Grid codes requirements for wind and photovoltaic power systems

The flexible requirements problems previously related in relation to the renewable sources integration have led the transmission systems operators (TSOs) to elaborate more specific and restrictive technical requirements [7]. Different from the conventional power plants that use synchronous machines, variable speed wind turbines and photovoltaic generators employ power electronics converters to perform the conditioning and control of the generated energy, and the actual grid codes (GCs) demand that PV and WEC generating units, behave as similar as possible to the conventional power plants (synchronous machines), requiring for example, extended voltage and frequency variation limits, active power/frequency regulation, reactive power/voltage regulation and fault ride through capability [7,8].

Momentary voltage sag (or voltage dip) is a sudden reduction in the voltage magnitude for a short-time period, and it is a very common transient phenomenon in the electrical power systems. For that reason, it is one of the main aspects approached by the GCs.

1.2.1 Voltage ride through and reactive current injection

The operation during the occurrence of momentary voltage sags, while the voltage magnitude is within the values defined by the grid codes, is known as low-voltage ride through (LVRT). References [9–12] present the GCs requirements of different countries and they establish that the generating units (GUs) must remain connected to the transmission system, as long as the voltage are above the values outlined by the curves in Fig. 1.2, where V_n is the nominal voltage. This requirement aims to avoid the sudden loss of a large set of generating units during voltage transients, reducing the possibility of the electrical mains collapse.

The voltage ride through described in Tennet (Deutschland) GC [11] define two limits. Faults above the limit line 1 must not lead to GU disconnection. When the voltage drops between the limit line 1 and 2, in case of GU instability, it is allowed short time disconnection from the mains. Nevertheless, the GU resynchronization must take place at least 2 seconds. The limit line 2 is the most restrictive situation analyzed in this work, the power plant must withstand voltages drops down to 0(pu) for duration up to 150(ms) (7.5 cycle). A disconnection of the generating plant is always allowed bellow the limit line 2.

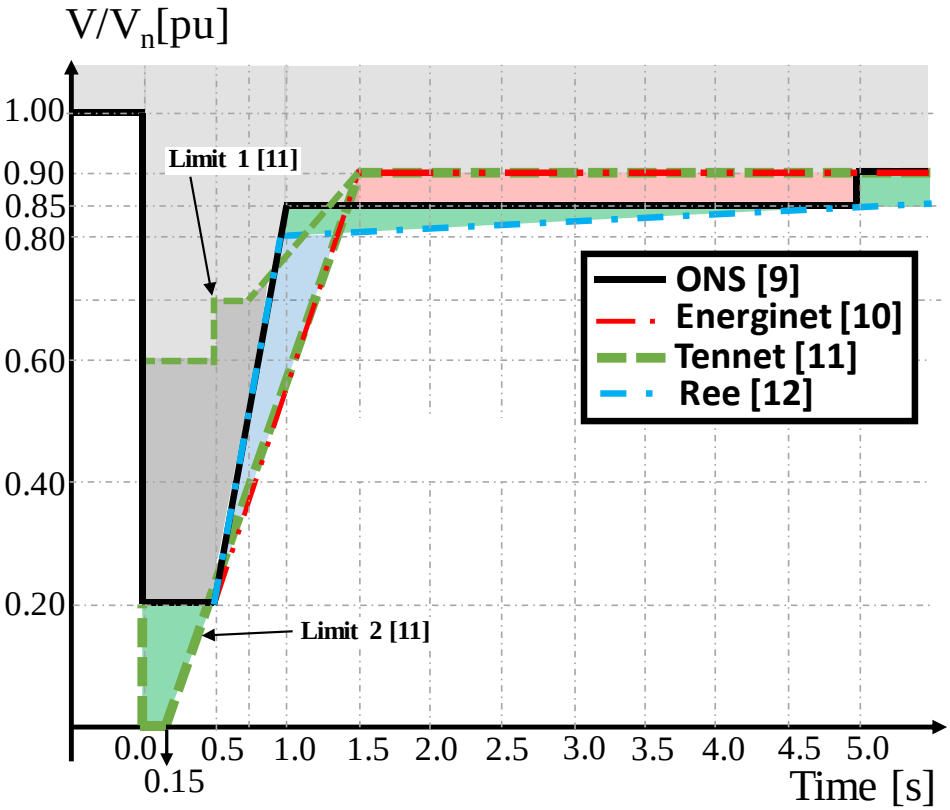

Fig. 1.2: Voltage sag tolerance requirement for different grid codes.
Source: Adapted from [9–12]

Regarding to the voltage values (y-axis), ONS (Brazil) and Ree (Spain) [9,12] denotes to the phase-to-ground voltage that undergoes the greatest variation, Energinet (Denmark) [10] refers to the smallest and Tennet [11] to the highest phase-to-phase grid voltage.

In addition to the non-disconnection, the PV and WEC units connected to the transmission system must support the mains by means additional positive sequence reactive current injection (RCI) (ΔI_Q), as shown in Fig. 1.3, where I_N is the converter nominal current. The RCI increase the positive sequence voltage at the point of common coupling and helping to avoid the GU disconnection. The y-axis denotes the fundamental component reactive current magnitude and x-axis the positive sequence voltage drop [9–12]. The grid support though reactive current feed-in, must be the priority and the active power production may be reduced during the transient phenomena. Moreover, it is a TSO responsibility to define the RCI curve slope, depending on the system characteristic where the power plant is connected.

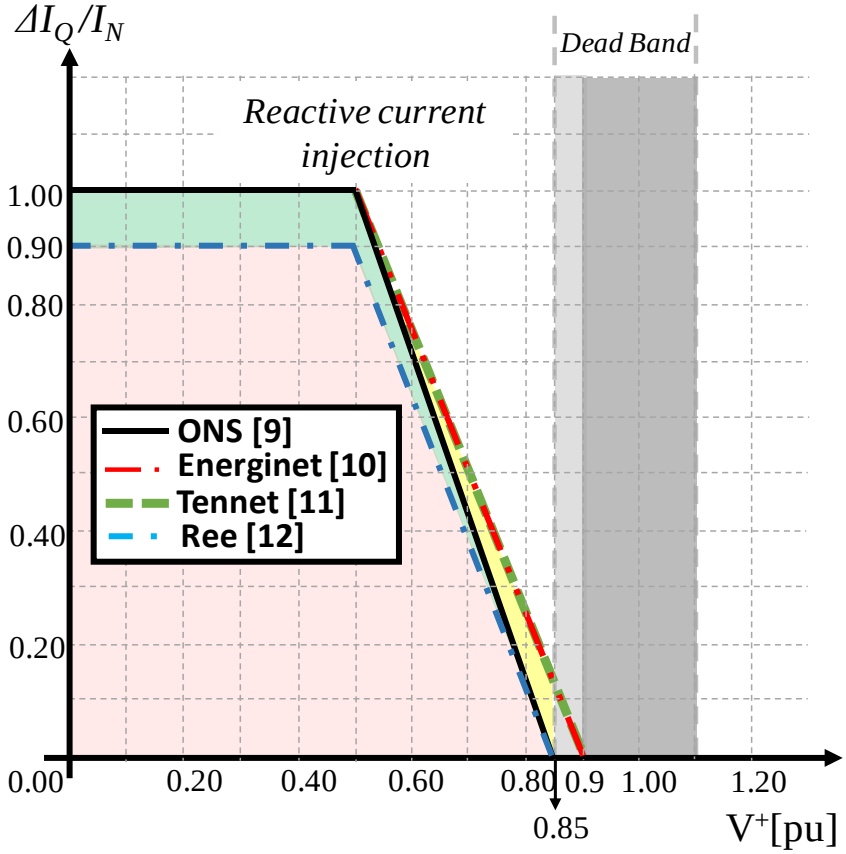

Fig. 1.3: Requirements for reactive current injection during voltage sags for different grid codes.
Source: Adapted from [9–12]

Fig. 1.4 illustrates, in a simplified way, the voltage ride through operation and its relation with the RCI curve in Fig. 1.3, where $I_{q(GC)}$ is the reactive current magnitude defined by the GC, $I_{p(PF)}$ is the pre-fault active current and I_p is the active current magnitude during the voltage sag.

After the fault start, the GU has 30(ms) [9] to 20(ms) [11] to begin the reactive current injection. According to ONS and Tennet [9,11], the curve in Fig. 1.3 defines the algebraic sum between the reactive current before the fault (I_{Q0}) and the necessary value (I_Q) to reach the ΔI_Q. Second Ree [12], during the fault and after the return to the dead band voltage until the fault clearance (reestablishment period in Fig. 1.4), the GU must support the grid with its maximum current capacity (I_{rated}), even that in a low active power production scenario. Hence, the curve in Fig. 1.3 delineates the minimum reactive current magnitude to be delivered to the mains. Besides that, according to Tennet [11] in the reestablishment period, the voltage support must be maintained longer than 500(ms), as exemplified in Fig. 1.4.

After the fault clearance, it is defined in Tennet GC [11] that the GU active power production must be continued immediately and increase to the original value with a gradient at least 20(%) of the rated power per second. For Energinet [10], the return to the to the pre-fault condition should not last more than five seconds. However, for ONS [9] this rate must be adjusted according to the grid characteristic, and the generation system should allow the configuration of active power ramp as can be seen in Fig. 1.4.

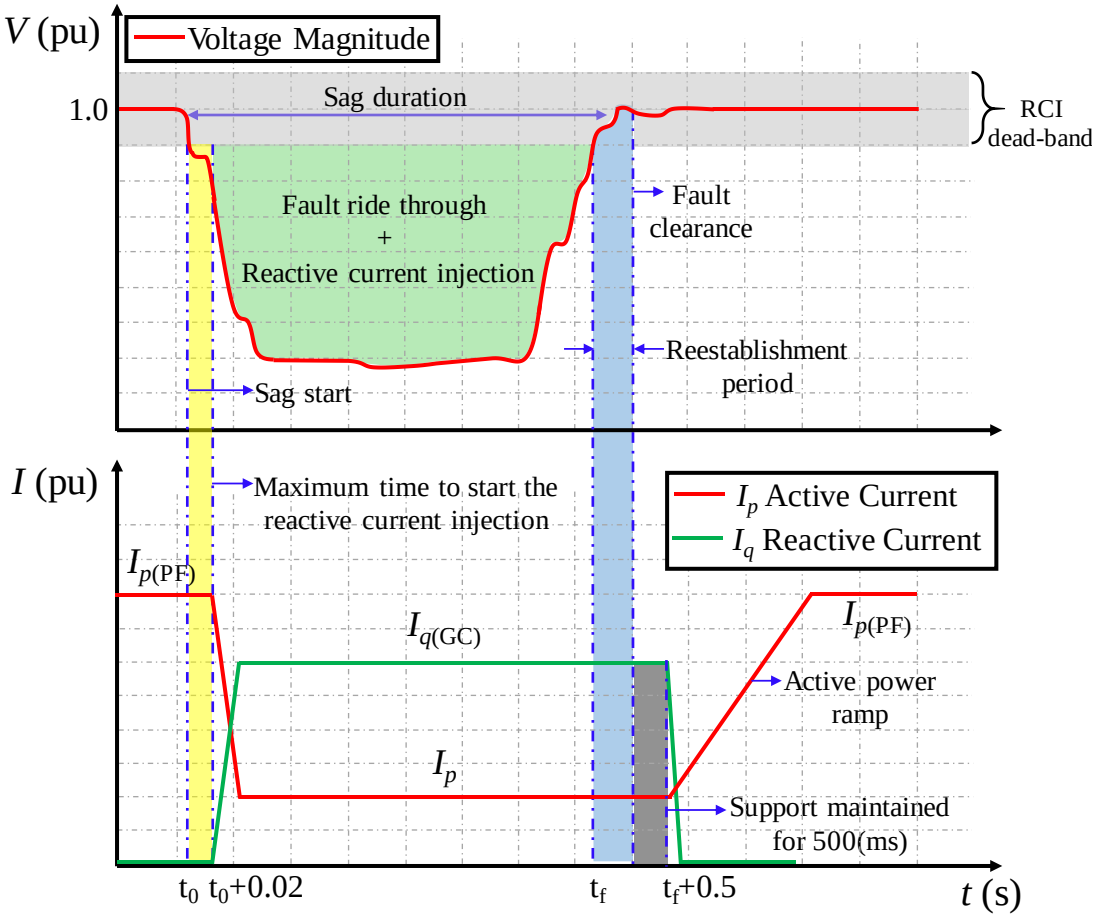

Fig. 1.4: Simplified voltage ride through operation.
Source: Elaborated by the author

1.3 Low voltage ride through literature review

Due to its importance, the LVRT for grid connected converters is a well diffused discussion in the technical literature. In this section is present some of the main references in the core topics related to this subject.

Besides to the magnitude reduction, unbalanced voltage dips causes active and reactive power oscillations with twice of fundamental grid frequency [13]. Several works in literature have proposed methods to deal with the converter operation during unbalanced sags with different objectives.

References [14,15] present some power control strategies that allow to achieve different power quality characteristics, they are the instantaneous active and reactive control (IARC), instantaneously controlled positive sequence (ICPS), average active and reactive control (AARC), positive and negative sequence compensation (PNSC) and balanced positive sequence control (BPSC). Except for the IARC where a high harmonic content is produced, all the strategies listed above generate power oscillations when active and reactive powers are simultaneously injected into the grid.

There are also flexible approaches that use gains that weigh the relation between the positive and negative sequence current components, allowing to reach different power control characteristics [16–19], making it possible to emulate the strategies previously mentioned. In this work three flexible strategies are contemplated, flexible positive and negative sequence control (FPNSC) [16] and pliant active and reactive power control (PARPC) [17], which present two freedom degrees. Finally, the method proposed in [19] has four freedom degrees and it is called in this work generalized flexible power control (GFPC).

It is possible to cancel the active or the reactive power oscillations through the active power oscillation cancel (APOC) or reactive power oscillation cancel (RPOC), these strategies were proposed in [17] as a feature of the flexible approach and they generate sinusoidal unbalanced currents.

In [20] it is analyzed the power oscillation impacts for three-phase photovoltaic distributed generation system and the energy store requirements are analytically deduced and the d.c. link capacitor stress are discussed and it is concluded that the active power oscillation increases the capacitors operation temperature. Though, according to [21], the mitigation of d.c. bus voltage ripple lead to reactive power fluctuation or increase in the low order harmonic content in the GSC currents.

Second [22,23], during severe faults the synchronization with the mains frequency can be lost, mainly in PLL based controls, resulting in the RPP tripping and the generation loss, endangering system stability. In [22] is proposed a closed loop control method based on PLL frequency as a solution to avoid the loss of synchronism, while complying with the grid codes' reactive current injection during very low voltage faults.

The voltage magnitude reduction and RCI requirement priority mean that it is not always possible to maintain the pre-fault grid power supply. References [24–26] propose dynamic power saturation methods as a function of the employed power control strategy, without take in account the RCI requirement. The curtailment strategy proposed in [27] makes precedence over to meet the LVRT RCI requirement, limit the currents magnitude to the converter rated value and when is possible avoid active power oscillations.

The works previously mentioned have centered in the reduction of power oscillation or harmonic content. They always focus on the mitigation of voltage sag impacts to the power electronics converter. There is another research line, which the main motivation is the use of converter capacity to restore the PCC voltage. It is discussed a future scenario, where the penetration of distributed power plants will be high enough to replace the conventional power generators, as present in [28–35]. In [31] for example, it is proposed a reactive power control to regulate the voltage at point of common coupling where is combined the positive and negative sequence reactive powers to flexibly raise and equalize the phase voltages.

However, in order to improve the PCC voltage, it is necessary to supply a considerable current through the negative sequence, generating high active and reactive power oscillations magnitudes [33,34]. In addition, as discussed in [35], the reactive current injection proposed in the actual GCs, not only increase the positive but also the negative and zero sequences voltages magnitudes at the faulted point, due to the coupling between the sequences, generating severe overvoltage in the non-faulted phases.

1.4 Motivation and objectives

Based on the previous section, it is possible to highlights some common aspects in the voltage ride through requirements established in the GCs [9–12]:

- Remain connected to the grid during balanced or unbalanced transient voltage faults while the voltage is within the values outlined by the grid codes;
- Fast recovery to its normal operation condition after the fault clearance;
- Positive sequence reactive current injection capacity during the LVRT operation.

In relation to the last, the power electronic converter presents different characteristics in relation to the conventional synchronous generators, such as active and independent reactive current injection, unbalanced currents synthetize, harmonic currents synthesis capability and faster time response. Thus, for voltages values $V^{+} \geq 0.5$(pu), the idle current capacity can be used to reduce the voltage sag effects on the grid converter or/and to the mains.

The aim of this work is to analyze the power control strategies AARC, PNSC, BPSC, RPOC and APOC in relation to the power qualities issues, such as active and reactive power oscillations and discuss their effects to the three-phase three-wire grid-connected converters and to the electrical mains, given focus to meeting the RCI grid code requirements. A detailed mathematical analysis is performed, thus obtaining some contributions:

- Development of formulations that allow quantifying the grid power oscillation magnitude;
- Development of an equation that allows to approximate the dc bus voltage ripple as a function of power control strategies that generate sinusoidal currents;
- Development of an equation in time domain that describes the point of common coupling (PCC) voltage as a function of power control strategies that generate sinusoidal currents;
- Analysis of the positive and negative sequence power flow in the power control strategies that generate sinusoidal currents.

The results are demonstrated through computational simulation from real systems data using the MATLAB/Simulink software. For this, two case studies are performed, the first one of a 2 (MW) WEC system, and second one of a 118 (MW) generation plant to investigate the voltage support at the point of common coupling.

1.5 Thesis organization

This work is outlined as follows:

- In this chapter a contextualization of the voltage ride through requirements in different countries is presented and the main aspects about this subject in the technical literature are addressed.
- In the second chapter it is discussed the renewable sources integration technologies and an overview of primary source control strategies during voltage sags operation.

- In the third chapter are discussed some of the power control strategies that mitigate distinct power quality issues over unbalanced sag conditions presented in literature.
- In the fourth chapter are proposed equations that quantify the steady state power oscillation magnitude for the sinusoidal power control strategies and equations that relate the active power oscillation and d.c. bus voltage ripple. Finally, a case study with a simulation of a 2(MW) WEC is performed.
- In the fifth chapter is discussed how the power control strategies earlier present can affect the voltage support. For this, a PCC voltage formulation as a function of the GFPC strategy is proposed, and a study case with a simulation of a 118(MW) RPP is performed.
- In the sixth chapter the conclusions are made.

Chapter II

RENEWABLE SOURCES TECHNOLOGIES

ALTHOUGH solar and wind energy conversion systems both employ grid-connected converters to perform the conditioning and control of the generated energy, they present different behaviors and should be manipulated in distinct ways during the fault ride through. In this chapter it is discussed the renewable sources integration technologies and an overview of primary source control strategies during voltage sags operation is realized.

2.1 Renewable power plants

Renewable power plants (RPP) are grouping of power generation units in a same geographic region, where there is a profusion of resources, such as wind or solar irradiation. Usually the RPP systems are built on the continent and called on-shore systems. However, the high energy density present in oceanic winds and the reduction of impacts, like visual appeal, noise disturbance, tower shadow, etc, currently off-shore plants, which are constructed over the sea, are very common in European continent [36].

As represented Fig. 2.1, traditional onshore RPP have its point of common coupling (PCC) connected to the mains through a Dyg (grounded neutral point) transformer, which segregate the RPP and transmission system grounding [37]. The equivalent grid voltage and the transmission line impedance are represented by the elements Z_{lt} and v_g. The power plant has an internal medium voltage grid with line feeders, using underground or overhead lines cables represented by the equivalent impedance Z_{Fx}, which link the generating units point of connection (POC) to the PCC [38]. Finally, the point of generator connection (PGC) is tied to the POC through a medium/low voltage Dy transformer.

In some cases, the off-shore renewable power plants are located at long distances from the shore and to become economically viable, they are built with a high generation capacity, using a greater number or higher power generating units. In this aspect, voltage source converter (VSC) based on high voltage direct current (HVDC) system become more technically and economically advantageous. In offshore plants, it is necessary to use subsea cables, where the a.c. capacitive charging is much higher than overhead lines and the voltage

compensation through shunt reactors, to equalize the a.c. line voltage, become a technical challenge. However, in VSC-HVDC systems the cable length and power capacity is not limited by the capacitive charging current and it offers a fast and independent control of active and reactive power in both directions [36].

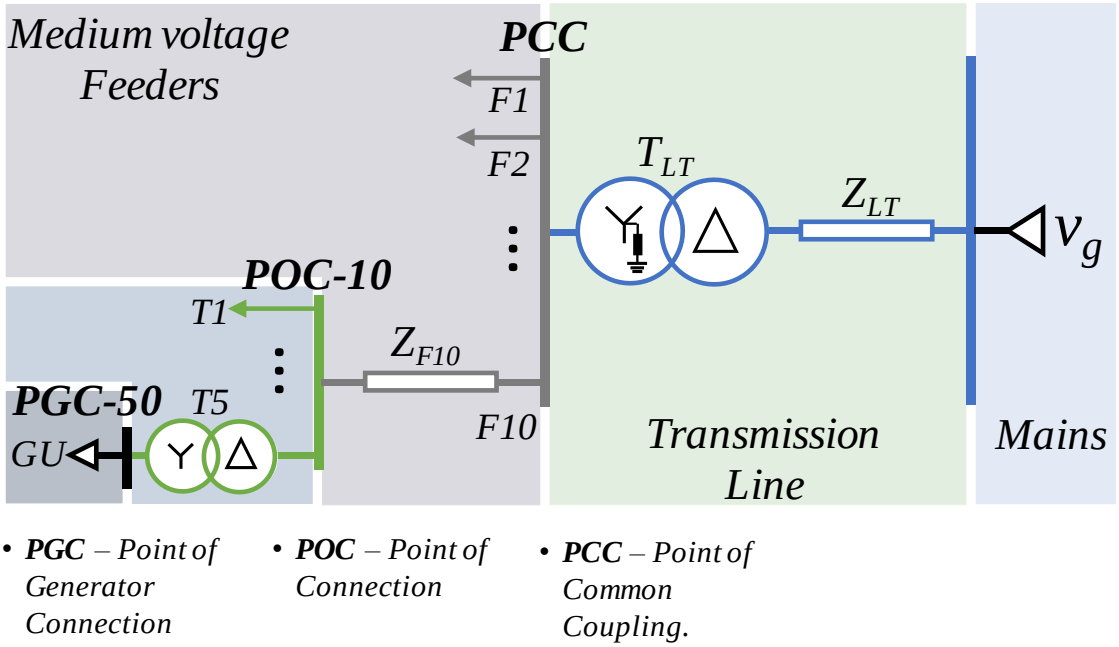

Fig. 2.1: Single line diagram of traditional a.c. connected renewable power plant (RPP).
Source: Elaborated by the author.

The off-shore RPP single line diagram is presented in Fig. 2.2. The VSC-HVDC is composed of bidirectional static converters, interface transformers, phase series reactors, tuned shunt filters and a high direct voltage link. The internal structure is very similar to the traditional renewable plants, except by the intermediary high voltage feeder between the HVDC and the medium voltage collectors. As previously discussed, the HVDC systems transport high energy levels and they have an important role in the associated a.c. power system, moreover, they completely isolate generating units from the a.c. transmission lines. Consequently, the grid codes requirements for HVDC systems are different from those established to traditional RPP and they will not be addressed in this work.

2.2 Grid-connected converters

Renewable generation sources, such as wind or photovoltaic, uses electronic converters that allow the maximum energy extraction from the primary source and the power conditioning to be feed-in to the grid. A basic structure of three-phase three-wire grid-connected converter is presented in Fig. 2.3. Several configurations can be used in the

implementation of the grid side converter (GSC), such as two-level structures, flying capacitor, neutral-point clamped, multi modular converters, etc. Despite the hardware differences, they present similar control structures.

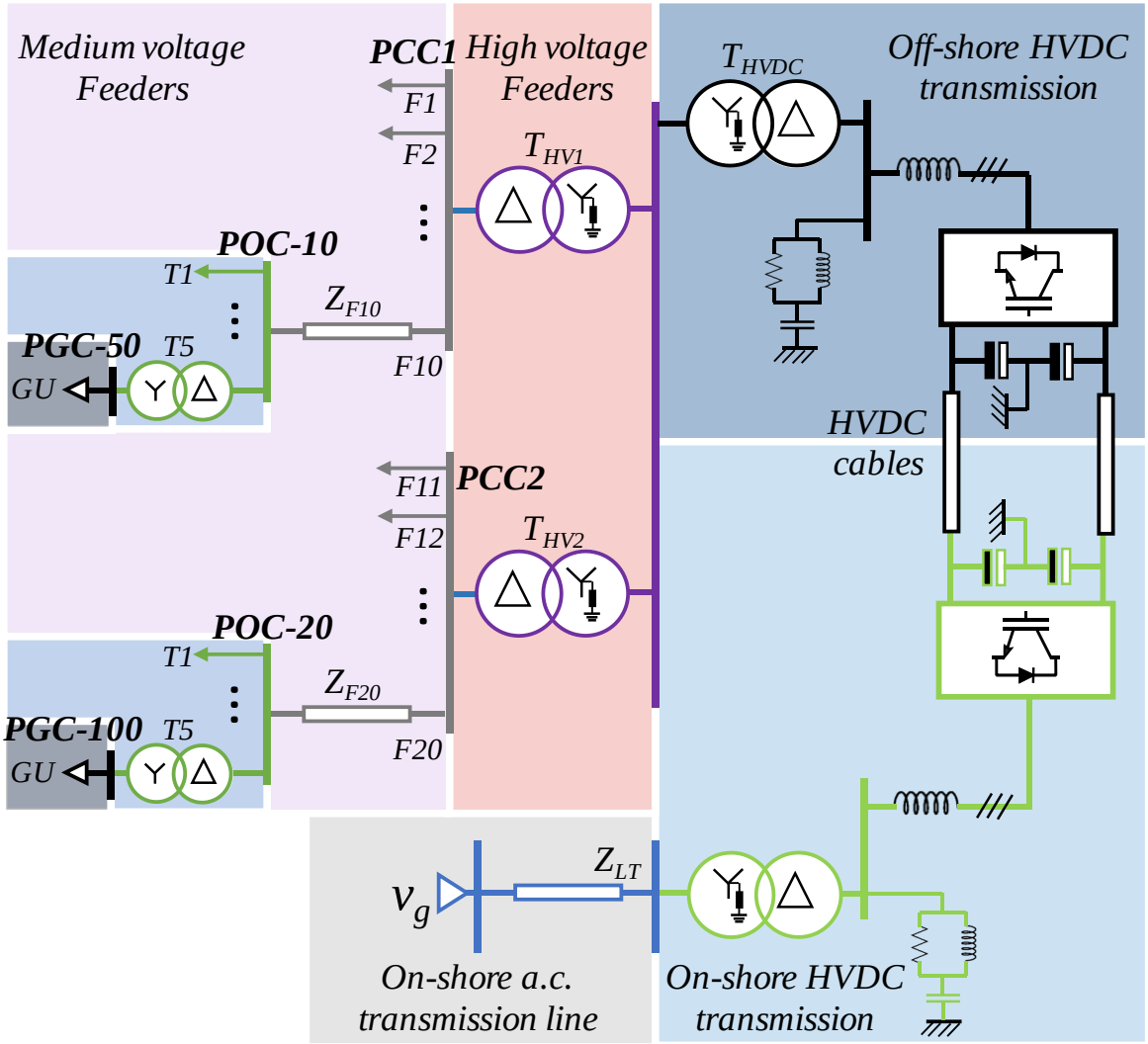

Fig. 2.2: Single line diagram of VSC-HVDC connected renewable power plant (RPP).
Source: Adapted from [36]

The LCL filter aims at reducing the high order harmonics content in GSC currents [39]. The element L_1 represents the inverter side inductor; L_2 is the equivalent inductance from the PGC interface transformer. The filter shunt leg comprises the filter capacitor C_f in series with the damping resistance R_d and inductance L_d. Finally, the d.c. bus equivalent capacitor is denoted by C. The chopper circuit is an essential element for d.c. bus protection against overvoltage in WEC systems and it is covered in details in section 2.3.

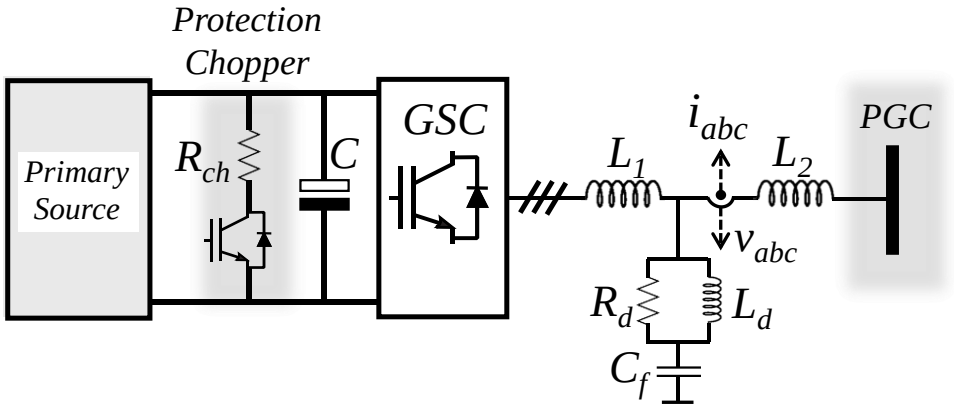

Fig. 2.3: Grid Side Converter.
Source: Elaborated by the author.

2.2.1 Grid side converter control

The GSC simplified control diagram is presented in Fig. 2.4. The control studied in this work is performed in the stationary ($\alpha\beta$) reference frame for the following reasons:

- In a three-wire system there is a fewer number of control variables in relation to the natural (abc) reference frame.
- It presents a smaller number of base transformations in relation to the synchronous (dq) reference frame, reducing the computational effort.
- It has a less dependence of synchronism structures such as phase locked loop (PLL) [40] or frequency locked loop (FLL) [41] that can present instability problems over severe voltage sags [22].

The GSC control is composed of cascade loops. In Fig. 2.4 the GSC bus direct voltage control loop, currents control loop and they auxiliary structures are represented. The measured voltage is decomposed of positive and negative sequence through a double second order generalized integrator (DSOGI) associated to a positive negative sequence extractor (PNSE) structure [40]. To guarantee the precise results and operation under frequency deviations, a closed-loop system employing auxiliary structures such as PLLs or FLLs is demanded. Differently from the synchronous reference frame, where all the control variables are subjected to linear transformations that depends on synchronous structures, in the stationary reference frame they are required only to improve the precision of sequence voltages decomposition.

The GSC output filter determines the current control dynamic. Since the filter shunt branch has high impedance, its effect could be ignored and therefore:

$$v_{(c)\alpha} = R_t\, i_\alpha + L_t \frac{di_\alpha}{dt} + v_\alpha,$$
$$v_{(c)\beta} = R_t\, i_\beta + L_t \frac{di_\beta}{dt} + v_\beta, \tag{2.1}$$

where $v_{(c)\alpha\beta}$ is the GSC synthesized voltage at the converter terminals, $L_t = L_1 + L_2$ and $R_t = R_1 + R_2$ are the filter equivalent inductance and resistance respectively and $v_{\alpha\beta}$ the grid (PGC) voltage. Assuming that the generation unit cannot change the voltage $v_{\alpha\beta}$, it could be considered a disturbance to the current control. Hence, $v_{(c)\alpha\beta}$ variations result in the current circulation through the elements L_t and R_t and the process transfer function is defined by [42]:

$$G_c(s) = \frac{i}{v_{(c)}} = \frac{1}{L_t\, s + R_t}. \tag{2.2}$$

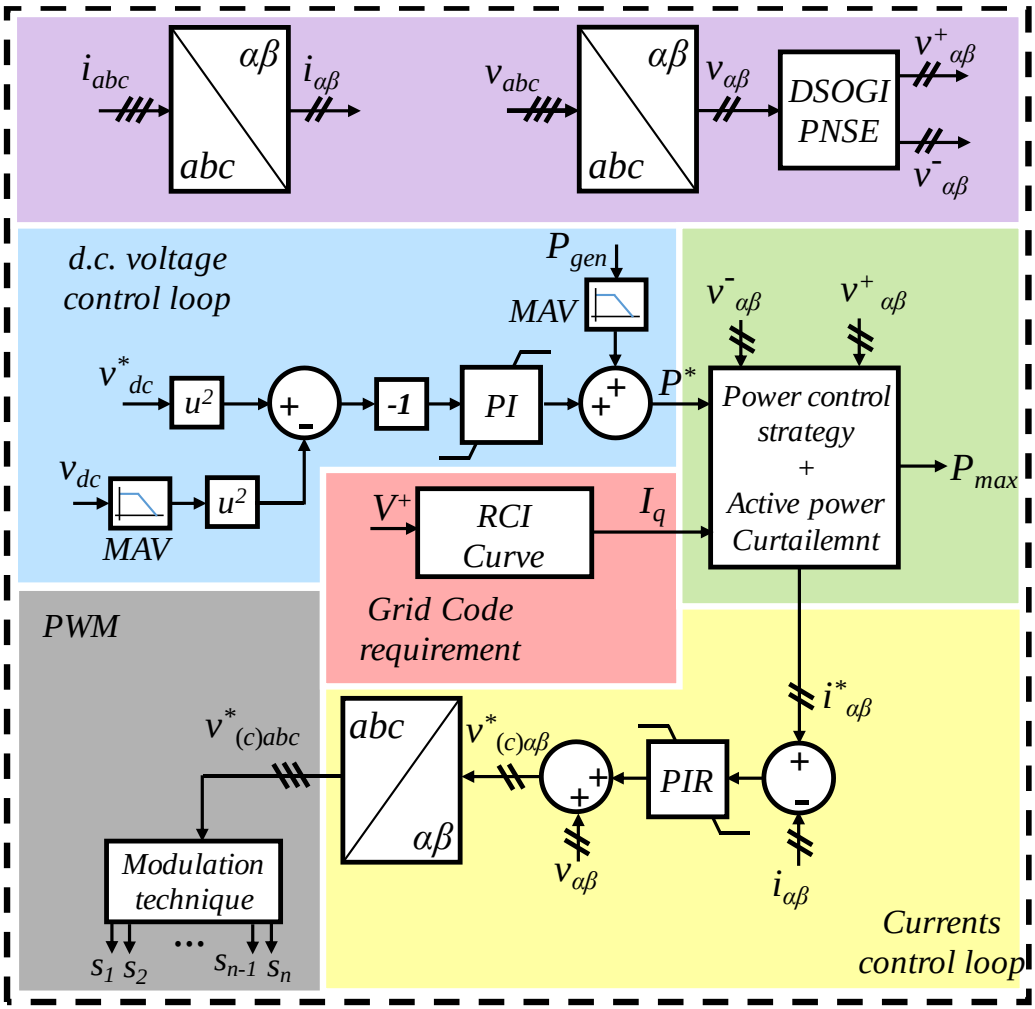

Fig. 2.4: Grid side converter control loop.
Source: Elaborated by the author.

The magnitude and phase deviations of voltage $v_{(c)\alpha\beta}$ around $v_{\alpha\beta}$ produce the current flow through the converter and the mains. Therefore a feed-forward action with $v_{\alpha\beta}$ is applied to the proportional-resonant (PR) controllers [43] output, in order to reduce the controller efforts, resulting in the reference voltages $v^*_{(c)\alpha\beta}$.

The power control strategy and current saturation block is the core of this work and is detailed in the following chapters. The block inputs are the active power reference P^* and the GC reactive current magnitude I_q. It calculates the reference currents $i^*_{\alpha\beta}$ and limits the grid active power (P_{max}) to avoid the converter to operate above its rated current.

The d.c. bus control is based in the GSC input and output power balance, where the difference between them reflects in the capacitor stored energy and consequently in the direct voltage v_{dc} level [42], i.e.:

$$\frac{C}{2}\frac{dv_{dc}^2}{dt} = P_{gen} - P, \tag{2.3}$$

P_{gen} is the power generated by the primary source, P is the power delivered to the grid active power and C the equivalent d.c. bus capacitance. Assuming P_{gen} is a disturbance, it is defined a transfer function between the power P and the quadratic direct voltage, as follow.

$$G_{dc}(s) = \frac{P}{v_{dc}^2} = -\frac{2}{C}\frac{\tau s + 1}{s}. \tag{2.4}$$

The zero in equation (2.4) represents the grid power flow dynamic and its time constant τ is defined in (2.5), where $P_{(n)}$ and $V_{g(n)}$ are the nominal power and phase voltage magnitude respectively[42].

$$\tau = \frac{2\,L_t\,P_{(n)}}{3\left(V_{g(n)}\right)^2}. \tag{2.5}$$

In steady state, the input and output powers must be equal. Hence, a feedforward action with the power P_{gen} on the voltage controller output is used to reduce the integral control effort, resulting in the reference power P^*. Moving average filters in the feedback and feedforward signals reduce the ripple in the measured values and prevent the control instability. The controller's implementation description details and tuning methodology are described in Appendix A:.

2.3 Primary source behavior in voltage ride through operation

This work aims to analyze the GSC operation and control over unbalanced faults. Nevertheless, the primary source behavior has a substantial impact on grid converter operation, and a detailed discussion in relation to them is needed.

The focus of this work is on full-scale grid converters, i.e., the primary source and the mains are completely isolated. They have greater flexibility and reliability with respect to partial-scale systems, such as, doubly-fed induction generators (DFIG), where the connection between the generator and grid makes the DFIG very sensitive to grid disturbances [44].

2.3.1 Photovoltaic energy conversion systems

In multi-megawatt systems, the PV array is directly connected to the GSC, presenting a single-stage structure, as shown in Fig. 2.5. Hence, in normal operation conditions, the MPPT algorithm increase or decrease the direct voltage reference v_{dc}^{*} inside the converter operation range, tracking the maximum power point.

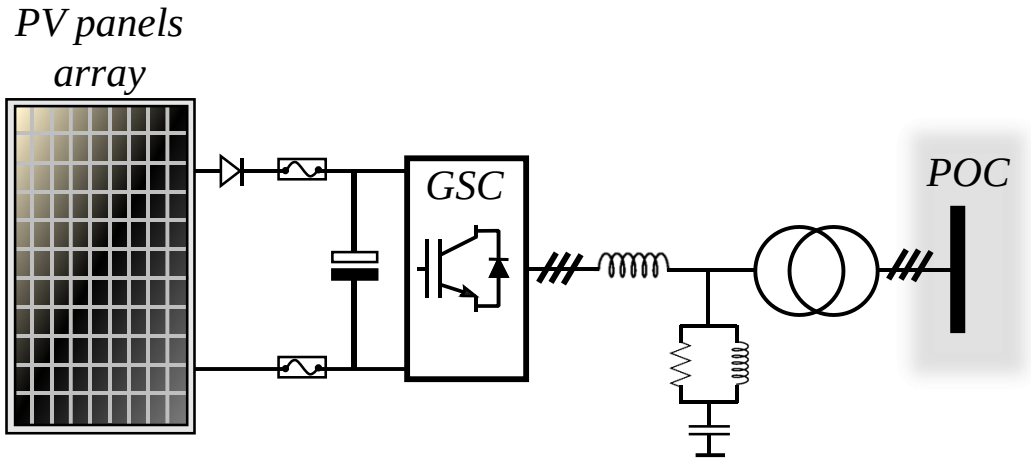

Fig. 2.5: Single line diagram for single-stage PV inverters
Source: Elaborated by the author.

During voltage sags the control of PV active power should be limited to the maximum value P_{max}, defined by the GSC active power curtailment algorithm to be within the converter current limitation and consequently keep the power balance in the d.c. bus capacitors, prevent the d.c. link overvoltage. Reference [45] proposes a general algorithm, where during the fault, the MPPT is replaced by the calculus of the voltage reference based on the required external power set-point, as exemplified in Fig. 2.6.

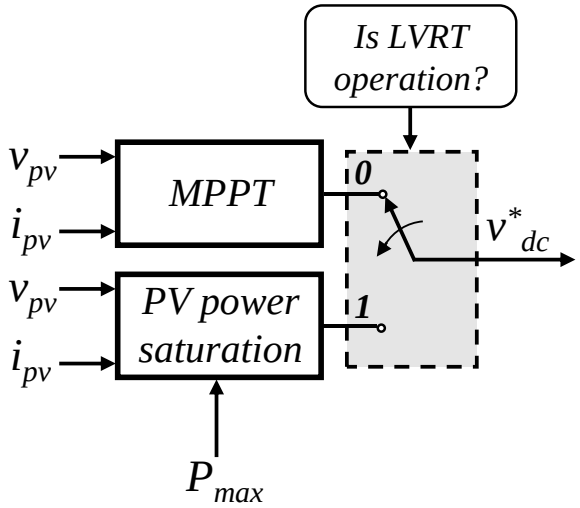

Fig. 2.6: Simplified diagram of PV power saturation
Source: Elaborated by the author.

Fig. 2.7 presents the PV power (P_{pv}) saturation principle in the array power versus voltage curve, where P_{mppt} is the maximum power point. In the saturation mode the algorithm proposed in [45] could operate in the left (Point A) and right (Point B) side of power PV curve, increasing or decreasing the array voltage V_{pv}. However, in single-stage inverters, the operation point cannot be moved to the left side, because the d.c. voltage may become lower than the GSC operation minimum voltage, preventing unnecessary converter disconnection. On the other hand, the d.c. voltage ripple ($\tilde{v}_{osc}$) in the point B, produces higher power oscillations ($\tilde{p}_{osc(B)}$) in the PV array, compared to the operation point A ($\tilde{p}_{osc(A)}$), which is a significant drawback.

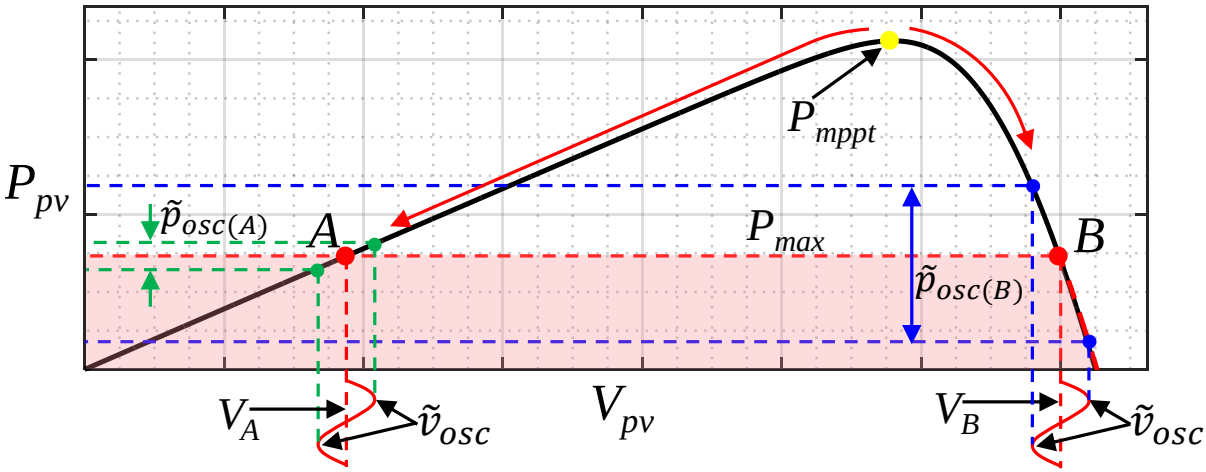

Fig. 2.7: PV power saturation during LVRT.
Source: Elaborated by the author.

2.3.2 Wind energy conversion systems

In full-scale WECs, a back-to-back structure is introduced between the stator winding and the mains, decoupling the generator and the grid side. This characteristic allows the use of several kinds of machine technologies. Permanent magnet synchronous machines (PMSG) is one of the most employed in the recent years, especially in off-shore RPPs, due to its high efficiency, energy density and mainly reliability, since they are built with a large number of poles, eliminating the gear box and there are no brushes for electrical connection with the rotor [46]. Fig. 2.8 presents a full-scale WEC employing a PMSG, where MSC is the machine side converters.

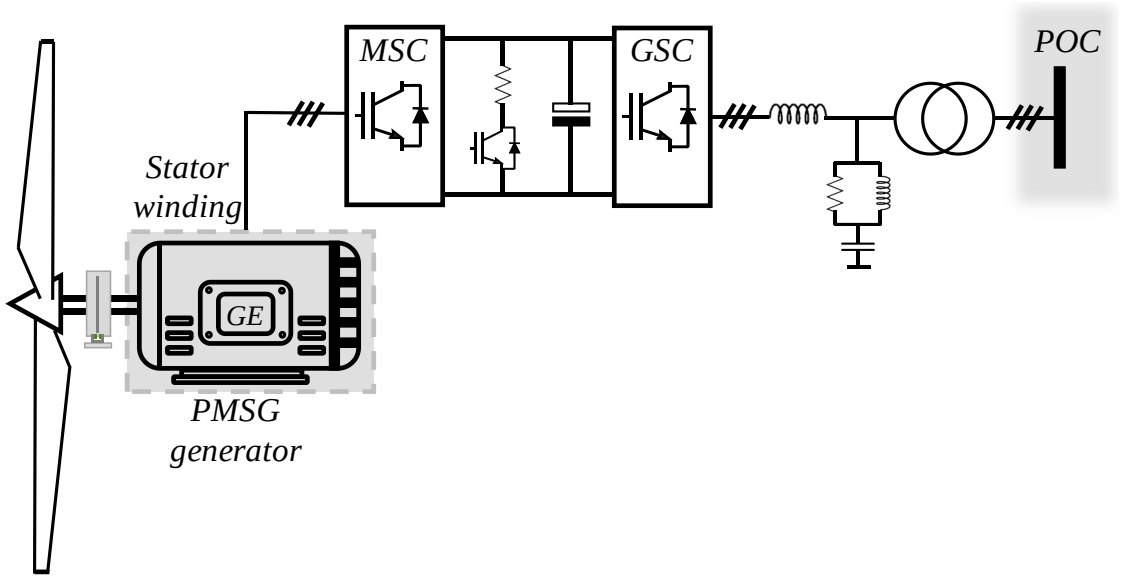

Fig. 2.8: Full scale WEC with permanent magnet synchronous machine
Source: Elaborated by the author

In LVTR operation the GSC capacity to supply the active power to the grid is reduced and the power that is converted by the wind turbine and generator may increase the d.c. bus voltage [47]. It is possible to reduce the generator active power reference during the fault, which raise the turbine shaft speed, due to the high amount of kinetic energy. This is a significant drawback, since it increases the active power ramp slope after the fault clearance [47]. The generated energy reduction can also be achieved through the pitch control. However, the mechanical system has a slow time response and cannot reduce the active power fast enough [48].

The most common solution is the braking resistor or protection chopper, where a resistor is inserted in parallel to the bus capacitors through a static switch. The surplus power is dissipated on it, ensuring a faster time response and return to the normal operation after the fault clearance. Some WEC manufactures uses a hysteresis control for the protection chopper,

i.e., when the bus direct voltage is greater than a maximum value, the chopper static key is closed, dissipating the surplus energy in the breaking chopper. When the direct voltage drops below a minimum value the chopper is turned off.

In this work it is proposed a pulse width modulation (PWM) chopper control, where the maximum grid power (P_{max}) calculated by the curtailment algorithm is compared to the direct voltage output power set-point (P^*), the difference between them is the primary source surplus energy and it is normalized by the nominal power, in order to calculate the protection chopper duty cycle during the LVRT operation, as presented in Fig. 2.9.

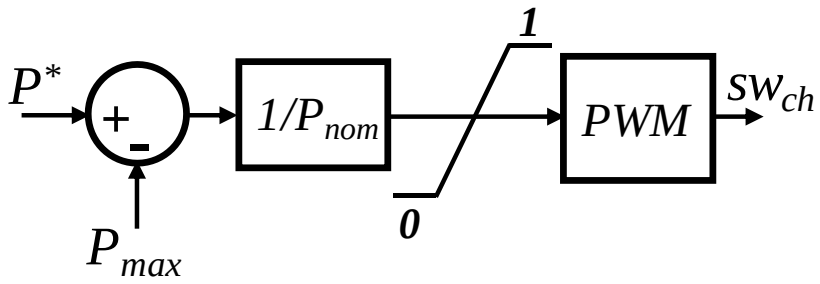

Fig. 2.9: Proposed chopper control diagram.
Source: Elaborated by the author

2.4 Chapter Conclusions

The aims of this chapter were present an overview some of the renewable power source technologies and its integration to the electrical mains. Despite the completely different characteristics, WEC and PV systems employ grid connected converters to control and conditioning the mains feed-in power and, although several converters configurations can be used in the GSC implementation, they present very similar control structures.

Another important point addressed in this chapter is the primary source behavior during the LVRT operation. The PV systems active power reduction can be easily achieved though the alteration in the array voltage, without additional protection circuits and stress in the d.c. bus capacitors.

In the multi-megawatts WEC systems, the high mechanical inertia makes it impossible to reduce the generator active power in a timely manner. Therefore, the surplus energy must be dissipated in an auxiliary protection circuit, increasing the implementation costs.

The primary source protection strategies guarantee the steady state power balance during the LVRT operation, preserving the GSC bus direct voltage in a safe operation margin. Thus, the following chapter will focus in the GSC operation and its interaction with the grid.

Chapter III

POWER CONTROL STRATEGIES

GRID connected converters have greater currents synthesis flexibility in relation to the conventional synchronous generator, such as active and reactive independent current control, unbalanced and harmonic currents synthesis capability and faster time response. The focus of this work is in three-phase three-wire power converters and the zero sequence voltages and currents are not taken in account. Then, it is possible to employ different power control strategies that mitigate distinct power quality issues over unbalanced sag conditions. Some of these strategies are discussed in this chapter.

3.1 Voltage sags characteristics

Voltage sag (voltage dip) is a sudden reduction in the voltage magnitude for a short time period [28]. The main causes of this transient phenomenon are abrupt load variations and short circuits and in the most of cases, they are phase-to-ground or phase-to-phase occurrences. Single phase faults result in unbalanced voltages, which can be mathematically quantified by [49]:

$$u = \frac{V^+}{V^-}, \tag{3.1}$$

where u is the unbalanced factor, V^+ is the positive and V^- the negative sequence voltage magnitude. The unbalanced factor is not an ideal index for voltage sags characterization, because there are several combinations that results in the same value of u. However, it is a recurrent term in the power control strategies formulations, and will be adopted in this work.

In addition to the voltage magnitude reduction, short circuits can cause the phase jumps, which are sudden variations of the voltages phase angles, due to the change in the *X/R* ratio between the feeder and the faulted point [50]. According to [50] the voltage sags can be generically classified in 4 types in relation to its magnitude and angle phase jump, denoted by A, B, C and D as shown in Fig. 3.1. For sags type A, all voltages drop to the same magnitude value, for type B only one phase is reduced. In type C, in addition to the two phases sag, it is changed their angle. Finally, in type D the three voltages change their value, but the angle is

altered only in two. The propagation of unbalanced sags in the electrical power system is affected by the transformer winding connection due to the absence of the zero sequence, as presented in Table I.

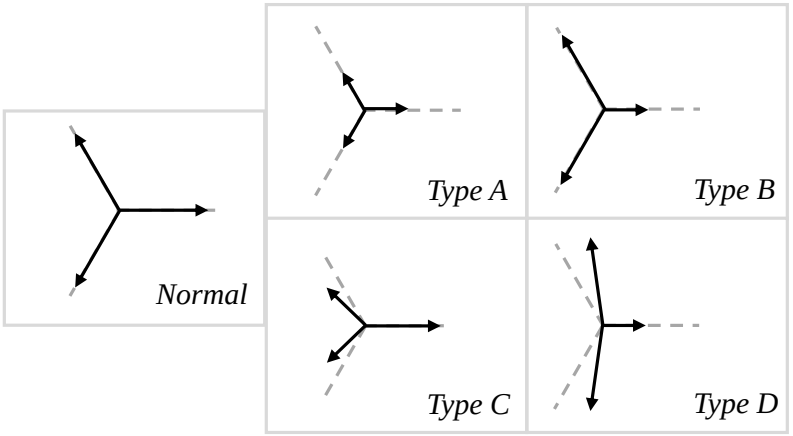

Fig. 3.1: Fundamental types of sags.
Source: Adapted from [50]

Table I: Transformation of sag type on the secondary side

Transformer connection	**Sag Type on primary side**			
	A	B	C	D
Ynyn	A	B	C	D
Yy, Dd, Dz	A	D	C	D
Yd, Dy, Yz	A	C	D	C

Source: Adapted from [50]

In unbalanced dips, the grid voltage could be modeled as the sum of its positive and negative sequence components [28], since the transformers winding connection in Fig. 2.1 insulate the mains zero sequence voltage from the RPP side, hence:

$$\begin{aligned} v_a &= V^+\cos(\omega t+\phi^+)+V^-\cos(\omega t-\phi^-),\\ v_b &= V^+\cos\left(\omega t+\phi^+-\frac{2\pi}{3}\right)+V^-\cos\left(\omega t-\phi^-+\frac{2\pi}{3}\right),\\ v_c &= V^+\cos\left(\omega t+\phi^++\frac{2\pi}{3}\right)+V^-\cos\left(\omega t-\phi^--\frac{2\pi}{3}\right), \end{aligned} \tag{3.2}$$

where ϕ^+ and ϕ^- are the sequences phase angles and ω the fundamental frequency. It can be noted that V^+, V^-, ω, ϕ^+, and ϕ^- are time-varying parameters [28]. However, for sake of simplicity, in this work they are assumed constant during the sag. Using Clark transformation [31], the signals are transferred to the stationary reference frame:

$$\begin{aligned} v_\alpha &= V^+\cos(\omega t+\phi^+)+V^-\cos(-\omega t+\phi^-),\\ v_\beta &= V^+\sin(\omega t+\phi^+)+V^-\sin(-\omega t+\phi^-). \end{aligned} \tag{3.3}$$

A generalized mathematical representation could be written to represent the instantaneous voltage through the space vector notation, that is:

$$\begin{aligned} \mathbf{v}^+ &= \left[v_\alpha^+, v_\beta^+\right] = [v_a^+, v_b^+, v_c^+], \\ \mathbf{v}^- &= \left[v_\alpha^-, v_\beta^-\right] = [v_a^-, v_b^-, v_c^-], \\ \mathbf{v} &= \mathbf{v}^+ + \mathbf{v}^-. \end{aligned} \tag{3.4}$$

In the stationary frame, the vectors $\mathbf{v}^+$ and $\mathbf{v}^-$ have circular trajectories but, different directions of rotation. In unbalanced conditions, $\mathbf{v}$ has an elliptical path, where its eccentricity is related to the negative sequence amount, since the vector maximum magnitude happens when $\mathbf{v}^+$ and $\mathbf{v}^-$ are aligned and the minimum when they are in opposite positions. The difference between ϕ^+ and ϕ^- angles causes a displacement ϕ of the voltage trajectory in relation to the α-axis, as can be seen in the Fig. 3.2.

The space vector instantaneous norm $|\mathbf{v}|$ presents time-varying oscillations, demonstrated by the elliptic trajectory, and it is defined by the equation (3.5), where $|\mathbf{v}^+|$ and $|\mathbf{v}^-|$ is the positive and negative space vectors magnitude, according to equations (3.6).

$$|\mathbf{v}|^2 = (\mathbf{v}^+ + \mathbf{v}^-) \cdot (\mathbf{v}^+ + \mathbf{v}^-) = |\mathbf{v}^+|^2 + |\mathbf{v}^-|^2 + 2|\mathbf{v}^+||\mathbf{v}^-|\cos(2\omega t + \phi^+ - \phi^-), \tag{3.5}$$

$$\begin{aligned} |\mathbf{v}|^2 &= v_\alpha^2 + v_\beta^2, \\ |\mathbf{v}^+|^2 &= {v_\alpha^+}^2 + {v_\beta^+}^2, \\ |\mathbf{v}^-|^2 &= {v_\alpha^-}^2 + {v_\beta^-}^2. \end{aligned} \tag{3.6}$$

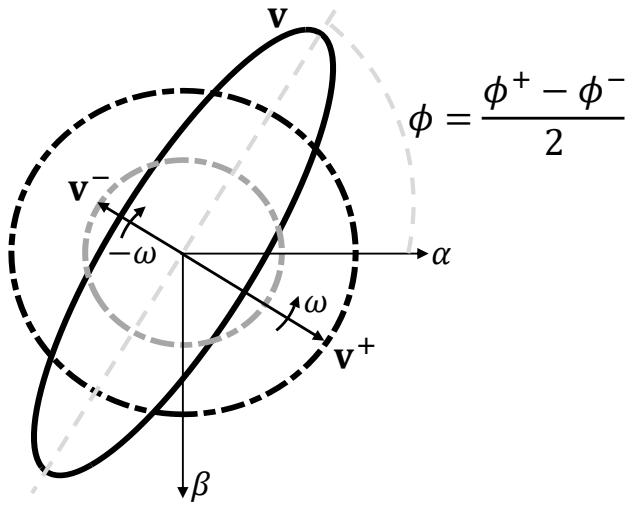

Fig. 3.2: Grid voltage vector representation.
Source: Elaborated by the author

3.1.1 Instantaneous power oscillations

The current vector (**i**) can be decomposed into active ($\mathbf{i}_p$) and reactive ($\mathbf{i}_q$) parts, besides the sequential components, where $\mathbf{i}_p$ is parallel and $\mathbf{i}_q$ is orthogonal to **v**.

$$\begin{aligned} \mathbf{i}_p &= \mathbf{i}_p^+ + \mathbf{i}_p^-, \\ \mathbf{i}_q &= \mathbf{i}_q^+ + \mathbf{i}_q^-, \\ \mathbf{i} &= \mathbf{i}_p + \mathbf{i}_q. \end{aligned} \tag{3.7}$$

The instantaneous active (p) and reactive (q) power terms are defined in equations (3.8) and (3.9), respectively, with P, Q the mean power and $\tilde{p}$, $\tilde{q}$ the oscillatory values with twice fundamental frequency, where '·' denotes the vectors internal product.

$$p = (\mathbf{v}^+ + \mathbf{v}^-) \cdot \left(\mathbf{i}_p^+ + \mathbf{i}_p^- + \mathbf{i}_q^+ + \mathbf{i}_q^-\right) = \cdots$$
$$\underbrace{\mathbf{v}^+ \cdot \mathbf{i}_p^+ + \mathbf{v}^- \cdot \mathbf{i}_p^-}_{P} + \underbrace{\mathbf{v}^+ \cdot \mathbf{i}_q^+ + \mathbf{v}^- \cdot \mathbf{i}_q^-}_{0} + \underbrace{\mathbf{v}^- \cdot \mathbf{i}_p^+ + \mathbf{v}^+ \cdot \mathbf{i}_p^- + \mathbf{v}^+ \cdot \mathbf{i}_q^- + \mathbf{v}^- \cdot \mathbf{i}_q^+}_{\tilde{p}}, \tag{3.8}$$

$$q = (\mathbf{v}_\perp^+ + \mathbf{v}_\perp^-) \cdot (\mathbf{i}_p^+ + \mathbf{i}_p^- + \mathbf{i}_q^+ + \mathbf{i}_q^-) = \cdots$$
$$\underbrace{\mathbf{v}_\perp^+ \cdot \mathbf{i}_\mathrm{q}^+ + \mathbf{v}_\perp^+ \cdot \mathbf{i}_\mathrm{q}^-}_{Q} + \underbrace{\mathbf{v}_\perp^+ \cdot \mathbf{i}_\mathrm{p}^+ + \mathbf{v}_\perp^- \cdot \mathbf{i}_\mathrm{p}^-}_{0} + \underbrace{\mathbf{v}_\perp^- \cdot \mathbf{i}_\mathrm{q}^+ + \mathbf{v}_\perp^+ \cdot \mathbf{i}_\mathrm{q}^- + \mathbf{v}_\perp^+ \cdot \mathbf{i}_\mathrm{p}^- + \mathbf{v}_\perp^- \cdot \mathbf{i}_\mathrm{p}^+}_{\tilde{q}}, \tag{3.9}$$

$\mathbf{v}_\perp$ is the orthogonal projection of vector **v,** defined by [28]:

$$\mathbf{v}_{\perp(abc)} = \frac{1}{\sqrt{3}}\begin{bmatrix} 0 & 1 & -1 \\ -1 & 0 & 1 \\ 1 & -1 & 0 \end{bmatrix}\begin{bmatrix} v_a \\ v_b \\ v_c \end{bmatrix}, \mathbf{v}_{\perp(\alpha,\beta)} = \begin{bmatrix} 0 & 1 \\ -1 & 0 \end{bmatrix}\begin{bmatrix} v_\alpha \\ v_\beta \end{bmatrix}. \tag{3.10}$$

According to the equations (3.8) and (3.9), the projection of current vector **i** in **v** results in active power transfer, while the projection of **i** over $\mathbf{v}_\perp$ produces the reactive power flow [20]. However, the interaction of voltages and currents from different sequences results in power oscillations, where they can be divided into cosine and sine terms, according to the relations (3.11) and (3.12) [34].

$$\begin{aligned} P_{c2}\cos(2\omega t + \phi^+ - \phi^-) &= \mathbf{v}^- \cdot \mathbf{i}_p^+ + \mathbf{v}^+ \cdot \mathbf{i}_p^-, \\ Q_{c2}\cos(2\omega t + \phi^+ - \phi^-) &= \mathbf{v}_\perp^- \cdot \mathbf{i}_\mathrm{q}^+ + \mathbf{v}_\perp^+ \cdot \mathbf{i}_\mathrm{q}^-, \end{aligned} \tag{3.11}$$

$$\begin{aligned} P_{s2}\sin(2\omega t + \phi^+ - \phi^-) &= \mathbf{v}_\perp^+ \cdot \mathbf{i}_p^- + \mathbf{v}_\perp^- \cdot \mathbf{i}_p^+, \\ Q_{s2}\sin(2\omega t + \phi^+ - \phi^-) &= \mathbf{v}^+ \cdot \mathbf{i}_q^- + \mathbf{v}^- \cdot \mathbf{i}_q^+. \end{aligned} \tag{3.12}$$

where P_{c2}, Q_{c2}, P_{s2} and Q_{s2} are the power oscillations magnitudes.

3.2 Non-sinusoidal currents power control strategies

The power control strategies calculate the current reference vector $\mathbf{i}^*$**,** which feed-in the active P^* and reactive Q^* power set-points [20], where it is represented in Fig. 2.4 in the green

sector. The power control strategies analyzed in this section are called non-sinusoidal reference currents and they can reduce or even cancel the active and reactive power oscillations simultaneously. However, the reference currents will present a high harmonic content as it is explained in the following subsections.

3.2.1 Instantaneous active and reactive control (IARC)

The IARC strategy generates active $\mathbf{i}_p^*$ and reactive $\mathbf{i}_q^*$ reference currents instantaneously proportional to the vectors $\mathbf{v}$ and $\mathbf{v}_\perp$. This strategy is directly based on the instantaneous power theory concepts [51], and the reference currents are calculated as follows [14,15]:

$$\mathbf{i}_p^* = \frac{P^*}{|\mathbf{v}|^2}\,\mathbf{v} = g\,\mathbf{v}, \tag{3.13}$$

$$\mathbf{i}_q^* = \frac{Q^*}{|\mathbf{v}|^2}\,\mathbf{v}_\perp = b\,\mathbf{v}_\perp, \tag{3.14}$$

where g is the instantaneous conductance and b the susceptance seen from the GSC output and they define the proportion relation between the voltages and currents vectors. Since $|\mathbf{v}|^2 = \mathbf{v}\cdot\mathbf{v} = \mathbf{v}_\perp\cdot\mathbf{v}_\perp$, it can be demonstrated that the IARC produces the most efficient set of currents that delivers the power set-points P^* and Q^*[20], because there are no instantaneous power oscillations even with unbalanced voltages:

$$p = \mathbf{v}\cdot\left(\mathbf{i}_p + \mathbf{i}_q\right) = \frac{P^*}{|\mathbf{v}|^2}\underbrace{\mathbf{v}\cdot\mathbf{v}}_{|\mathbf{v}|^2} + \frac{Q^*}{|\mathbf{v}|^2}\underbrace{\mathbf{v}\cdot\mathbf{v}_\perp}_{0} = P^*, \tag{3.15}$$

$$q = \mathbf{v}_\perp\cdot\left(\mathbf{i}_p + \mathbf{i}_q\right) = \frac{P^*}{|\mathbf{v}|^2}\underbrace{\mathbf{v}_\perp\cdot\mathbf{v}}_{0} + \frac{Q^*}{|\mathbf{v}|^2}\underbrace{\mathbf{v}_\perp\cdot\mathbf{v}_\perp}_{|\mathbf{v}|^2} = Q^*. \tag{3.16}$$

According to the equation (3.5) the instantaneous norm $|\mathbf{v}|^2$ is not constant, resulting in non-sinusoidal references with a high total harmonic distortion (THD) value. According to [18] the THD can be approximated by the expression (3.17), assuming only active power injection:

$$THD = \frac{u}{\sqrt{1-u^2}}. \tag{3.17}$$

3.2.2 Instantaneously controlled positive sequence (ICPS)

The ICSP aims to inject the power set-points P^* and Q^* exclusively through the positive sequence, i.e., there are no negative sequence components in the reference currents. It was

proposed considering only one of the power set-points is different from zero during the voltage sag. Hence, the following restraints are imposed [14,15]:

$$\left.\begin{aligned} P^* &= \mathbf{v}\cdot\mathbf{i}_p^+ = \mathbf{v}^+\cdot\mathbf{i}_p^+ + \mathbf{v}^-\cdot\mathbf{i}_p^+ \\ 0 &= \mathbf{v}\cdot\mathbf{i}_p^- = \mathbf{v}^+\cdot\mathbf{i}_p^- + \mathbf{v}^-\cdot\mathbf{i}_p^- \end{aligned}\right\} \Longrightarrow\ \mathbf{i}_q = 0, \tag{3.18}$$

$$\left.\begin{aligned} Q^* &= \mathbf{v}_\perp\cdot\mathbf{i}_q^+ = \mathbf{v}_\perp^+\cdot\mathbf{i}_q^+ + \mathbf{v}_\perp^-\cdot\mathbf{i}_q^+ \\ 0 &= \mathbf{v}_\perp\cdot\mathbf{i}_{\boldsymbol{q}}^- = \mathbf{v}_\perp^+\cdot\mathbf{i}_q^- + \mathbf{v}_\perp^-\cdot\mathbf{i}_q^- \end{aligned}\right\} \Longrightarrow\ \mathbf{i}_p = 0. \tag{3.19}$$

Resulting in the subsequent currents equations [14,15]:

$$\mathbf{i}_p^{+*} = \frac{P^*}{|\mathbf{v}^+|^2 + \mathbf{v}^+\cdot\mathbf{v}^-}\,\mathbf{v}^+ = g^+\,\mathbf{v}^+, \tag{3.20}$$

$$\mathbf{i}_q^{+*} = \frac{Q^*}{|\mathbf{v}^+|^2 + \mathbf{v}^+\cdot\mathbf{v}^-}\,\mathbf{v}_\perp^+ = b^+\,\mathbf{v}^+, \tag{3.21}$$

where g^+ and b^+ are the instantaneous positive sequence conductance and susceptance, respectively. Replacing (3.18) and (3.19) into the instantaneous power expressions (3.8) and (3.9), the ICSP power is defined by:

$$p = (\mathbf{v}^+ + \mathbf{v}^-)\cdot\left(\mathbf{i}_p^+ + \mathbf{i}_q^+\right) = \underbrace{\mathbf{v}^+\cdot\mathbf{i}_p^+ + \mathbf{v}^-\cdot\mathbf{i}_p^+}_{P^*} + \underbrace{\mathbf{v}^+\cdot\mathbf{i}_q^+}_{0} + \underbrace{\mathbf{v}^-\cdot\mathbf{i}_q^+}_{\tilde{\boldsymbol{p}}}, \tag{3.22}$$

$$q = (\mathbf{v}_\perp^+ + \mathbf{v}_\perp^-)\cdot\left(\mathbf{i}_p^+ + \mathbf{i}_q^+\right) = \underbrace{\mathbf{v}_\perp^+\cdot\mathbf{i}_q^+ + \mathbf{v}_\perp^-\cdot\mathbf{i}_q^+}_{Q^*} + \underbrace{\mathbf{v}_\perp^+\cdot\mathbf{i}_p^+}_{0} + \underbrace{\mathbf{v}_\perp^-\cdot\mathbf{i}_p^+}_{\tilde{\boldsymbol{q}}}. \tag{3.23}$$

According to the equations above, the negative sequence voltage interaction with its positive sequence orthogonal current produces power oscillations that are zero if this component of the current is null. Moreover, the internal products in the equations (3.20) and (3.21) denominators result in non-sinusoidal references, where, the ICSP THD can be approximated through the equation (3.24), when only active power is injected [18]:

$$THD = \sqrt{\frac{u^2}{2\sqrt{1-u^2}\left(1-\sqrt{1-n^2}\right)} - 1}\,. \tag{3.24}$$

3.2.3 Harmonic distortion in non-sinusoidal reference currents strategies

In the Appendix B: is analyzed the behavior of the power control strategies with non-sinusoidal reference currents and as can be seen in Fig. 3.3, obtained through the equations (3.17) and (3.24), the IARC and ICSP strategies present a high harmonic distortion is even for low unbalance voltages values.

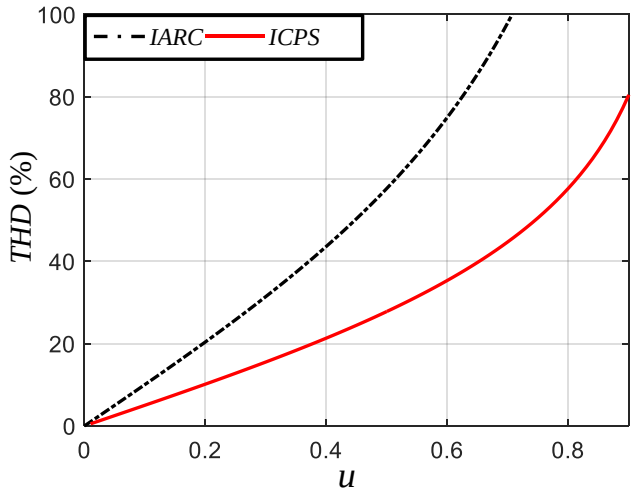

Fig. 3.3: Total harmonic distortion for non-sinusoidal power control strategies.
Source: Elaborated by the author

Due to the technical limitations listed in Appendix B:, the application of control strategies with non-sinusoidal reference currents becomes almost impracticable in multi-megawatts power generation systems. Hence, the IARC and ICSP are not addressed in the following studies carried out in this work.

3.3 Sinusoidal reference currents power control strategies

Some power control strategies with sinusoidal reference currents are proposed in literature. Even though they do not cancel the active and reactive power oscillation instantaneously, it is possible to achieve others power quality characteristics.

3.3.1 Average active and reactive control (AARC)

Instead the instantaneous voltage vector norm $|\mathbf{v}|$, it is possible to decompose the current in active and reactive parts using the collective root-mean square (RMS) norm $\|\mathbf{v}\|$ [52]. Since T is one cycle of fundamental period, $\|\mathbf{v}\|$ is defined by [14]:

$$\|\mathbf{v}\|^2 = \frac{1}{T}\int_0^T (v_a^2 + v_b^2 + v_c^2)dt = \frac{1}{T}\int_0^T |\mathbf{v}|^2 dt = |\mathbf{v}^+|^2 + |\mathbf{v}^-|^2. \tag{3.25}$$

The active and reactive reference currents are defined in the equations (3.26) and (3.27) , respectively. They are the smallest collective RMS value to deliver P^* and Q^* over one grid period [20].

$$\mathbf{i}_p^* = \frac{P^*}{\|\mathbf{v}\|^2}\,\mathbf{v} = G_e\,\mathbf{v} = \frac{P^*}{|\mathbf{v}^+|^2 + |\mathbf{v}^-|^2}\,(\mathbf{v}^+ + \mathbf{v}^-), \tag{3.26}$$

$$\mathbf{i}_q^* = \frac{Q^*}{\|\mathbf{v}\|^2}\,\mathbf{v}_\perp = B_e\,\mathbf{v}_\perp = \frac{Q^*}{|\mathbf{v}^+|^2 + |\mathbf{v}^-|^2}\,(\mathbf{v}_\perp^+ + \mathbf{v}_\perp^-), \tag{3.27}$$

G_e is the conductance and B_e susceptance of the asymmetrical load seen from the GSC output, which are constant within a period T. Consequently, $\mathbf{i}_p^*$ and $\mathbf{i}_q^*$ are directly proportional to the voltages $\mathbf{v}$ and $\mathbf{v}_\perp$, that is, unbalanced voltages will generate unbalanced currents.

Replacing the equations (3.26), (3.27) and (3.5) into (3.8) and (3.9), it is possible to obtain the instantaneous power generated by the AARC strategy:

$$\begin{aligned} p = \mathbf{v}\cdot\left(\mathbf{i}_p+\mathbf{i}_q\right) &= \frac{P^*}{|\mathbf{v}^+|^2+|\mathbf{v}^-|^2}\cdot\underbrace{\mathbf{v}\cdot\mathbf{v}}_{|\mathbf{v}|^2}+\frac{Q^*}{|\mathbf{v}^+|^2+|\mathbf{v}^-|^2}\cdot\underbrace{\mathbf{v}_\perp\cdot\mathbf{v}}_{0}=\cdots \\ &= P^*\left\{1+\frac{2|\mathbf{v}^+||\mathbf{v}^-|\cos(2\omega t+\phi^+-\phi^-)}{|\mathbf{v}^+|^2+|\mathbf{v}^-|^2}\right\}, \end{aligned} \tag{3.28}$$

$$\begin{aligned} q = \mathbf{v}_\perp\cdot\left(\mathbf{i}_p+\mathbf{i}_q\right) &= \frac{P^*}{|\mathbf{v}^+|^2+|\mathbf{v}^-|^2}\cdot\underbrace{\mathbf{v}\cdot\mathbf{v}_\perp}_{\mathbf{0}}+\frac{Q^*}{|\mathbf{v}^+|^2+|\mathbf{v}^-|^2}\cdot\underbrace{\mathbf{v}_\perp\cdot\mathbf{v}_\perp}_{|\mathbf{v}|^2}=\cdots \\ &Q^*\left\{1+\frac{2|\mathbf{v}^+||\mathbf{v}^-|\cos(2\omega t+\phi^+-\phi^-)}{|\mathbf{v}^+|^2+|\mathbf{v}^-|^2}\right\}. \end{aligned} \tag{3.29}$$

The values of p and q are composed of a mean and oscillatory terms with twice fundamental frequency that are proportional to the set-points values. It is possible to note that the AARC cancels the sine terms of instantaneous power oscillation (equations (3.12)), which creates a linear independence between the orthogonal power components, i.e., the active power oscillation relates only with P^* and the reactive power oscillations with Q^*.

3.3.2 Positive and negative sequence compensation (PNSC)

The PNSC [14,15] calculates a set of references with positive and negative sequence components, generating unbalanced currents. In a similar way from ICPS, it was proposed delivering only one of the power set-points during the voltage sag. This strategy aims to eliminate the power oscillations through the following constraints:

$$\left.\begin{aligned} P^* &= \mathbf{v}^+\cdot\mathbf{i}_p^+ + \mathbf{v}^-\cdot\mathbf{i}_p^- \\ 0 &= \mathbf{v}^+\cdot\mathbf{i}_p^- + \mathbf{v}^-\cdot\mathbf{i}_p^+ \end{aligned}\right\} \Longrightarrow\ \mathbf{i}_q = 0, \tag{3.30}$$

$$\left.\begin{aligned} Q^* &= \mathbf{v}_\perp^+\cdot\mathbf{i}_q^+ + \mathbf{v}_\perp^-\cdot\mathbf{i}_q^- \\ 0 &= \mathbf{v}_\perp^+\cdot\mathbf{i}_q^- + \mathbf{v}_\perp^-\cdot\mathbf{i}_q^+ \end{aligned}\right\} \Longrightarrow \mathbf{i}_p = 0. \tag{3.31}$$

According to (3.30) and (3.31), the mean value of the instantaneous powers results from the products of voltages and currents with the same sequence and the different sequences voltages and currents interactions must be eliminated. Thus, the active and reactive currents vectors are given by:

$$\mathbf{i}_p^* = \frac{P^*}{|\mathbf{v}^+|^2 - |\mathbf{v}^-|^2}\,(\mathbf{v}^+ - \mathbf{v}^-) = g^{\pm}\,(\mathbf{v}^+ - \mathbf{v}^-), \tag{3.32}$$

$$\mathbf{i}_q^* = \frac{Q^*}{|\mathbf{v}^+|^2 - |\mathbf{v}^-|^2}\,(\mathbf{v}_\perp^+ - \mathbf{v}_\perp^-) = b^{\pm}\,(\mathbf{v}_\perp^+ - \mathbf{v}_\perp^-), \tag{3.33}$$

where $g^{\pm}$ and $b^{\pm}$ are the PNSC positive/negative instantaneous conductance and susceptance, respectively. Replacing equations (3.30) and (3.31) in (3.8) and (3.9), the instantaneous powers produced by the PNSC are obtained:

$$p = (\mathbf{v}^+ + \mathbf{v}^-)\cdot\left(\mathbf{i}_p^+ + \mathbf{i}_p^- + \mathbf{i}_q^+ + \mathbf{i}_q^-\right) = \cdots$$
$$\underbrace{\mathbf{v}^+\cdot\mathbf{i}_p^+ + \mathbf{v}^-\cdot\mathbf{i}_p^-}_{P} + \underbrace{\mathbf{v}^+\cdot\mathbf{i}_q^+ + \mathbf{v}^-\cdot\mathbf{i}_q^-}_{0} + \underbrace{\mathbf{v}^-\cdot\mathbf{i}_p^+ + \mathbf{v}^+\cdot\mathbf{i}_p^-}_{0} + \underbrace{\mathbf{v}^+\cdot\mathbf{i}_q^- + \mathbf{v}^-\cdot\mathbf{i}_q^+}_{\tilde{p}}, \tag{3.34}$$

$$q = (\mathbf{v}_\perp^+ + \mathbf{v}_\perp^-)\cdot(\mathbf{i}_p^+ + \mathbf{i}_p^- + \mathbf{i}_q^+ + \mathbf{i}_q^-) = \cdots$$
$$\underbrace{\mathbf{v}_\perp^+\cdot\mathbf{i}_\mathrm{q}^+ + \mathbf{v}_\perp^+\cdot\mathbf{i}_\mathrm{q}^-}_{Q} + \underbrace{\mathbf{v}_\perp^+\cdot\mathbf{i}_\mathrm{p}^+ + \mathbf{v}_\perp^-\cdot\mathbf{i}_\mathrm{p}^-}_{0} + \underbrace{\mathbf{v}_\perp^-\cdot\mathbf{i}_\mathrm{q}^+ + \mathbf{v}_\perp^+\cdot\mathbf{i}_\mathrm{q}^-}_{0} + \underbrace{\mathbf{v}_\perp^+\cdot\mathbf{i}_\mathrm{p}^- + \mathbf{v}_\perp^-\cdot\mathbf{i}_\mathrm{p}^+}_{\tilde{q}}. \tag{3.35}$$

The PNSC objective is to suppress the cosine terms of the active and reactive powers oscillations in (3.11) and (3.12). However, with any of the two power set-points different from zero, the sine terms are still present, and the power oscillations are not null [34].

The equations (3.32) and (3.33) present a singular point in $|\mathbf{v}^+| = |\mathbf{v}^-|$, in other words, when the positive and negative sequence voltages become equal. This mean that it is physically impossible to cancel the power oscillations under extreme unbalanced voltages [34].

3.3.3 Balanced positive sequence control (BPSC)

The BPSC generates a set of perfectly balanced positive sequence currents with sinusoidal waveforms [14,15]. For this, only the positive sequence voltage vector is used to calculate the reference currents:

$$\mathbf{i}_p^* = \frac{P^*}{|\mathbf{v}^+|^2}\,\mathbf{v}^+ = G^+\,\mathbf{v}^+, \tag{3.36}$$

$$\mathbf{i}_q^* = \frac{Q^*}{|\mathbf{v}^+|^2}\,\mathbf{v}_\perp^+ = B^+\mathbf{v}_\perp^+. \tag{3.37}$$

The positive sequence conductance G^+ and susceptance B^+ are constant, and the currents are directly proportional to the positive sequence voltage. Since the BPSC produces sinusoidal currents through the positive sequence, it executes the exactly requirement by the actuals GCs and it can be considered the standard condition in the analyses realized in this

work. This strategy cannot cancel the power oscillation, except when $P^* = Q^* = 0$, as follows:

$$p = \underbrace{\mathbf{v}^+ \cdot \mathbf{i}_p^+}_{P} + \underbrace{\mathbf{v}^+ \cdot \mathbf{i}_q^+}_{0} + \underbrace{\mathbf{v}^- \cdot \mathbf{i}_p^+ + \mathbf{v}^- \cdot \mathbf{i}_q^+}_{\tilde{p}}, \tag{3.38}$$

$$q = \underbrace{\mathbf{v}_\perp^+ \cdot \mathbf{i}_\mathrm{q}^+}_{Q} + \underbrace{\mathbf{v}_\perp^+ \cdot \mathbf{i}_\mathrm{p}^+}_{0} + \underbrace{\mathbf{v}_\perp^- \cdot \mathbf{i}_\mathrm{q}^+ + \mathbf{v}_\perp^- \cdot \mathbf{i}_\mathrm{p}^+}_{\tilde{q}}. \tag{3.39}$$

3.3.4 Active (APOC) and reactive (RPOC) power oscillation cancel

The sinusoidal reference currents strategies previously presented are not able to cancel the powers oscillations when P^* and Q^* are simultaneously different from zero. However, the APOC can cancel the active and RPOC the reactive power oscillations, independent of the power set-point values. These strategies were proposed in [17] as a feature of the flexible approaches (which will be discussed in the next section). Nevertheless, in this work they are treated as independent strategies. The APOC reference currents are calculated by:

$$\mathbf{i}_p^* = \frac{P^*}{|\mathbf{v}^+|^2 - |\mathbf{v}^-|^2}\,(\mathbf{v}^+ - \mathbf{v}^-) = g^{\pm}\,(\mathbf{v}^+ - \mathbf{v}^-), \tag{3.40}$$

$$\mathbf{i}_q^* = \frac{Q^*}{|\mathbf{v}^+|^2 + |\mathbf{v}^-|^2}\,(\mathbf{v}_\perp^+ + \mathbf{v}_\perp^-) = b^{\pm}(\mathbf{v}_\perp^+ + \mathbf{v}_\perp^-), \tag{3.41}$$

where $g^{\pm}$ and $b^{\pm}$ are the positive and negative sequence conductance and susceptance. The APOC instantaneous power expressions are defined in equations (3.42) and (3.43). Despite the null active power oscillations, in the reactive power both sine and cosine power oscillation terms are present.

$$p = (\mathbf{v}^+ + \mathbf{v}^-) \cdot \left(\mathbf{i}_p^+ + \mathbf{i}_p^- + \mathbf{i}_q^+ + \mathbf{i}_q^-\right) = \cdots$$
$$\underbrace{\mathbf{v}^+ \cdot \mathbf{i}_p^+ + \mathbf{v}^- \cdot \mathbf{i}_p^-}_{P} + \underbrace{\mathbf{v}^+ \cdot \mathbf{i}_q^+ + \mathbf{v}^- \cdot \mathbf{i}_q^-}_{0} + \underbrace{\mathbf{v}^- \cdot \mathbf{i}_p^+ + \mathbf{v}^+ \cdot \mathbf{i}_p^- + \mathbf{v}^+ \cdot \mathbf{i}_q^- + \mathbf{v}^- \cdot \mathbf{i}_q^+}_{0}, \tag{3.42}$$

$$q = (\mathbf{v}_\perp^+ + \mathbf{v}_\perp^-) \cdot (\mathbf{i}_p^+ + \mathbf{i}_p^- + \mathbf{i}_q^+ + \mathbf{i}_q^-) = \cdots$$
$$\underbrace{\mathbf{v}_\perp^+ \cdot \mathbf{i}_\mathrm{q}^+ + \mathbf{v}_\perp^+ \cdot \mathbf{i}_\mathrm{q}^-}_{Q} + \underbrace{\mathbf{v}_\perp^+ \cdot \mathbf{i}_\mathrm{p}^+ + \mathbf{v}_\perp^- \cdot \mathbf{i}_\mathrm{p}^-}_{0} + \underbrace{\mathbf{v}_\perp^- \cdot \mathbf{i}_\mathrm{q}^+ + \mathbf{v}_\perp^+ \cdot \mathbf{i}_\mathrm{q}^- + \mathbf{v}_\perp^+ \cdot \mathbf{i}_\mathrm{p}^- + \mathbf{v}_\perp^- \cdot \mathbf{i}_\mathrm{p}^+}_{\tilde{q}}. \tag{3.43}$$

The RPOC reference currents expressions are given by

$$\mathbf{i}_p^* = \frac{P^*}{|\mathbf{v}^+|^2 + |\mathbf{v}^-|^2}\,(\mathbf{v}^+ + \mathbf{v}^-) = g^{\pm}\,(\mathbf{v}^+ + \mathbf{v}^-), \tag{3.44}$$

$$\mathbf{i}_q^* = \frac{Q^*}{|\mathbf{v}^+|^2 - |\mathbf{v}^-|^2}\,(\mathbf{v}_\perp^+ - \mathbf{v}_\perp^-) = b^{\pm}(\mathbf{v}_\perp^+ - \mathbf{v}_\perp^-). \tag{3.45}$$

The RPOC instantaneous powers are described in equations (3.45) and (3.46). In complementary way from the APOC, the RPOC presents null reactive power oscillations,

however the active power sine and cosine terms are present in the active instantaneous power expression.

$$p = (\mathbf{v}^+ + \mathbf{v}^-) \cdot \left(\mathbf{i}_p^+ + \mathbf{i}_p^- + \mathbf{i}_q^+ + \mathbf{i}_q^-\right) = \cdots$$
$$\underbrace{\mathbf{v}^+ \cdot \mathbf{i}_p^+ + \mathbf{v}^- \cdot \mathbf{i}_p^-}_{P} + \underbrace{\mathbf{v}^+ \cdot \mathbf{i}_q^+ + \mathbf{v}^- \cdot \mathbf{i}_q^-}_{0} + \underbrace{\mathbf{v}^- \cdot \mathbf{i}_p^+ + \mathbf{v}^+ \cdot \mathbf{i}_p^- + \mathbf{v}^+ \cdot \mathbf{i}_q^- + \mathbf{v}^- \cdot \mathbf{i}_q^+}_{\tilde{p}}, \tag{3.46}$$

$$q = (\mathbf{v}_\perp^+ + \mathbf{v}_\perp^-) \cdot (\mathbf{i}_p^+ + \mathbf{i}_p^- + \mathbf{i}_q^+ + \mathbf{i}_q^-) = \cdots$$
$$\underbrace{\mathbf{v}_\perp^+ \cdot \mathbf{i}_\mathrm{q}^+ + \mathbf{v}_\perp^+ \cdot \mathbf{i}_\mathrm{q}^-}_{Q} + \underbrace{\mathbf{v}_\perp^+ \cdot \mathbf{i}_\mathrm{p}^+ + \mathbf{v}_\perp^- \cdot \mathbf{i}_\mathrm{p}^-}_{0} + \underbrace{\mathbf{v}_\perp^- \cdot \mathbf{i}_\mathrm{q}^+ + \mathbf{v}_\perp^+ \cdot \mathbf{i}_\mathrm{q}^- + \mathbf{v}_\perp^+ \cdot \mathbf{i}_\mathrm{p}^- + \mathbf{v}_\perp^- \cdot \mathbf{i}_\mathrm{p}^+}_{0}. \tag{3.47}$$

The APOC and RPOC generate reference currents composed of positive and negative sequence, i.e. unbalanced currents. Although they enable to cancel the ripple in the active or reactive power; its in-quadrature component is affected by high magnitude power oscillations. Moreover, it is possible to note that they also present the same singular point at $|\mathbf{v}^+| = |\mathbf{v}^-|$ observed in the PNSC strategy, consequently it is impossible to cancel the power oscillations under extreme unbalanced situations.

3.4 Flexible power control strategies

The flexible approaches use gains to weight the relation between the positive and negative sequence currents, allowing to reach different power quality characteristics. Several flexible power control strategies are proposed in literature and some of them are presented in [16–19]. In [18] for example, the operation of the GSC can be programed by setting two continuous control parameters, consequently the active and reactive power ripple and harmonic distortion can be adjusted. However, as previously discussed, the harmonic content is not a desirable characteristic and this work is focused in control strategies with sinusoidal currents.

Reference [16] presents the flexible positive and negative sequence control (FPNSC), where by means of changes the values of k_1 and k_2 in equations (3.48) and (3.49) ($0 \leq k_1 \leq 1$ and $0 \leq k_2 \leq 1$), it is possible the change the relationship between the positive and negative sequence in both active and reactive currents.

$$\mathbf{i}_p^* = P^* \left(\frac{k_1}{|\mathbf{v}^+|^2}\, \mathbf{v}^+ + \frac{(1-k_1)}{|\mathbf{v}^-|^2} \mathbf{v}^- \right), \tag{3.48}$$

$$\mathbf{i}_q^* = Q^* \left(\frac{k_2}{|\mathbf{v}^+|^2}\, \mathbf{v}_\perp^+ + \frac{(1-k_2)}{|\mathbf{v}^-|^2}\, \mathbf{v}_\perp^- \right). \tag{3.49}$$

The pliant active and reactive power control (PARPC) is proposed in [17]. The positive and negative sequence connection is controlled by the coefficients k_p for active and k_q for the reactive current in equations (3.50) and (3.51) ($-1 \leq k_p \leq 1$ and $-1 \leq k_q \leq 1$).

$$\mathbf{i}_p^* = \frac{P^*}{|\mathbf{v}^+|^2 + k_p|\mathbf{v}^-|^2}\left(\mathbf{v}^+ + k_p\,\mathbf{v}^-\right), \tag{3.50}$$

$$\mathbf{i}_q^* = \frac{Q^*}{|\mathbf{v}^+|^2 + k_q|\mathbf{v}^-|^2}\left(\mathbf{v}_\perp^+ + k_q\,\mathbf{v}_\perp^-\right). \tag{3.51}$$

Finally, a more general flexible method is proposed in [19] and will be called here as generalized flexible power control (GFPC). It presents four degrees of freedom though the gains k_p^+, k_p^-, k_q^+ and k_q^- according to the equations (3.52) and (3.53) ($0 \leq k_p^+ \leq 1$, $-1 \leq k_p^- \leq 1$, $0 \leq k_q^+ \leq 1$ and $-1 \leq k_q^- \leq 1$).

$$\mathbf{i}_p^* = \frac{P^*}{k_p^+\,|\mathbf{v}^+|^2 + k_p^-\,|\mathbf{v}^-|^2}\left(k_p^+\,\mathbf{v}^+ + k_p^-\,\mathbf{v}^-\right), \tag{3.52}$$

$$\mathbf{i}_q^* = \frac{Q^*}{k_q^+\,|\mathbf{v}^+|^2 + k_q^-\,|\mathbf{v}^-|^2}\left(k_q^+\,\mathbf{v}_\perp^+ + k_q^-\,\mathbf{v}_\perp^-\right). \tag{3.53}$$

The flexible power control strategies previously mentioned can emulate any of the control methods that generate sinusoidal reference currents early discussed. In fact, due to the greater GFPC freedom degree, it can even emulate other flexible strategies, as demonstrated in Table II. The correlation among the flexible power control strategies can be obtained equating the GFPC, PARPC and FPNSC relations, and it is one contributions of this work.

Since the flexible strategies power oscillation equations are one of the main contributions of this text, they will be better detailed in the next chapter.

3.5 Chapter conclusion

During unbalanced faults, the imbalance between the mains phase voltages generates instantaneous power oscillations with twice of the fundamental frequency. It is possible to generate different currents profiles through the power control strategies, which allows to reduce or even cancel the power ripple during the unbalanced voltage sag. In this chapter is presented some of the main power control methods proposed in literature, where they can be divided in sinusoidal and non-sinusoidal strategies.

The Non-sinusoidal reference currents power control strategies presented in this work allows to reduce or simultaneously cancel the active and reactive power ripple. However, a

high harmonic content, which is proportional to phase voltage unbalance, is inserted to the reference currents. Hence, technical limitations make impracticable the implementation of non-sinusoidal power control strategies in multi-megawatts power converters, and they are not addressed in the following studies carried out in this work.

The sinusoidal reference currents strategies do not cancel concurrently the active and reactive power oscillations. Nonetheless, they present other very interesting features such as active or reactive power ripple cancel, conduction losses reduction, balanced currents, etc. A comparative summary of the sinusoidal reference currents sinusoidal analyzed in this work is presented in Table III.

The flexible approaches using weight gains that allow to achieve different power qualities characteristics, include to emulate other power control strategies. This characteristic makes the flexible power control strategies an excellent alternative to elaborate more generalized equations allowing a more comprehensive analysis, as it will be shown in the following chapters.

Table II: Flexible and sinusoidal power control strategies relation

	FPNSC [16]		**PARPC** [17]		**GFPC** [19]			
Strategy	k_1	k_2	k_p	k_q	k_p^+	k_p^-	k_q^+	k_q^-
AARC	$\frac{1}{1+u^2}$	$\frac{1}{1+u^2}$	1	1	1	1	1	1
PNSC	$\frac{1}{1-u^2}$	$\frac{1}{1-u^2}$	-1	-1	1	-1	1	-1
BPSC	1	1	0	0	1	0	1	0
APOC	$\frac{1}{1-u^2}$	$\frac{1}{1+u^2}$	-1	1	1	-1	1	1
RPOC	$\frac{1}{1+u^2}$	$\frac{1}{1-u^2}$	1	-1	1	1	1	-1
PARPC	$\frac{1}{1+k_p u^2}$	$\frac{1}{1+k_q u^2}$	$-$	$-$	1	k_p	1	k_q
FPNSC	$-$	$-$	$\frac{1-k_1}{u^2 k_1}$	$\frac{1-k_2}{u^2 k_2}$	1	$\frac{1-k_1}{u^2 k_1}$	1	$\frac{1-k_2}{u^2 k_2}$

Source: Elaborated by the author

Table III: Comparative summary of the sinusoidal reference currents power control strategies.

Strategy	Active reference	Reactive reference	Characteristics
AARC	$\mathbf{i}_p^{+*} = \frac{P^*}{\lvert\mathbf{v}^+\rvert^2 + \lvert\mathbf{v}^-\rvert^2}\,\mathbf{v}^+$ $\mathbf{i}_p^{-*} = \frac{P^*}{\lvert\mathbf{v}^+\rvert^2 + \lvert\mathbf{v}^-\rvert^2}\,\mathbf{v}^-$	$\mathbf{i}_q^{+*} = \frac{Q^*}{\lvert\mathbf{v}^+\rvert^2 + \lvert\mathbf{v}^-\rvert^2}\,\mathbf{v}_\perp^+$ $\mathbf{i}_q^{-*} = \frac{Q^*}{\lvert\mathbf{v}^+\rvert^2 + \lvert\mathbf{v}^-\rvert^2}\,\mathbf{v}_\perp^-$	• Unbalanced currents. • Cancels the sine terms of the instantaneous power oscillations; • It always has active power oscillations, except when $P^* = 0$; • It always has reactive power oscillations, except when $Q^* = 0$; • The reference currents computed result in the smallest collective RMS value to deliver P^* and Q^* over one grid period.
PNSC	$\mathbf{i}_p^{+*} = \frac{P^*}{\lvert\mathbf{v}^+\rvert^2 - \lvert\mathbf{v}^-\rvert^2}\,\mathbf{v}^+$ $\mathbf{i}_p^{-*} = \frac{-P^*}{\lvert\mathbf{v}^+\rvert^2 - \lvert\mathbf{v}^-\rvert^2}\,\mathbf{v}^-$	$\mathbf{i}_q^{+*} = \frac{Q^*}{\lvert\mathbf{v}^+\rvert^2 - \lvert\mathbf{v}^-\rvert^2}\,\mathbf{v}_\perp^+$ $\mathbf{i}_q^{-*} = \frac{-Q^*}{\lvert\mathbf{v}^+\rvert^2 - \lvert\mathbf{v}^-\rvert^2}\,\mathbf{v}_\perp^-$	• Unbalanced currents; • Cancels the cosine terms of the instantaneous power oscillations; • Singular point at $\lvert\mathbf{v}^+\rvert = \lvert\mathbf{v}^-\rvert$; • Cancels the active power oscillations only if $Q^* = 0$; • Cancels the reactive power oscillations only if $P^* = 0$.
BPSC	$\mathbf{i}_p^{+*} = \frac{P^*}{\lvert\mathbf{v}^+\rvert^2}\,\mathbf{v}^+$ $\mathbf{i}_p^{-*} = 0$	$\mathbf{i}_q^{+*} = \frac{Q^*}{\lvert\mathbf{v}^+\rvert^2}\,\mathbf{v}_\perp^+$ $\mathbf{i}_q^{-*} = 0$	• Balanced currents; • It always has active and reactive power; • oscillations, except when $P^* = Q^* = 0$.
APOC	$\mathbf{i}_p^{+*} = \frac{P^*}{\lvert\mathbf{v}^+\rvert^2 - \lvert\mathbf{v}^-\rvert^2}\,\mathbf{v}^+$ $\mathbf{i}_p^{-*} = \frac{-P^*}{\lvert\mathbf{v}^+\rvert^2 - \lvert\mathbf{v}^-\rvert^2}\,\mathbf{v}^-$	$\mathbf{i}_q^{+*} = \frac{Q^*}{\lvert\mathbf{v}^+\rvert^2 + \lvert\mathbf{v}^-\rvert^2}\,\mathbf{v}_\perp^+$ $\mathbf{i}_q^{-*} = \frac{Q^*}{\lvert\mathbf{v}^+\rvert^2 + \lvert\mathbf{v}^-\rvert^2}\,\mathbf{v}_\perp^-$	• Unbalanced currents; • No active power oscillation; • Singular point at $\lvert\mathbf{v}^+\rvert = \lvert\mathbf{v}^-\rvert$; • It always has reactive power oscillations, except when $P^* = Q^* = 0$; • Presents the sine and cosine terms of the reactive instantaneous power oscillation.
RPOC	$\mathbf{i}_p^{+*} = \frac{P^*}{\lvert\mathbf{v}^+\rvert^2 + \lvert\mathbf{v}^-\rvert^2}\,\mathbf{v}^+$ $\mathbf{i}_p^{-*} = \frac{P^*}{\lvert\mathbf{v}^+\rvert^2 + \lvert\mathbf{v}^-\rvert^2}\,\mathbf{v}^-$	$\mathbf{i}_q^{+*} = \frac{Q^*}{\lvert\mathbf{v}^+\rvert^2 - \lvert\mathbf{v}^-\rvert^2}\,\mathbf{v}_\perp^+$ $\mathbf{i}_q^{-*} = \frac{-Q^*}{\lvert\mathbf{v}^+\rvert^2 - \lvert\mathbf{v}^-\rvert^2}\,\mathbf{v}_\perp^-$	• Unbalanced currents; • No reactive power oscillations; • Singular point at $\lvert\mathbf{v}^+\rvert = \lvert\mathbf{v}^-\rvert$; • It always has active power oscillations, except when $P^* = Q^* = 0$; • Presents the sine and cosine terms of the active instantaneous power oscillation.

Source: Elaborated by the author

Chapter IV

VOLTAGE SAG EFFECTS ON GRID CONVERTERS

IN this chapter, it is discussed the effects of power oscillations, generated by the previously presented power control strategies on the grid-connected converters. For this, equations that quantify the steady state power oscillation magnitude for the sinusoidal reference currents strategies (AARC, PNSC, BPSC, APOC and RPOC) using the GFPC strategy as basis are proposed and it is also approached equations that relates the active power oscillation and d.c. bus voltage ripple. Finally, a case study with a simulation of a 2(MW) WEC is performed in order to analyze the strategies behavior in terms of power fluctuation and converter d.c. bus impacts, where different points over the RCI curve, defined in the actual grid codes, are evaluated.

4.1 Generalized power oscillation analysis

It is possible to develop a general expression that quantifies instantaneous power oscillations for the sinusoidal reference currents strategies previously described. For this, it is replaced the GFPC currents expression (equations (3.52) and (3.53)) in the oscillation terms of the instantaneous power (equations (3.8) and (3.9)):

$$\begin{aligned}\tilde{p} = {} & \mathbf{v}^- \cdot \underbrace{\left(\frac{P^* \, k_p^+ \, \mathbf{v}^+}{k_p^+ \, |\mathbf{v}^+|^2 + k_p^- \, |\mathbf{v}^-|^2}\right)}_{i_p^+} + \mathbf{v}^+ \cdot \underbrace{\left(\frac{P^* \, k_p^- \, \mathbf{v}^-}{k_p^+ \, |\mathbf{v}^+|^2 + k_p^- \, |\mathbf{v}^-|^2}\right)}_{i_p^-} + \cdots \\ & \mathbf{v}^+ \cdot \underbrace{\left(\frac{Q^* k_q^- \, \mathbf{v}_\perp^-}{k_q^+ \, |\mathbf{v}^+|^2 + k_q^- \, |\mathbf{v}^-|^2}\right)}_{i_q^-} + \mathbf{v}^- \cdot \underbrace{\left(\frac{Q^* k_q^+ \, \mathbf{v}_\perp^+}{k_q^+ \, |\mathbf{v}^+|^2 + k_q^- \, |\mathbf{v}^-|^2}\right)}_{i_q^+},\end{aligned} \tag{4.1}$$

$$\begin{aligned}\tilde{q} = {} & \mathbf{v}_\perp^- \cdot \underbrace{\left(\frac{Q^* k_q^+ \, \mathbf{v}_\perp^+}{k_q^+ \, |\mathbf{v}^+|^2 + k_q^- \, |\mathbf{v}^-|^2}\right)}_{i_q^+} + \mathbf{v}_\perp^+ \cdot \underbrace{\left(\frac{Q^* k_q^- \, \mathbf{v}_\perp^-}{k_q^+ \, |\mathbf{v}^+|^2 + k_q^- \, |\mathbf{v}^-|^2}\right)}_{i_q^-} + \cdots \\ & \mathbf{v}_\perp^+ \cdot \underbrace{\left(\frac{P^* \, k_p^- \, \mathbf{v}^-}{k_p^+ \, |\mathbf{v}^+|^2 + k_p^- \, |\mathbf{v}^-|^2}\right)}_{i_p^-} + \mathbf{v}_\perp^- \cdot \underbrace{\left(\frac{P^* \, k_p^+ \, \mathbf{v}^+}{k_p^+ \, |\mathbf{v}^+|^2 + k_p^- \, |\mathbf{v}^-|^2}\right)}_{i_p^+}.\end{aligned} \tag{4.2}$$

The orthogonal principle results in the following propriety:

$$\mathbf{v}_{\perp} \cdot \mathbf{v} = (\mathbf{v}_{\perp}^{+} + \mathbf{v}_{\perp}^{-}) \cdot (\mathbf{v}^{+} + \mathbf{v}^{-}) = 0 \Longrightarrow \mathbf{v}_{\perp}^{+} \cdot \mathbf{v}^{-} = -\mathbf{v}_{\perp}^{-} \cdot \mathbf{v}^{+}, \tag{4.3}$$

Therefore, the power oscillation for the GFPC strategy is defined by:

$$\tilde{p} = \left(\frac{(k_p^+ + k_p^-)P^*}{k_p^+ \, |\mathbf{v}^+|^2 + k_p^- \, |\mathbf{v}^-|^2}\right)\mathbf{v}^+ \cdot \, \mathbf{v}^- + \left(\frac{(k_q^+ - k_q^-)Q^*}{k_q^+ \, |\mathbf{v}^+|^2 + k_q^- \, |\mathbf{v}^-|^2}\right)\mathbf{v}_{\perp}^+ \cdot \mathbf{v}^-, \tag{4.4}$$

$$\tilde{q} = \left(\frac{(k_q^+ + k_q^-)\, Q^*}{k_q^+ \, |\mathbf{v}^+|^2 + k_q^- \, |\mathbf{v}^-|^2}\right)\mathbf{v}_{\perp}^+ \cdot \mathbf{v}_{\perp}^- - \left(\frac{(k_p^+ - k_p^-)\, P^*}{k_p^+ \, |\mathbf{v}^+|^2 + k_p^- \, |\mathbf{v}^-|^2}\right)\mathbf{v}_{\perp}^+ \cdot \mathbf{v}^-. \tag{4.5}$$

Using the stationary frame voltage equations (3.3) in (4.4) and (4.5), the temporal expressions of GFPC power ripple are found:

$$\begin{aligned}\tilde{p} = &\left(\frac{(k_p^+ + k_p^-)|\mathbf{v}^+||\mathbf{v}^-|\cos(2\omega t + \phi^+ - \phi^-)}{k_p^+ \, |\mathbf{v}^+|^2 + k_p^- \, |\mathbf{v}^-|^2}\right)P^* + \cdots \\ &\left(\frac{(k_q^+ - k_q^-)|\mathbf{v}^+||\mathbf{v}^-|\sin(2\omega t + \phi^+ - \phi^-)}{k_q^+ \, |\mathbf{v}^+|^2 + k_q^- \, |\mathbf{v}^-|^2}\right)Q^*,\end{aligned} \tag{4.6}$$

$$\begin{aligned}\tilde{q} = &\left(\frac{(k_q^+ + k_q^-)|\mathbf{v}^+||\mathbf{v}^-|\cos(2\omega t + \phi^+ - \phi^-)}{k_q^+ \, |\mathbf{v}^+|^2 + k_q^- \, |\mathbf{v}^-|^2}\right)\, Q^* - \cdots \\ &\left(\frac{(k_p^+ - k_p^-)\, |\mathbf{v}^+||\mathbf{v}^-|\sin(2\omega t + \phi^+ - \phi^-)}{k_p^+ \, |\mathbf{v}^+|^2 + k_p^- \, |\mathbf{v}^-|^2}\right)P^*.\end{aligned} \tag{4.7}$$

In (4.6) and (4.7) the products between the parallel voltages and currents with different sequences result in power oscillations aligned to the cosine function, while the products of orthogonal voltages and currents with different sequences produce power oscillations aligned to the sine functions, in agreement with the equations (3.11) and (3.12).

The orthogonal relation in the terms of equations (4.6) and (4.7) makes possible to obtain the power oscillation magnitude through the quadratic sum, as follows:

$$\|\tilde{p}\| = u\sqrt{\left(\frac{(k_p^+ + k_p^-)P^*}{k_p^+ + k_p^- \, u^2}\right)^2 + \left(\frac{(k_q^+ - k_q^-)Q^*}{k_q^+ + k_q^- \, u^2}\right)^2}, \tag{4.8}$$

$$\|\tilde{q}\| = u\sqrt{\left(\frac{(k_q^+ + k_q^-)Q^*}{k_q^+ + k_q^- \, u^2}\right)^2 + \left(\frac{(k_p^+ - k_p^-)\, P^*}{k_p^+ + k_p^- \, u^2}\right)}. \tag{4.9}$$

To observe the effects of weight gains and power set-point variations in the oscillation magnitude, the power set-points were shifted, keeping the total power bounded by 1(pu), without taking in consideration the converter current limitation during the voltage sag. The

weight gains are changed in order to contemplate the strategies AARC, BPSC and PNSC in accordance to the Table II, i.e., $-1 \leq k_p^- = k_q^- \leq 1$ and $k_p^+ = k_q^+ = 1$. The active and reactive power oscillation magnitudes are show in Fig. 4.1.

The AARC presents the powers ripple proportional to the P^* and Q^*set-point values, which corroborate to the statements established in the previous chapter about the independence of active and reactive power oscillations. The PNSC has a complementary behavior in relation to the AARC, since the powers oscillations increase proportionally with the value of its orthogonal component, in other words, the raise of active power increases the reactive power oscillation and the rise of reactive power intensifies the active power ripple. Considering fixed P^* and Q^*, for small values of u the AARC and PNSC have very similar behaviors. Nevertheless, as u tends to 1 the power oscillation for the PNSC strategy has an expressive increase in relation to AARC, due to the approximation to the singular point $|\mathbf{v}^+| = |\mathbf{v}^-|$. The BPSC power oscillation is constant, because it is proportional to the unbalance factor and dependent on the total feed-in power to the grid.

The previous analyses can be extended to other control strategies, such as APOC and RPOC. Similar to the earlier case, the powers set-point were shifted keeping the total power bounded by 1(pu), without taking in consideration the converter current limitation. However, in a manner that is possible to cancel the powers oscillations, the gains are changed as $-1 \leq k_p^- = -k_q^- \leq 1$ and $k_p^+ = k_q^+ = 1$. The results are presented in Fig. 4.2.

When the active power cancellation (APOC) is reached in Fig. 4.2(a), the largest values of $\|\tilde{q}\|$ can be observed in Fig. 4.2(b), where the worst situation happens when $Q^* = 0$ and $P^* = 1$(pu). The opposite of earlier condition is experimented when the reactive power oscillation is cancelled (RPOC) in Fig. 4.2(b) and the highest values of $\|\tilde{p}\|$ can be seen in Fig. 4.2(a), where the worst case is observed with $P^* = 0$ and $Q^* = 1$.

In the similar way to the PNSC, when u tends to 1 the APOC and RPOC powers fluctuations has an expressive increase, due to the approximation to the singular point $|\mathbf{v}^+| = |\mathbf{v}^-|$ in the current reference calculation.

The previous analysis about the power magnitude can be better understood by replacing the weight gains of the GFPC strategy, presented in Table II, in the equations (4.6) and (4.7). Table IV describes the power oscillation magnitude from the power control strategies with sinusoidal reference currents, as function of the unbalanced factor u and set-points P^* and Q^*.

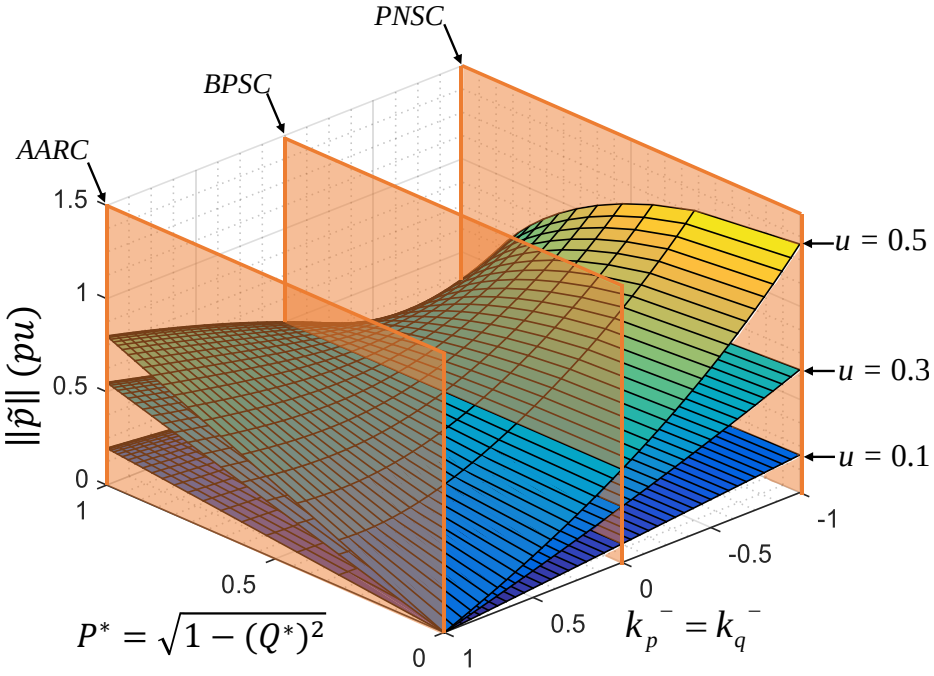

(a)

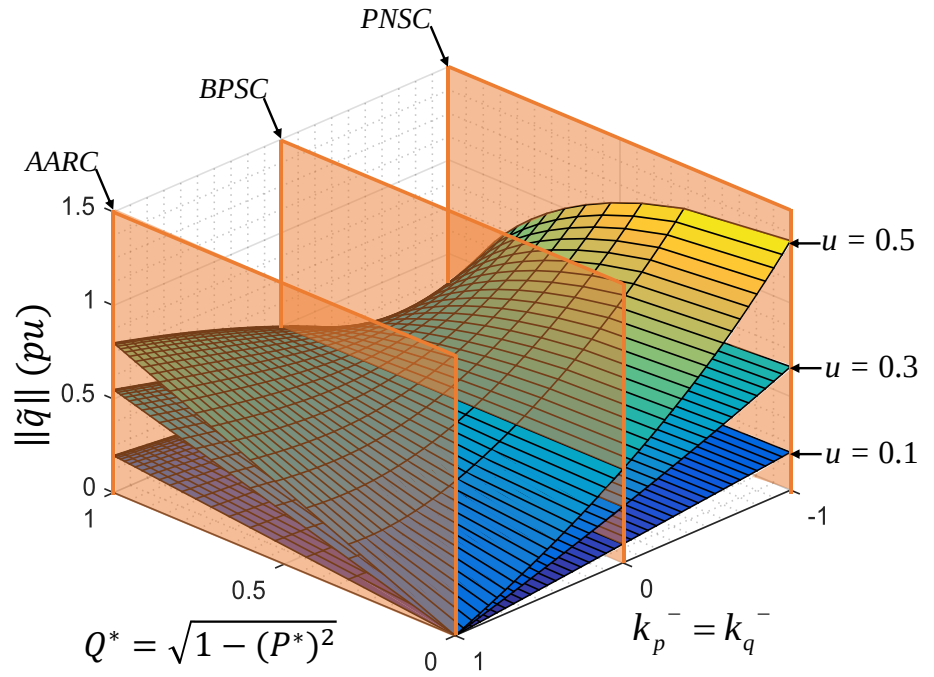

(b)

Fig. 4.1: Flexible (a) active and (b) reactive power oscillation magnitude for $k_p^+ = k_q^+ = 1$ and $k_p^- = k_q^-$.
Source: Elaborated by the author

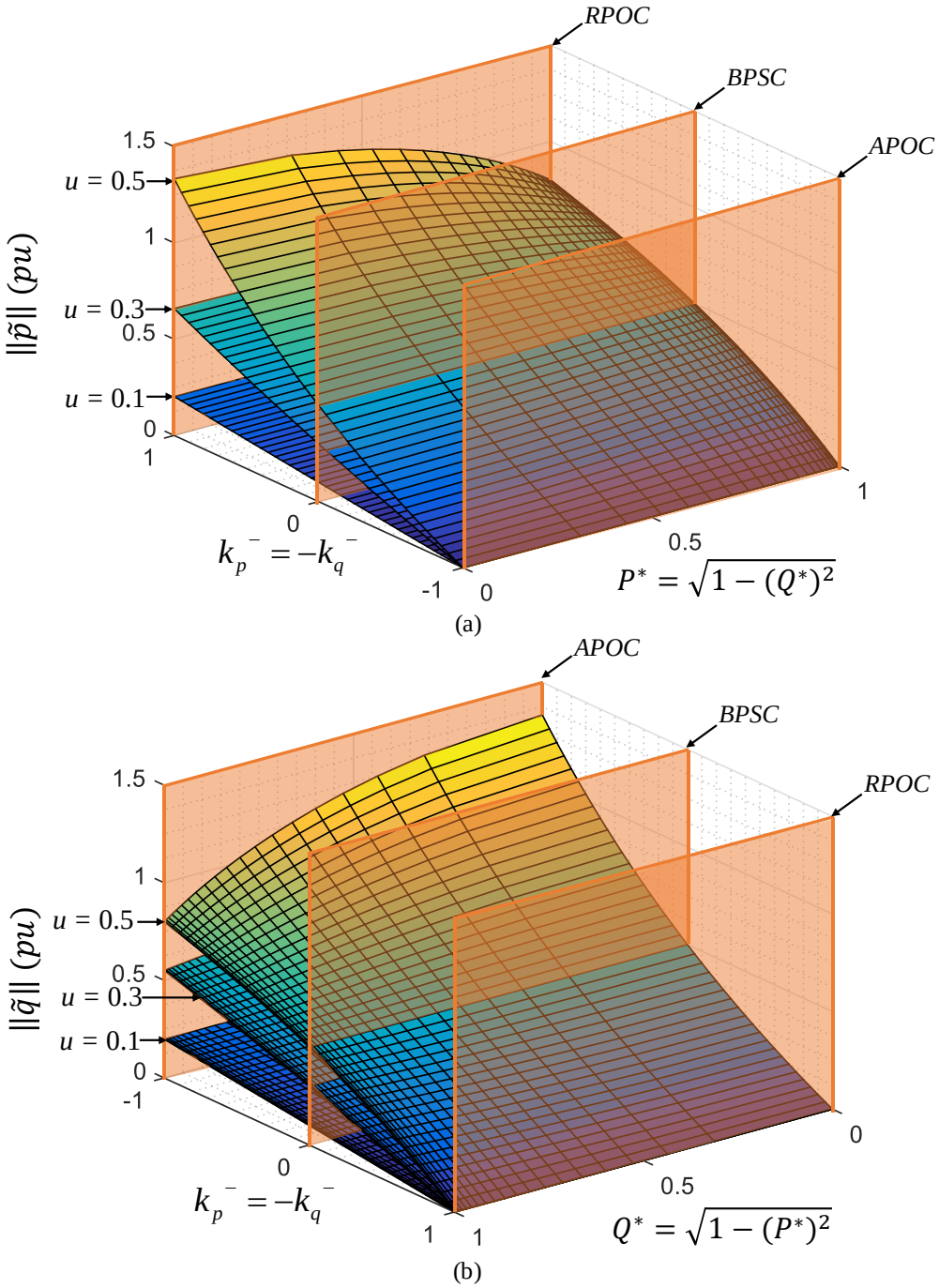

Fig. 4.2: Flexible (a) active and (b) reactive power oscillation magnitude for $k_p^+ = k_q^+ = 1$ and $k_p^- = -k_q^-$.
Source: Elaborated by the author

When it is compared the AARC and PNSC with APOC and RPOC magnitudes in Table IV, the strategies PNSC and AARC have the same behavior of each individual term of APOC and RPOC. Hence, in spite of the APOC and RPOC ripple cancellation in one of the power portions, its in-quadrature component will present high oscillations values.

.

Table IV: Instantaneous power oscillation magnitude

Strategy	$\|\tilde{p}\|$	$\|\tilde{q}\|$
AARC	$\frac{2u}{1+u^2}P^*$	$\frac{2u}{1+u^2}Q^*$
PNSC	$\frac{2u}{1-u^2}Q^*$	$\frac{2u}{1-u^2}P^*$
BPSC	$u\sqrt{(P^*)^2+(Q^*)^2}$	$u\sqrt{(P^*)^2+(Q^*)^2}$
APOC	0	$u\sqrt{\left(\frac{2\,u\,Q^*}{1+u^2}\right)^2+\left(\frac{2\,u\,P^*}{1-u^2}\right)^2}$
RPOC	$u\sqrt{\left(\frac{2\,u\,P^*}{1+u^2}\right)^2+\left(\frac{2\,u\,Q^*}{1-u^2}\right)^2}$	0

Source: Elaborated by the author

4.2 DC bus capacitors losses

From the power control strategies already presented, the following power quality characteristics can be obtained:

- Sinusoidal and balanced currents (BPSC);
- Optimized set of RMS currents to deliver the powers set-points P^* and Q^* (AARC);
- Cancellation of active power ripple (APOC);
- Cancellation of reactive power ripple (RPOC).

To investigate which is the best feature to be used to reduce voltage sag effects to the grid converter, a set of characteristics must be analyzed. In this section an overview discussion in relation to one of these characteristics is evaluated, that is the d.c. bus capacitors losses.

The d.c. bus capacitors are storage elements responsible for balancing the energy input from the primary source and the a.c. output power, absorbing the instantaneous difference between them [53,54]. They also damp the high switching frequency ripple of the pulse-width modulation (PWM) converters [53]. During transient conditions, such as voltage sags, the link capacitors are subjected to large energy variations and in many times they are also exposed to hostile environmental conditions such as, high temperature and humidity. Thus, they have been shown to be one of the main limitation factors in renewable source converters life time [54].

The d.c. link design requires the matching of available characteristics and parameters to the specific applications needs, under various environmental conditions, thermal, electrical and mechanical stress [54]. In a real electrolytic capacitor, in addition to their capacitance *C*, they

are composed of other parasitic elements inherent of their manufacturing, such as the equivalent series resistance (*ESR*) and the equivalent series inductance (*ESL*). Fig. 4.3 presents electrolytic capacitor equivalent model.

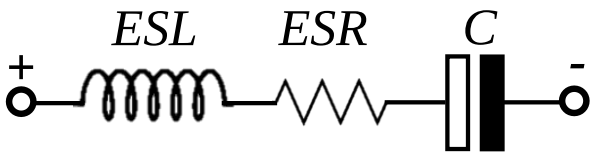

Fig. 4.3: Electrolytic capacitor equivalent model.
Source: Elaborated by the author

The dissipated power in an d.c. link capacitor P_{loss} is mainly composed by the resistive P_R and dielectric P_D power loses [55]. The *ESR* value refers to the hot spot and represents the equivalent parasitic resistance in the capacitor electrodes and contacts, where it is dependent on the current frequency ripple. Consequently, the resistive power dissipation from the joule effect is defined by:

$$P_R = \sum_{f=1}^{n} ESR_f \left(I_f^{\sim}\right)^2, \tag{4.10}$$

where ESR_f is the equivalent resistance and $I_f^{\sim}$ the RMS current ripple for the frequency f. Fig. 4.4 illustrates the typical behavior of an electrolytic capacitor *ESR* and permissible current ripple as a function of the frequency variation. The equivalent resistance tends to decline with the frequency and consequently, the low frequency current ripple generates higher losses. Thus, the permissible current ripple $I_f^{\sim}$ tends to decrease with the frequency, in order to keep the capacitor losses within its nominal value.

The dielectric losses have the peak of a symmetrical alternating voltage as the most significant factor, and they are defined by [55]:

$$P_D = \hat{u}_{ac}\, \pi\, f_0\, C \tan(\delta_0), \tag{4.11}$$

where $\hat{u}_{ac}$ is the peak value of symmetrical a.c. voltage and f_0 is the a.c. voltage ripple frequency, that are measured according to the Fig. 4.5, $\tan(\delta_0)$ is the dissipation factor of dielectric and its define the energy waste to polarize and repolarize the dielectric in two opposite directions for successive half cycles of the a.c. voltage [55].

The increase of power losses in the d.c. bus capacitor raises its operation temperature that can lead to values above to the safe operation region, causing the dielectric deterioration and consequently, having a direct impact on the capacitor life time reduction. Thus, the manufactures recommend a derating in the maximum capacitor rated voltage as a function of

the operation temperature. Hence, the current ripple and voltage oscillation is a serious issue during the unbalanced voltage sags.

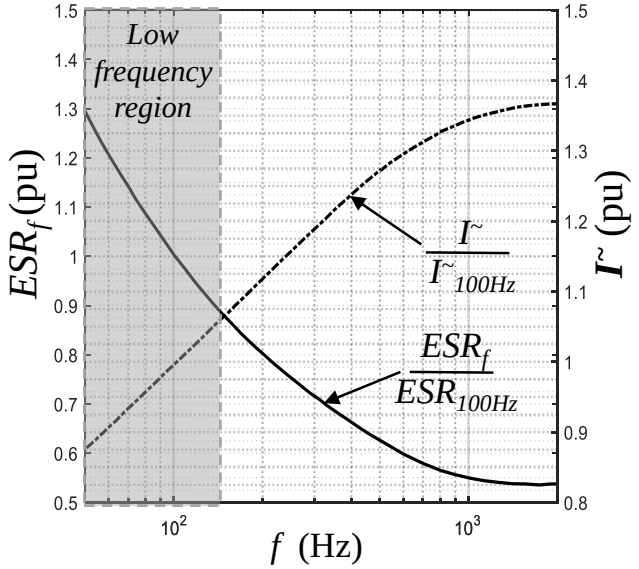

Fig. 4.4: Typical behavior of frequency characteristics of ESR and permissible current ripple.
Source: Elaborated by the author

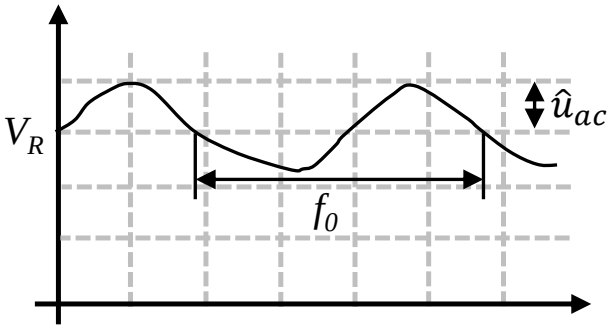

Fig. 4.5: Dielectric losses quantities graphical definition.
Source: Elaborated by the author

4.2.1 Relation between grid and d.c. bus active power oscillations

In steady state, the GSC instantaneous input active power (p_{in}) is only composed by a continuous value, since the primary source generates a direct voltage in a PV system or sinusoidal and balanced currents in a WEC system. In a similar way, under balanced voltages the GSC output power (p_{out}) is also constant, producing balanced and sinusoidal currents. Hence, neglecting the GSC losses, it can be assumed that the input and output power are equal and there is no energy flow to the d.c. bus capacitor. The power balance is represented in Fig. 4.6.

However, in an unbalanced fault, the instantaneous power p_{out} is formed by the sum of mean (P_{out}) and oscillatory ($\tilde{p}_{out}$) terms. As previously discussed, it can be used methods to reduce the generated power in PV and WEC systems. Thus, it is possible to assume that all

generated power is dissipated or delivered to the grid and the bus mean direct voltage is constant. Neglecting the converter losses, the energy balance in the d.c. bus is defined by:

$$\Delta p = p_{in} - p_{out} = p_{in} - (P_{out} + \tilde{p}_{out}) = -\tilde{p}_{out}. \tag{4.12}$$

The power set-points and reference currents handled by the power control strategies refer to the measurement point of voltage and currents, as shown in Fig. 4.6. Thus, the GSC output current is slightly different from the reference values generated by the power control strategies, since it has to supply the currents consumed by the LCL filter.

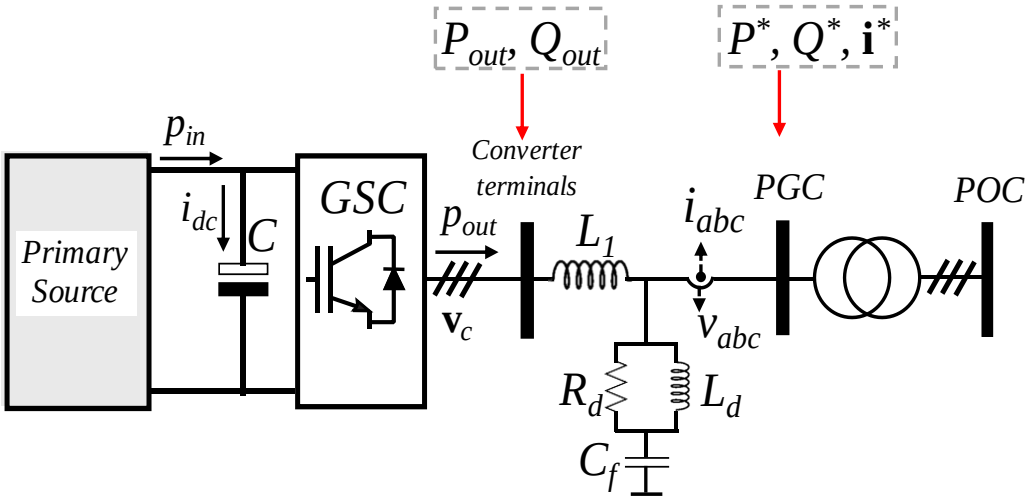

Fig. 4.6: Energy balance in GSC.
Source: Elaborated by the author

For sake of simplicity the current consumed by the LCL filter capacitive branch are ignored and the GSC terminals output power oscillation ($\tilde{p}_{out}$) can be approximated by:

$$\tilde{p}_{out} = \mathbf{v}_c^- \cdot \mathbf{i}_p^{+*} + \mathbf{v}_c^+ \cdot \mathbf{i}_p^{-*} + \mathbf{v}_c^- \cdot \mathbf{i}_q^{+*} + \mathbf{v}_c^+ \cdot \mathbf{i}_q^{-*}, \tag{4.13}$$

where $\mathbf{v}_c^{+-}$ are the positive and negative sequence voltages synthetized in the converter terminals (before the LCL filter as shown in Fig. 4.6). Then, to obtain a more generalized formulation, it is replaced the equations (3.52) and (3.53) of GFPC reference currents in (4.13), as follows:

$$\begin{aligned}\tilde{p}_{out} = \mathbf{v}_c^- \cdot \underbrace{\left(\frac{P^* k_p^+ \mathbf{v}^+}{k_p^+ |\mathbf{v}^+|^2 + k_p^- |\mathbf{v}^-|^2}\right)}_{i_p^+} + \mathbf{v}_c^+ \cdot \underbrace{\left(\frac{P^* k_p^- \mathbf{v}^-}{k_p^+ |\mathbf{v}^+|^2 + k_p^- |\mathbf{v}^-|^2}\right)}_{i_p^-} + \cdots \\ \mathbf{v}_c^- \cdot \underbrace{\left(\frac{Q^* k_q^- \mathbf{v}_\perp^-}{k_q^+ |\mathbf{v}^+|^2 + k_q^- |\mathbf{v}^-|^2}\right)}_{i_q^-} + \mathbf{v}_c^+ \cdot \underbrace{\left(\frac{Q^* k_q^+ \mathbf{v}_\perp^+}{k_q^+ |\mathbf{v}^+|^2 + k_q^- |\mathbf{v}^-|^2}\right)}_{i_q^+}.\end{aligned} \tag{4.14}$$

Grouping the similar terms:

$$\tilde{p}_{\text{out}} = \left(\frac{\left(k_p^+ \, \mathbf{v}^+ \cdot \, \mathbf{v}_c^- + k_p^- \, \mathbf{v}^- \cdot \, \mathbf{v}_c^+\right)}{k_p^+ \, |\mathbf{v}^+|^2 + k_p^- \, |\mathbf{v}^-|^2}\right) P^* + \left(\frac{\left(k_q^+ \, \mathbf{v}_\perp^+ \cdot \mathbf{v}_c^- - k_q^- \, \mathbf{v}_\perp^- \cdot \mathbf{v}_c^+\right)}{k_q^+ \, |\mathbf{v}^+|^2 + k_q^- \, |\mathbf{v}^-|^2}\right) Q^*. \tag{4.15}$$

Therefore, according (4.15), the power oscillation in the GSC terminals is a result from converter and measured point voltages interaction. This means that to compute the converter terminals power oscillation, it should be considered the dynamic of the LCL filter elements, which would require a very complex relation [56].

In order to obtain an analytical expression to describe the converter terminals and consequently the direct voltage bus power oscillation, it is assumed that the reference currents are function of the voltage $\mathbf{v}_c^{+-}$ (in fact they are function of the grid voltage). In addition, it is considered the mean values of the GSC terminals active P_{out} and reactive power Q_{out} (as can be seen in Fig. 4.6), instead the references P^* and Q^*, to contemplate the power consumed by the LCL filter during the voltage sag, which is different from normal operation condition. Thus, the (4.15) can be rewritten as follows.

$$\tilde{p}_{\text{out}} \approx \left(\frac{\left(k_p^+ + k_p^-\right) P_{out}}{k_p^+ \, |\mathbf{v}^+|^2 + k_p^- \, |\mathbf{v}^-|^2}\right) \mathbf{v}_c^+ \cdot \, \mathbf{v}_c^- + \left(\frac{\left(k_q^+ - k_q^-\right) Q_{out}}{k_p^+ \, |\mathbf{v}^+|^2 + k_p^- \, |\mathbf{v}^-|^2}\right) \mathbf{v}_{c\perp}^+ \cdot \mathbf{v}_c^-. \tag{4.16}$$

And the temporal form is defined by:

$$\begin{aligned} \tilde{p}_{\text{out}} = &\left(\frac{\left(k_p^+ + k_p^-\right)|\mathbf{v}_c^+||\mathbf{v}_c^-|\cos(2\omega t + \phi_c^+ - \phi_c^-)}{k_p^+ \, |\mathbf{v}_c^+|^2 + k_p^- \, |\mathbf{v}_c^-|^2}\right) P_{out} + \cdots \\ &\left(\frac{\left(k_q^+ - k_q^-\right)|\mathbf{v}_c^+||\mathbf{v}_c^-|\sin(2\omega t + \phi_c^+ - \phi_c^-)}{k_q^+ \, |\mathbf{v}_c^+|^2 + k_q^- \, |\mathbf{v}_c^-|^2}\right) Q_{out}, \end{aligned} \tag{4.17}$$

where ϕ_c^+ and ϕ_c^- are the positive and negative sequence phase angles of the converter voltages terminals. Likewise happen in the equations (4.6) and (4.7), the orthogonal relation between the terms in (4.17) can be obtained the power oscillation magnitude:

$$\|\tilde{p}_{out}\| = u_c \sqrt{\left(\frac{\left(k_p^+ + k_p^-\right)P_{out}}{k_p^+ \, + k_p^- \, u_c^2}\right)^2 + \left(\frac{\left(k_q^+ - k_q^-\right)Q_{out}}{k_q^+ \, + k_q^- \, u_c^2}\right)^2}, \tag{4.18}$$

where u_c is the GSC terminal voltages unbalance factor. The energy variation amplitude at the d.c. bus capacitor is decribed by [20]:

$$\Delta E = \max(\tilde{e}_{cap}), \tag{4.19}$$

where $\tilde{e}_{cap}$ is the instantaneous energy ripple that is a periodic time varying value, defined by:

$$\tilde{e}_{cap} = \int \Delta p \; dt = \int -\tilde{p}_{out} \; dt. \tag{4.20}$$

Then, replacing equation (4.17) in (4.20) and making the integral operation, the energy ripple is defined by:

$$\tilde{e}_{cap} = \cdots$$
$$\frac{u_c}{2\omega}\left\{-\left(\frac{\left(k_p^+ + k_p^-\right)\sin(2\omega t + \phi_c^+ - \phi_c^-)}{k_p^+ + k_p^- u_c^2}\right)P_{out} + \left(\frac{\left(k_q^+ - k_q^-\right)\cos(2\omega t + \phi_c^+ - \phi_c^-)}{k_q^+ + k_q^- u_u^2}\right)Q_{out}\right\}, \tag{4.21}$$

and the magnitude ΔE can be obtained by:

$$\Delta E = \cdots$$
$$\frac{u_c}{2\omega}\sqrt{\left(\frac{\left(k_p^+ + k_p^-\right)P_{out}}{k_p^+ + k_p^- u_c^2}\right)^2 + \left(\frac{\left(k_q^+ - k_q^-\right)Q_{out}}{k_q^+ + k_q^- u_u^2}\right)^2} = \frac{\|\tilde{p}_{out}\|}{2\omega}. \tag{4.22}$$

In other hand, the d.c. voltage can be approached in the following relation [20]:

$$v_{dc} \approx V_{dc} + \tilde{v}_{dc} = V_{dc} + \frac{1}{C\,V_{dc}}\int \Delta p\, dt = V_{dc} + \frac{\tilde{e}_{cap}}{C\,V_{dc}}, \tag{4.23}$$

where V_{dc} is the mean value of d.c. bus voltage, $\tilde{v}_{dc}$ is the instantaneous oscillation around the V_{dc}. Then, d.c. bus power oscillations amplitude Δv_{dc} is approximated through:

$$\Delta v_{dc} \approx \frac{\Delta E}{C\,V_{dc}} = \frac{\|\tilde{p}_{out}\|}{2\omega\,C\,V_{dc}}, \tag{4.24}$$

In equation (4.24) describe the factors that can be used in order to reduce the effects of voltage sag on the d.c. bus capacitor. Therefore, Δv_{dc} is:

- Directly proportional to the GSC terminals active power ripple magnitude $\|\tilde{p}_{out}\|$.
- Inversely proportional to the direct voltage level V_{dc}.
- Inversely proportional to the d.c. bus capacitance C.
- Inversely proportional to the grid frequency ω

Although (4.22) indicates that is possible to cancel the energy variation, and consequently the voltage ripple in (4.24) only using the APOC strategy, it is not a correct statement. The currents and voltages interaction with the LCL filter elements during the unbalanced voltage sags generate power oscillations, and as before discussed, to cancel them it should be considered the dynamic of the LCL filter in the power control strategies [56]. This is a complex task that is no addressed in this work.

Another consequence of the direct power oscillations is the low frequency current ripple in the bus capacitors, flowing with twice the fundamental frequency and as previously presented, it increases the thermal stress in the d.c. bus capacitors.

4.3 GSC power curtailment scheme

The GSC power curtailment algorithm presented in this section was adapted from the reference [27] and for this is used the GFPC strategy, allowing to contemplate other power control strategies. It has four control objectives listed according to their hierarchy and priority in the proposed control algorithm:

1) To meet the LVRT and RCI requirement defined in the actual GCs.
2) To limit the amount of injected current to the maximum allowed by the inverter.
3) Active power control in normal and under grid voltage sags.
4) Other power quality issues reduction, ancillary services.

The objective 4 listed above is different from the proposed in [27], where the focus was in the cancellation of the active power ripple. Thus, some modifications in the original algorithm are necessary, as described in the following subsection.

4.3.1 RCI requirement and current limitation

In order to achieve the objectives 1 and 2, it is necessary to introduce the currents notation of the GFPC strategy, as follow:

$$\mathbf{i}_p^* = \underbrace{I_p\ k_p^+}_{I_p^+}\frac{\mathbf{v}^+}{|\mathbf{v}^+|} + \underbrace{u\ I_p\ k_p^-}_{I_p^-}\frac{\mathbf{v}^-}{|\mathbf{v}^-|}, \tag{4.25}$$

$$\mathbf{i}_q^* = \underbrace{I_q\ k_q^+}_{I_q^+}\frac{\mathbf{v}_\perp^+}{|\mathbf{v}^+|} + \underbrace{u\ I_q\ k_q^-}_{I_q^-}\frac{\mathbf{v}_\perp^-}{|\mathbf{v}^-|}, \tag{4.26}$$

where:

$$I_p = \frac{P^*\,|\mathbf{v}^+|}{k_p^+|\mathbf{v}^+|^2 + k_p^-|\mathbf{v}^-|^2}, \tag{4.27}$$

$$I_q = \frac{Q^*\,|\mathbf{v}^+|}{k_q^+|\mathbf{v}^+|^2 + k_q^-|\mathbf{v}^-|^2}. \tag{4.28}$$

The positive sequence reactive current I_q^+ is defined by the GC RCI requirement and since the weight gain $k_q^+ = 1$ for all sinusoidal strategies discussed in this work, it can be assumed $I_q = I_q^+$ and $I_p = I_p^+$.

It is possible to note in (4.26) and (4.27) that each strategy generates different active and reactive current amplitude to feed-in the powers set points P^* and Q^*. The magnitude of positive sequence active current is calculated by:

$$I_p^+ = \frac{2}{3} P^* \frac{|\mathbf{v}^+|}{k_p^+ |\mathbf{v}^+|^2 + k_p^- |\mathbf{v}^-|^2}, \tag{4.29}$$

Based in reference [27] mathematical development, the maximum current amplitude ($I_{máx}$) can be approximated through:

$$I_{max} \approx \sqrt{\frac{|\mathbf{v}^+|^2 - 2|\mathbf{v}^+||\mathbf{v}^-|\, x + |\mathbf{v}^-|^2}{|\mathbf{v}^+|^2} \left(\left(I_p^+\right)^2 + \left(I_q^+\right)^2 \right)}, \tag{4.30}$$

where:

$$x = \min \left\{ \cos(\phi), \cos\left(\phi - \frac{2\pi}{3}\right), \cos\left(\phi + \frac{2\pi}{3}\right) \right\}, \tag{4.31}$$

$$\cos(\phi) = \frac{v_\alpha^+ \, v_\alpha^- - v_\beta^+ \, v_\beta^-}{V^+ \, V^-}. \tag{4.32}$$

The I_{max} limits the I_p^+ current, since I_q^+ is defined by the GCs according to the following relation:

$$I_{q(GC)}^+ = \begin{cases} I_{q(GC)-max} & \text{if } 0.0 \le V^+ \le 0.05 \text{ pu} \\ -k_{i1} \, V^+ + k_{i2} & \text{if } 0.5 < V^+ < V_{\min}^+ \text{ pu} \\ 0.0 & \text{if } V_{\min}^+ < V^+ < 1.1 \text{ pu} \end{cases}, \tag{4.33}$$

where $I_{q(GC)-max}$ is the maximum required reactive current ($I_{q(GC)-max} = 1(\text{pu})$ in [9–11] and $I_{q(GC)-max} = 0.9(pu)$ in [12]), k_{i1}, k_{i2} are the linear coefficients from the RCI equation and $V_{\min}^+$ is the minimum residual voltage to the energy conversion system beginning the RCI requirement ($V_{\min}^+ = 0.85(\text{pu})$ for [9,12] and $V_{\min}^+ = 0.9(\text{pu})$ for [10,11]), as can be seen in Fig. 1.3. The maximum positive sequence current can be calculated by:

$$I_{p-max}^+ = \sqrt{\frac{|\mathbf{v}^+|^2 (I_{rated})^2}{|\mathbf{v}^+|^2 - 2|\mathbf{v}^+||\mathbf{v}^-|\, x + |\mathbf{v}^-|^2 \, |\mathbf{v}^+|^2} - \left(I_q^+\right)^2}, \tag{4.34}$$

I_{rated} is the converter rated current (where $I_{rated} \ge I_{max}$), and the active current must be limited to its maximum allowable amplitude, i.e., $I_p^+ \le I_{p-max}^+$.

According to the grid code [12], the RCI curve in Fig. 1.3 defines the minimum current value to be injected to the grid during the LVRT operation, moreover the converter must support the grid with its maximum current capacity. In a low active power production condition, the reactive current must be recalculated in order to fulfill the GC requirements, as follow:

$$I_q^+ = \sqrt{\frac{|\mathbf{v}^+|^2 (I_{rated})^2}{|\mathbf{v}^+|^2 - 2|\mathbf{v}^+||\mathbf{v}^-|\, x + |\mathbf{v}^-|^2\, |\mathbf{v}^+|^2} - \left(I_p^+\right)^2}, \tag{4.35}$$

Once defined the currents magnitudes, assuming $k_p^+ = 1$, the time varying references are calculated by:

$$\mathbf{i}_p^* = I_p^+ \frac{\mathbf{v}^+}{|\mathbf{v}^+|} + k_p^- \, u \, I_p^+ \frac{\mathbf{v}^-}{|\mathbf{v}^+|}, \tag{4.36}$$

$$\mathbf{i}_q^* = I_q^+ \frac{\mathbf{v}_\perp^+}{|\mathbf{v}^+|} + k_q^- \, u \, I_q^+ \frac{\mathbf{v}_\perp^-}{|\mathbf{v}^-|}, \tag{4.37}$$

The GSC power curtailment scheme flowchart is presented in Fig. 4.7. The algorithm input are the reference power from the d.c. bus voltage controller P^*, the positive and negative sequence voltages $\mathbf{v}^+$, $\mathbf{v}^-$, $\mathbf{v}_\perp^+$, $\mathbf{v}_\perp^-$, their amplitude $|\mathbf{v}^+|, |\mathbf{v}^-|$ and the phase angle ϕ.

If there is no sag, the algorithm conducts to the left side of the flowchart, to the cases 1 or 2, where there is no reactive current injection ($I_q^+ = 0$). The equation (4.34) is used in order to ensure that I_{max} is not exceeded and only if $I_p^+ > I_{p-max}^+$ the GSC active power curtailment is performed in case 2.

Under fault operation, I_q^+ is obtained from the GC ($I_q^+ = I_{q(GC)}^+$) and the I_{p-max}^+ is calculated through (4.34). In case 3, the current I_p^+ does not exceed the limit I_{p-max}^+, and I_q^+ is recalculated using (4.35). The active power curtailment is realized in case 4, where I_p^+ is saturated in I_{p-max}^+.

The operation in cases 5 and 6, the inverter only injects relative current, i.e., it had been executed a total active power curtailment to avoid the converter operation above its rated current. In case 6 all the converter capacity is use to inject reactive current through the positive sequence and $I_p^- = I_q^- = 0$.

Once it is defined the magnitudes I_p^+, I_q^+, I_p^- and I_q^- the reference currents are calculated using the equations (4.36) and (4.37).

For the BPSC strategy, the equations can be simplified by making $V^- = 0$, $I_p^- = I_q^- = 0$ and $k_p^- = k_q^- = 0$ in the power curtailment algorithm equations.

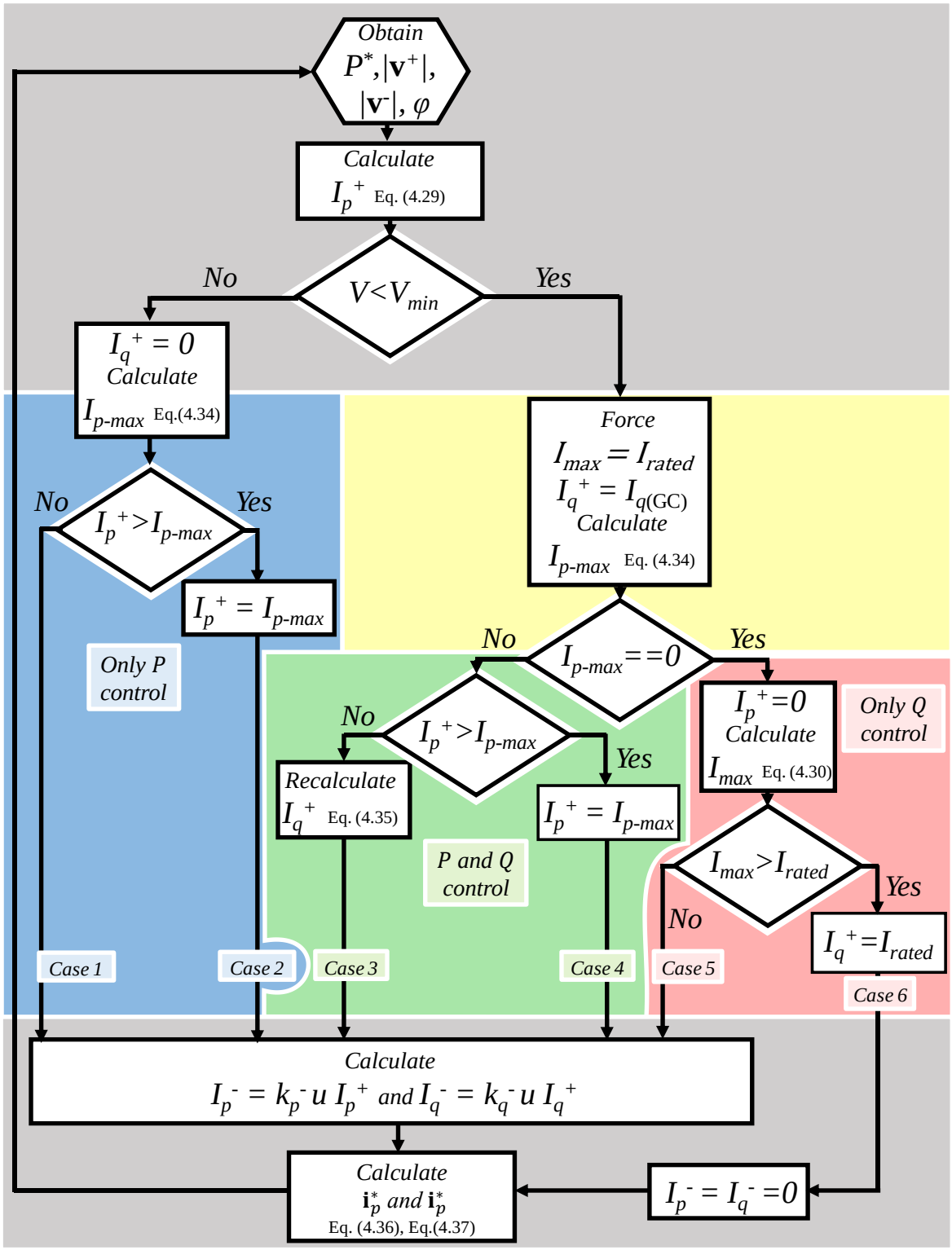

Fig. 4.7: Flowchart of the GSC power curtailment algorithm
Source: Adapted from [27]

4.4 Case study

To evaluate the discussion in relation to the power control strategies behavior and reduction of the effects on the power electronic converter during the LVRT operation, simulations of a real scale wind energy conversion system are performed using the Matlab/Simulink software. The WEC system parameters are described in Table V and since the focus is on the electronic converter, the following conditions are imposed:

- The POC voltage cannot be altered by the generating unit, i.e., stiff grid (Focus on the power electronic converter).
- The system operates with rated power before the fault occurrence (worst condition) and return to this condition after the fault clearance.
- The chopper resistance can dissipate the WEC rated power during the whole voltage ride though operation.
- All the graphs are in per unit in relation to the rated values of voltage, current, power, etc.

In this case study the APOC, RPOC, AARC, PNSC and BPSC will be compared in terms of the current profiles and power oscillations as well as their impact to the grid converter.

Table V: Power Converter Parameters

Parameter	**Symbol**	**Value**	**Unity**
Line nominal voltage (PGC)	V_n	0.69	kV_{rms}
Converter nominal current	I_n	1.76	kA_{rms}
Grid frequency	f_n	60	Hz
Switching frequency	f_{sw}	3.42	kHz
Chopper switching frequency	$f_{sw(ch)}$	3.42	kHz
Bus capacitor	C_{dc}	35.7	mF
d.c. bus nominal voltage	V_{dc}	1.15	kV
d.c. bus shutdown voltage	$V_{dc\text{-}st}$	1.2	kV
Filter Inductor 1	L_1	80	µH
Filter Inductor 2	L_2	25.26	µH
Filter capacitor	C_f	147	µF
Damping Resistor	R_d	0.1	Ω
Damping Inductor	L_d	20	µH
Rated Power	P_{gen}	2	MW

It is used the droop curve based on the Brazilian grid code [9] showed in Fig. 1.3, where the linear coefficients in the (4.33) are k_{i1} =2.8571, k_{i2} = 2.4286, the maximum reactive current is $I_{q(GC)-max}$ = 1.0(pu), and the minimum positive sequence residual voltage is $V_{\min}^{+} = 0.85$(pu).

4.4.1 Specific case analysis

Initially, the control strategies are evaluated for a specific voltage sag, where the grid PCC voltages are described by v_a = 1(pu), v_b = v_c = 0.4(pu) resulting in a positive sequence voltage $|\mathbf{v}^+| = 0.6$(pu) and an unbalanced factor u = 1/3. The simulated PCC phase voltages are shown in Fig. 4.8.

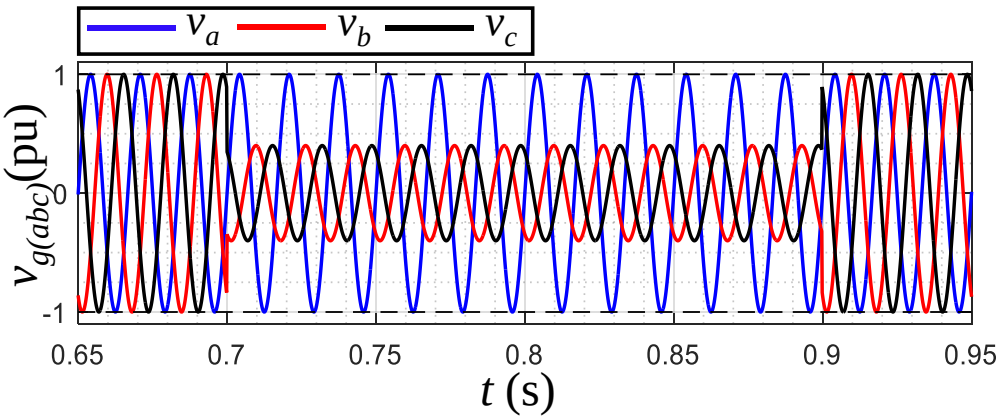

Fig. 4.8: Point of common coupling phase voltages.
Source: Elaborated by the author

Fig. 4.9 to Fig. 4.13 present the GSC currents in natural and stationary frames and the active and reactive power oscillations in the PGC (black lines) and at the converter terminals (blue lines) for the APOC, RPOC, AARC, PNSC and BPSC, respectively. Except by the BPSC all of others strategies generate unbalanced currents, which results in vectors with elliptical paths in the complex plane.

In the APOC currents profiles in Fig. 4.9(a), the smaller phase voltages amplitudes have the highest currents magnitude and vice-versa. This behavior in the stationary frame (Fig. 4.9(b)) reflects in the both active $\mathbf{i}_p$ and reactive $\mathbf{i}_q$ current have their maximum values in quadrature with the voltage vector peak value $\mathbf{v}$. Consequently, it is observed null active power oscillations (Fig. 4.9(c)) and high reactive power ripple (Fig. 4.9(d)) in the PGC. However, the active power oscillation at the converters terminals is not null, which is a result from the interaction with LCL filter elements.

The RPOC has an opposite behavior in relation to the APOC, since the highest voltage and currents magnitudes happens in the same phase, as presented in Fig. 4.10(a). Hence, in the stationary frame (Fig. 4.10(b)) the active $\mathbf{i}_p$ and reactive $\mathbf{i}_q$ currents have their maximum values aligned with the voltage vector $\mathbf{v}$ peak, that is, in quadrature to the orthogonal projection $\mathbf{v}_\perp$. Resulting in high active power ripple (Fig. 4.10(c)) and null reactive power oscillations (Fig. 4.10(d)).

Although the reactive power at the converter terminals (q_{out}) presents low oscillations, its offset in relation to the PGC reactive power (q) becomes more evident, which is related to the reactive power demanded by the LCL filter during the voltage ride through operation that should be supplied by the GSC.

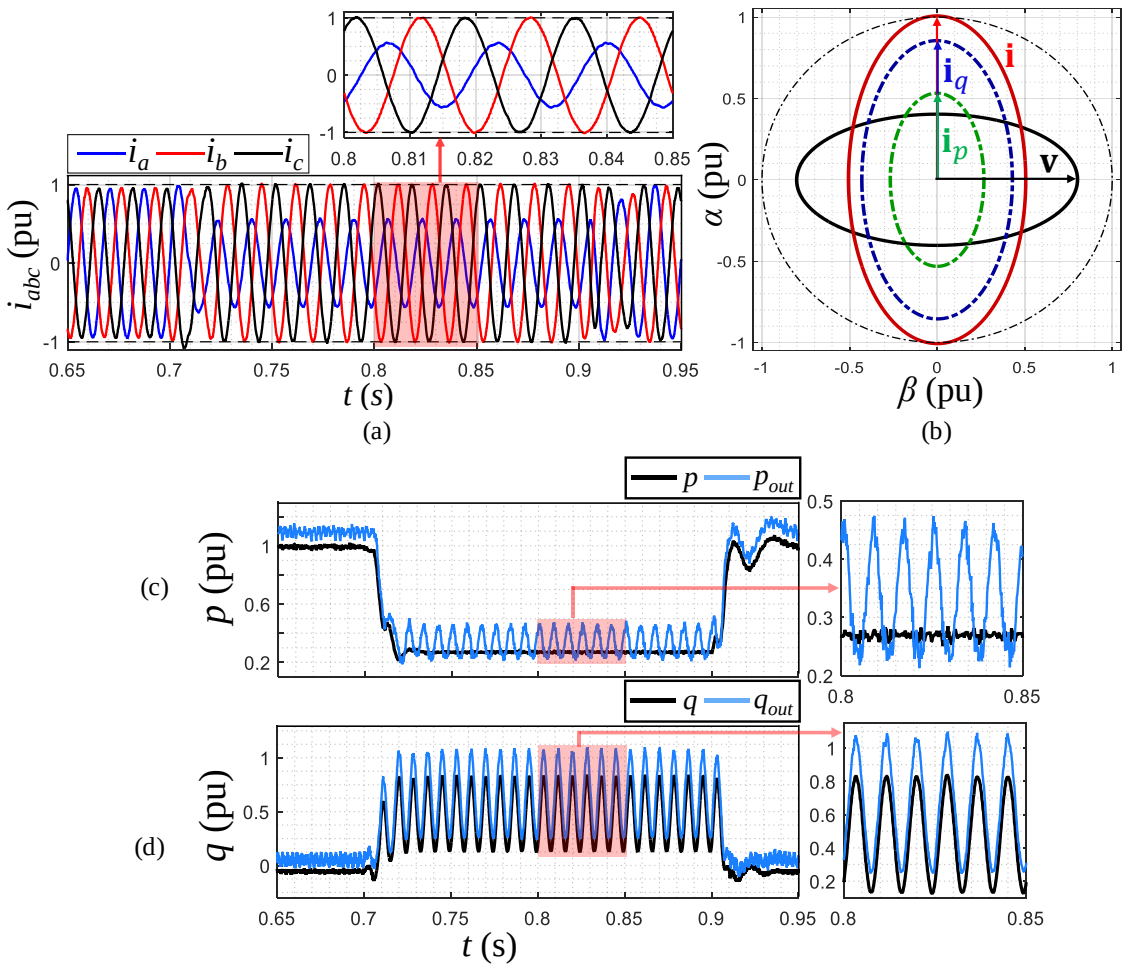

Fig. 4.9: APOC strategy GSC currents (a) in natural frame and (b) stationary frame, (c) active and (b) reactive instantaneous power in the PGC (black line) and in the converter terminals (blue line).
Source: Elaborated by the author

The currents vector path in Fig. 4.9(b) and Fig. 4.10(b) demonstrate that for the sinusoidal strategies, the voltage and current vectors must have their maximum magnitude values in quadrature in order to cancel the power oscillation. In Fig. 4.9(b) for example, in the minimum value of **v** and maximum of $\mathbf{v}_{\perp}$ the vector **i** present its highest magnitude value, which results in null active power oscillations and high values of reactive power ripple.

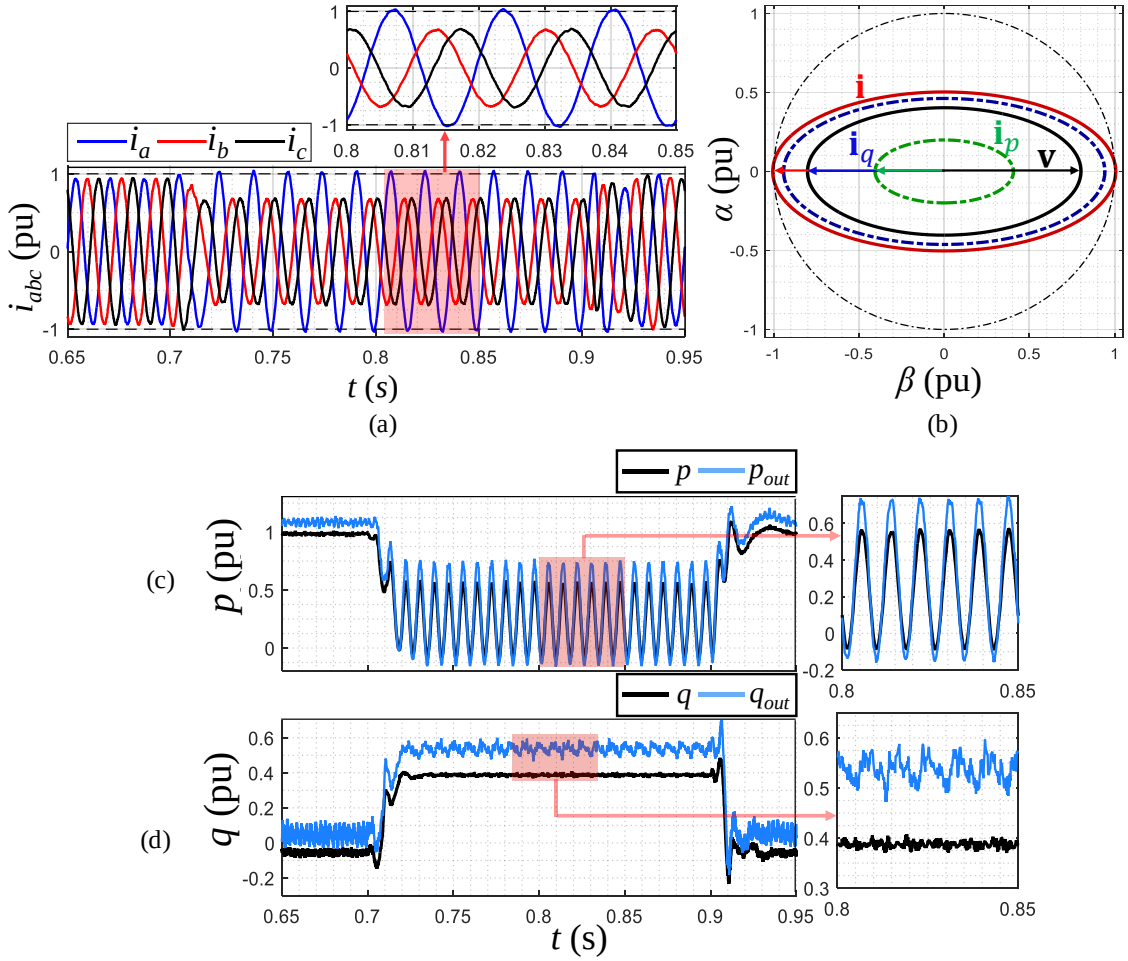

Fig. 4.10: RPOC strategy GSC currents (a) in natural frame and (b) stationary frame, (c) active and (b) reactive instantaneous power in the PGC (black line) and in the converter terminals (blue line)..
Source: Elaborated by the author

The AARC generates unbalanced currents as presented in Fig. 4.12(a). The active current $\mathbf{i}_p$ is directly proportional to $\mathbf{v}$ and the reactive $\mathbf{i}_q$ to the orthogonal voltage $\mathbf{v}_\perp$, which becomes more evident in Fig. 4.11(b), where the vector $\mathbf{v}$ is aligned to $\mathbf{i}_p$ and in quadrature to $\mathbf{i}_q$. Therefore, as previously discussed and stated in Table IV, the active power oscillations only depend on P^* and the reactive power ripple only depends on Q^*. Since for the case under analyses $I_q \geq I_p$ for the AARC, the active power fluctuation is lower than the reactive power ripple, as can be observed in Fig. 4.11(c) and Fig. 4.11(d).

The PNSC also generates unbalanced currents as shown in Fig. 4.12(a). However, differently from the AARC, the PNSC conductance and susceptance are not constant and thus, the peak of the vector $\mathbf{v}$ is in quadrature to the current $\mathbf{i}_p$ and aligned to $\mathbf{i}_q$ in the complex plane Fig. 4.12(b).

Therefore, according to previous discussions and to the equations in Table IV, the active current generates reactive power oscillations and reactive current generates active power ripple and consequently, if the active current is null there is no reactive power oscillations, in other hands, if the reactive current is null there is no active power oscillations. Since for the case under analyses $I_q \geq I_p$ for the PNSC, the active power fluctuation is higher than the reactive power ripple, as can be observed in Fig. 4.12(c) and Fig. 4.12(d)

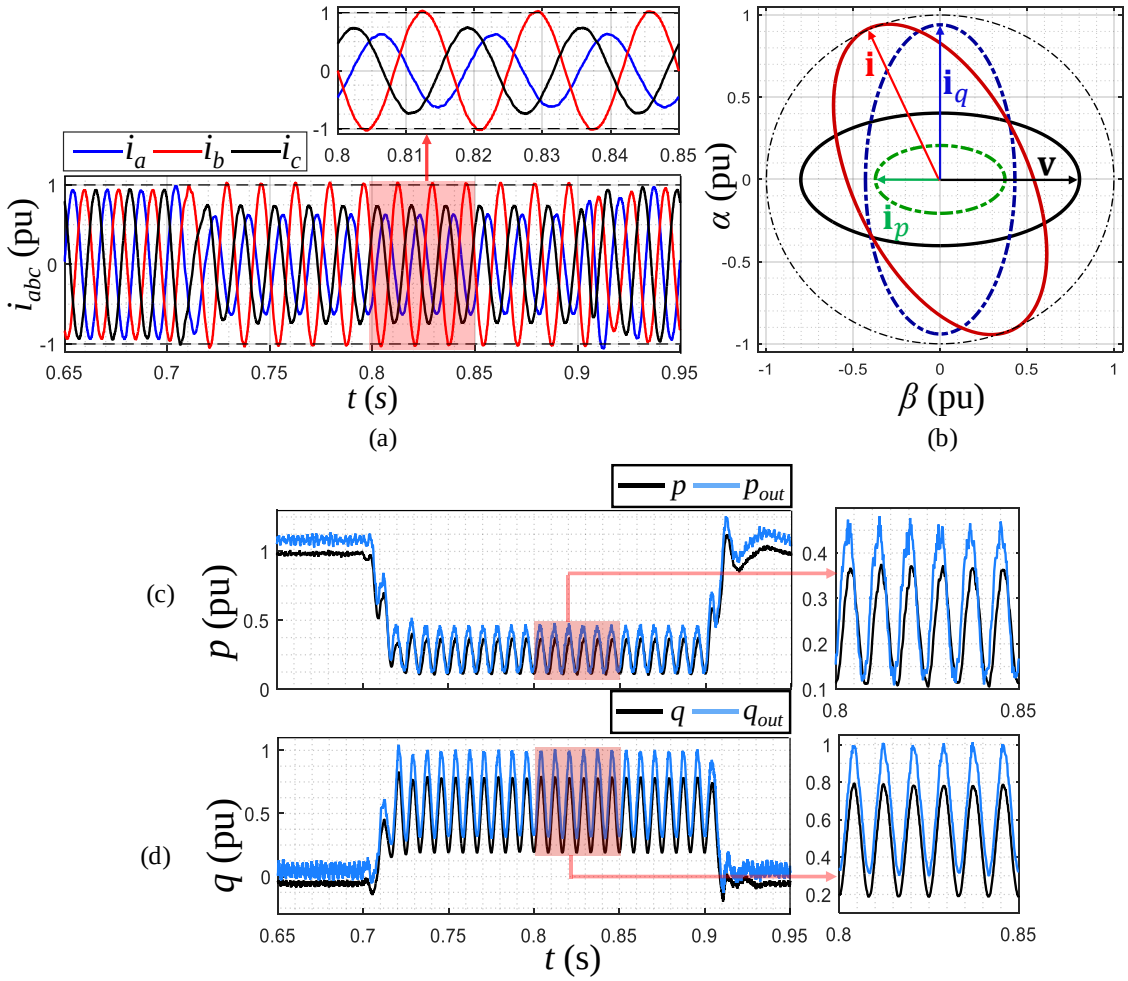

Fig. 4.11: AARC strategy GSC currents (a) in natural frame and (b) stationary frame, (c) active and (b) reactive instantaneous power in the PGC (black line) and in the converter terminals (blue line)..
Source: Elaborated by the author

.

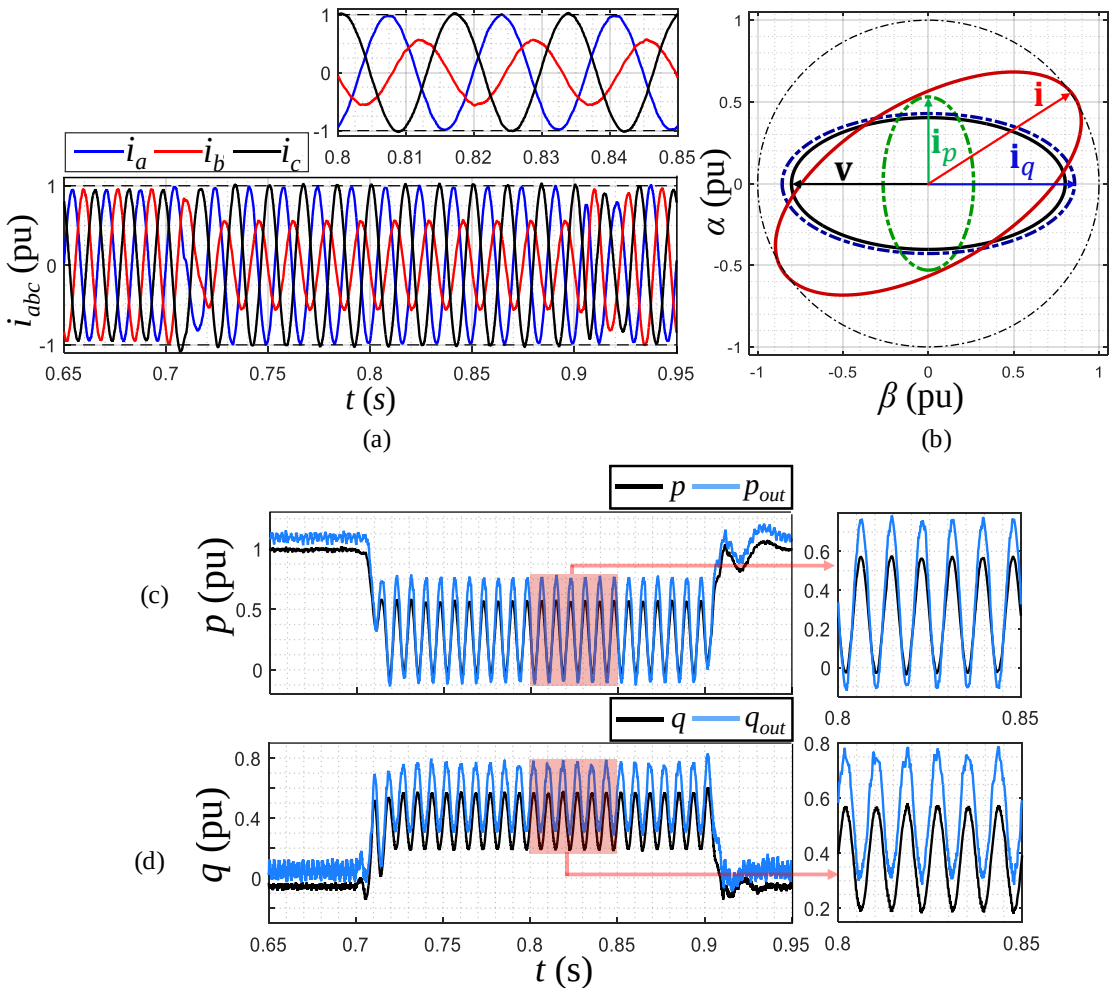

Fig. 4.12: PNSC strategy GSC currents (a) in natural frame and (b) stationary frame, (c) active and (b) reactive instantaneous power in the PGC (black line) and in the converter terminals (blue line)..
Source: Elaborated by the author

The BPSC takes into account only the positive sequence voltage for the reference calculation, generating balanced and sinusoidal currents as shown in Fig. 4.13(a), exactly as required by the actual GCs. Thus, the active and reactive currents vectors paths have a circular shape in the stationary frame (Fig. 4.13(b)). Furthermore, specifically for the case under analysis, the BPSC currents magnitudes are equal, that is, $I_q = I_p$.

The unbalanced voltages and balanced currents interactions result in oscillations in active and reactive power, as shown in Fig. 4.13(c) and Fig. 4.13(d). Demonstrating that if the reactive current is injected exactly as demanded by the GCs, i.e., without any negative sequence compensation, the active and reactive power present power oscillations.

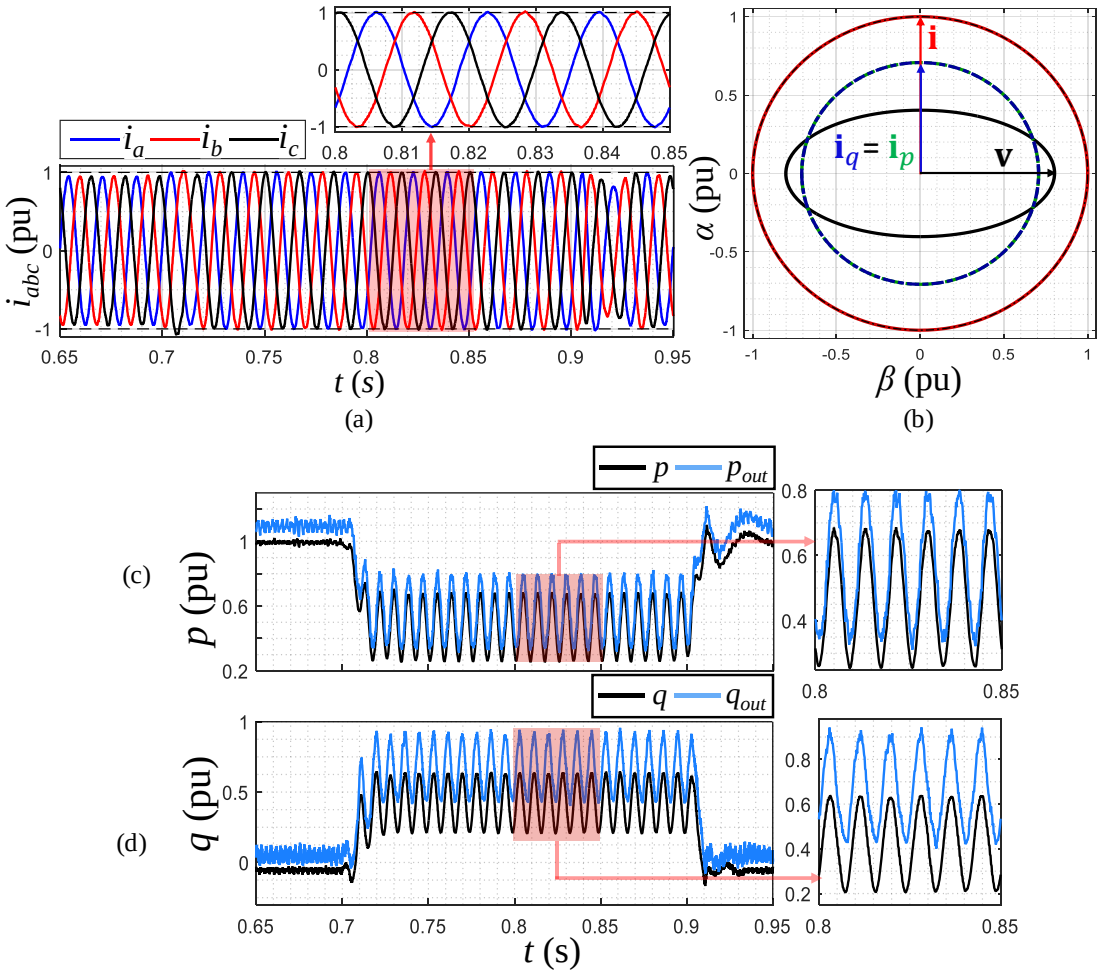

Fig. 4.13: BPSC strategy GSC currents (a) in natural frame and (b) stationary frame, (c) active and (b) reactive instantaneous power in the PGC (black line) and in the converter terminals (blue line).
Source: Elaborated by the author

Fig. 4.14 to Fig. 4.18 show a comparison between the oscillating terms of the instantaneous powers (black lines), and their magnitude (red line) calculated through the equations in the Table IV.

The calculated values are very accurate when compared to the simulated curves in voltage sag steady state, supporting the previous analyzes. Despite the APOC (Fig. 4.14) cancel the active power oscillation, it presents the highest values of reactive power ripple among the analyzed strategies. The opposite is true for the RPOC (Fig. 4.15), where besides null reactive power oscillations, it presents the highest active power ripple.

The AARC (Fig. 4.16) and PNSC (Fig. 4.17) may alternate with respect to which has the highest oscillation amplitude, since as described in Table IV, their power ripple magnitude depends on the operation point. However, it is worth emphasizing that, the powers oscillations in the PNSC are more susceptible to the phase voltages unbalance than the AARC.

The active and reactive power oscillations present the same magnitude value in the BPSC (Fig. 4.18) where they are proportional to the total power and to the unbalance between the phases, as described by BPSC equations in the Table IV.

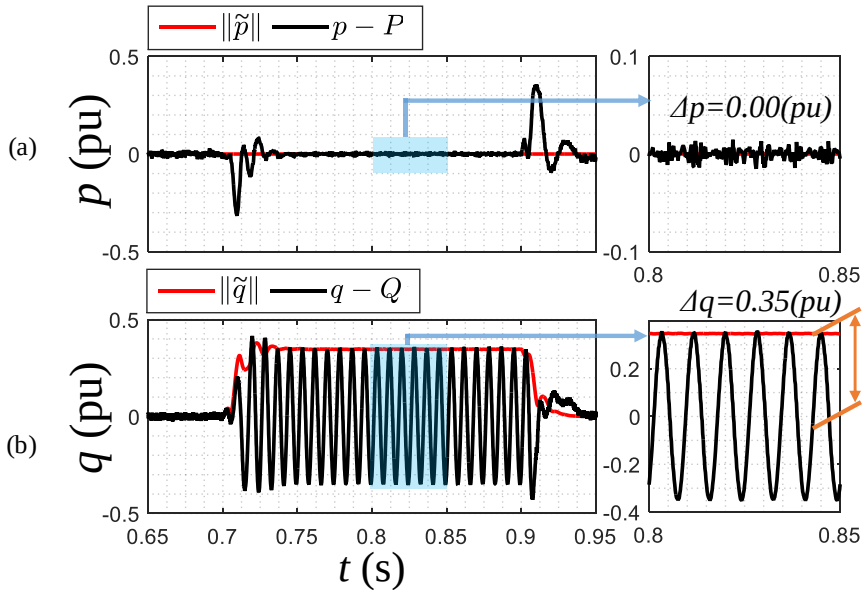

Fig. 4.14: Comparison between simulated (black line) and calculated (red line) (a) active and (b) reactive power oscillation magnitude from APOC.
Source: Elaborated by the author

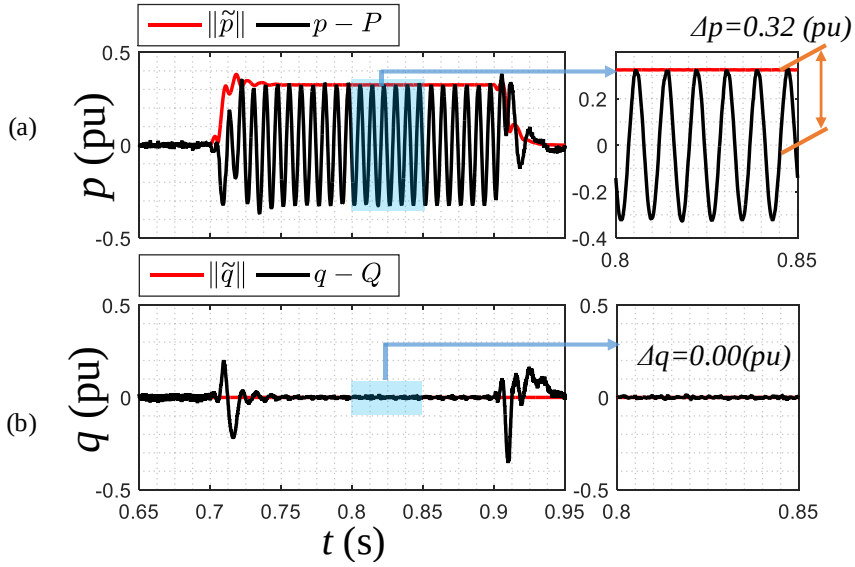

Fig. 4.15: Comparison between simulated (black line) and calculated (red line) (a) active and (b) reactive power oscillation magnitude from RPOC.
Source: Elaborated by the author

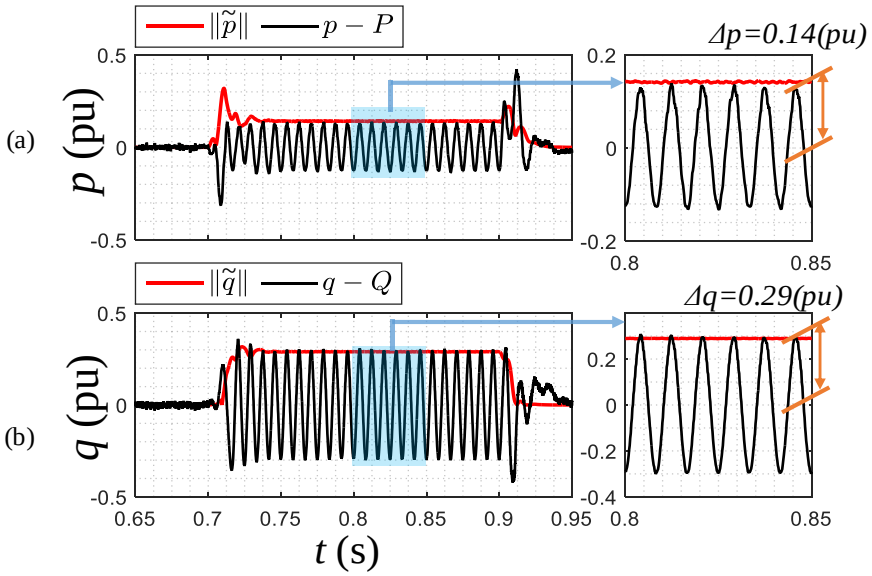

Fig. 4.16: Comparison between simulated (black line) and calculated (red line) (a) active and (b) reactive power oscillation magnitude from AARC.
Source: Elaborated by the author

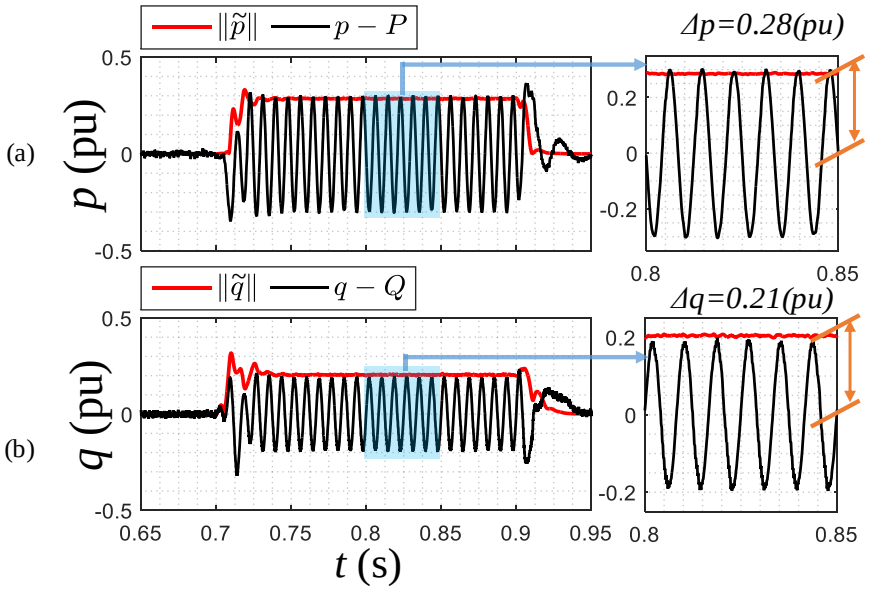

Fig. 4.17: Comparison between simulated (black line) and calculated (red line) (a) active and (b) reactive power oscillation magnitude from PNSC.
Source: Elaborated by the author

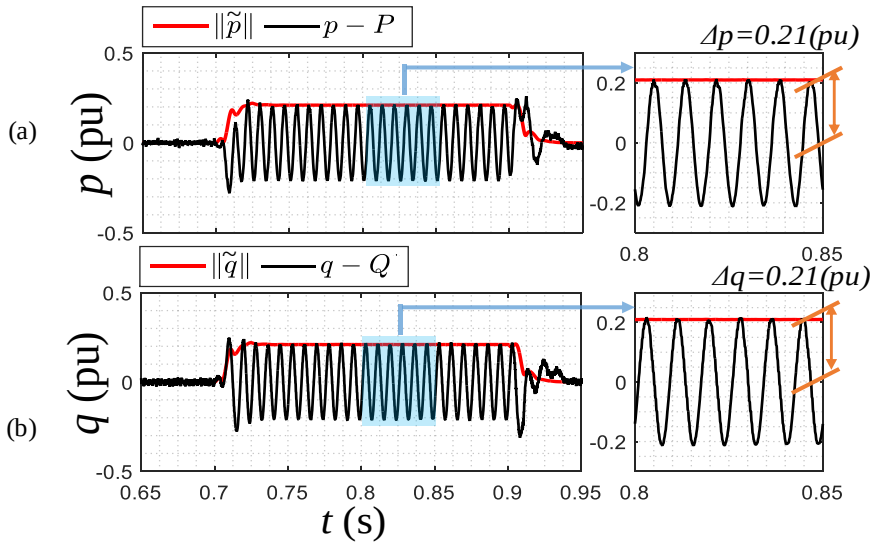

Fig. 4.18: Comparison between simulated (black line) and calculated (red line) (a) active and (b) reactive power oscillation magnitude from BPSC.
Source: Elaborated by the author

Fig. 4.19 and Fig. 4.20 show the direct voltage ripple and the bus capacitors current frequency spectrum during the voltage sag operation for different power control strategies. It is presented a comparison between the simulated d.c. voltage (black line) and its magnitude (red line) calculated through the equation (4.24), where the calculated values are close with to the simulated curves in voltage sag steady state, except by the APOC.

As expected, the direct voltage ripple in Fig. 4.19 increases proportionally with the active power oscillation. However, the ripple amplitude is small in relation to the direct voltage nominal value. For the APOC, since the active power is not null at the converter terminals, as shown in Fig. 4.19(a), the direct voltage ripple is also different from zero.

Regarding the d.c. bus capacitor current spectrum in Fig. 4.20, two components raise up during the voltage sag. The first frequency is located at 120(Hz) and as well as the voltage ripple, this current component is proportional to active power oscillation, were the highest current ripple among the analyzed strategies is about 29(%) of the converter rated current for the RPOC.

The second component is located at the protection chopper switching frequency 3.42(kHz) and its side bands, where it is related to the unbalanced between the generated and grid feed-in active power. It is worth to note that, as discussed in the section 2.3, in PV systems the generated power is modified only by change the array voltage. Consequently, the chopper frequency component does not exist in the photovoltaic converters bus capacitors current spectrum.

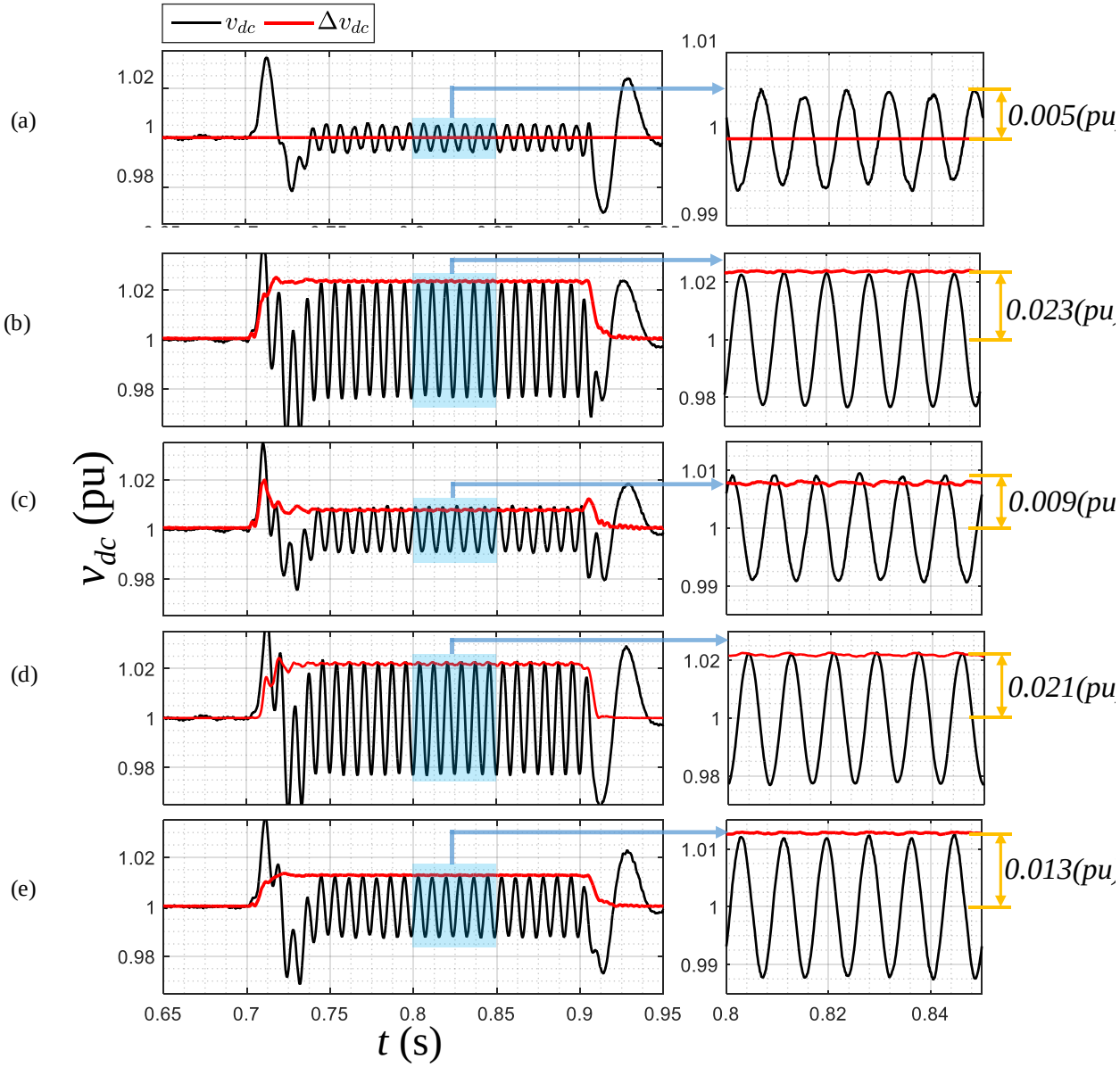

Fig. 4.19: Bus direct voltage oscillation for (a) APOC, (b) RPOC, (c) AARC, (d) PNSC and (e) BPSC.
Source: Elaborated by the author

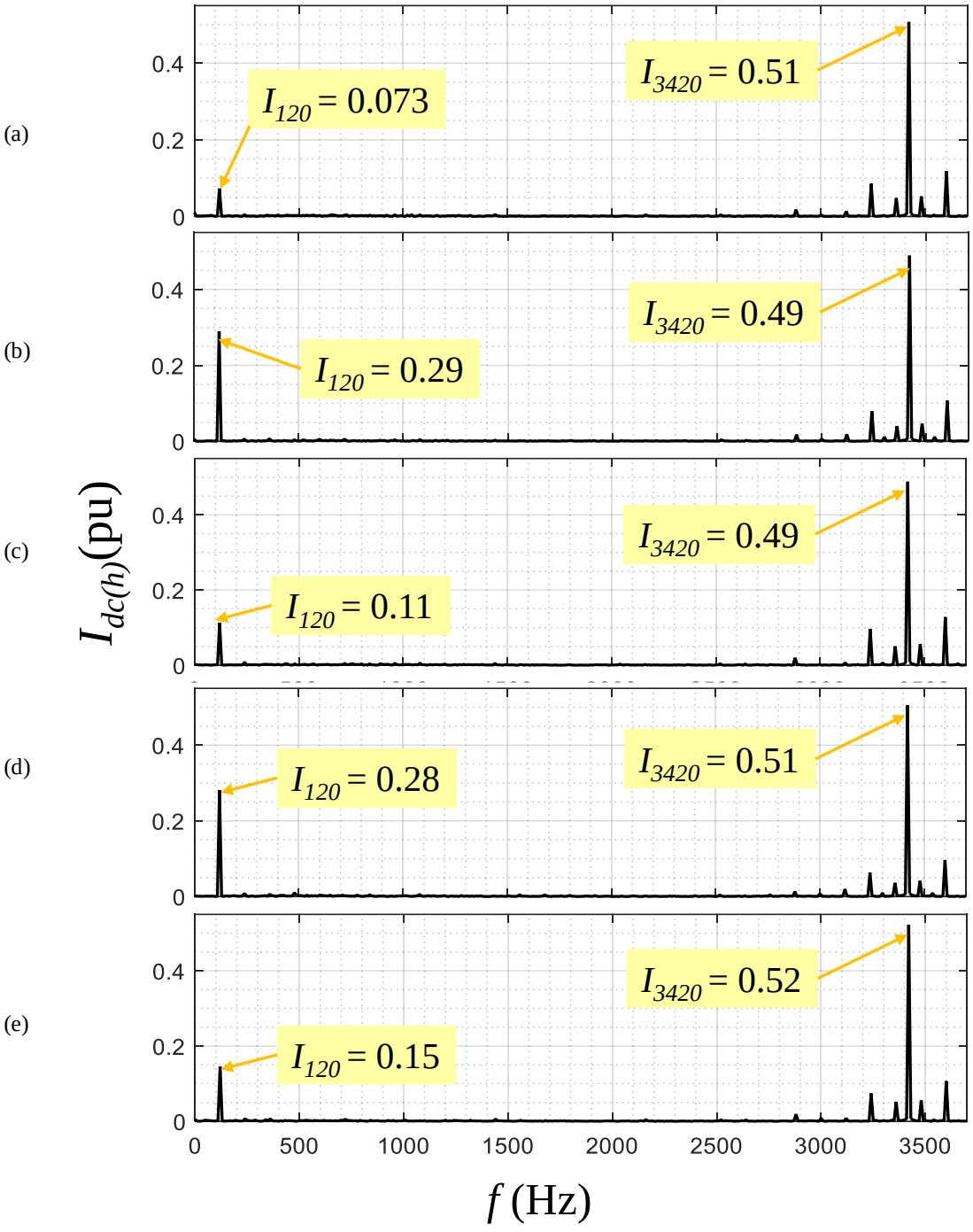

Fig. 4.20: Bus capacitors direct current frequency spectrum for (a) APOC, (b) RPOC, (c) AARC, (d) PNSC and (e) BPSC.
Source: Elaborated by the author

4.4.2 Generalized analysis

To extend the results to different points of RCI curve requirement in Fig. 1.3, several simulations were carried out, keeping v_a = 1(pu), while v_b and v_c were decreased for each simulation interaction, as exemplified in the Fig. 4.21. The voltage limits for the GU disconnection established in grid codes were disregarded for this analysis.

Fig. 4.22 shows the positive sequence reference currents generated by the power curtailment algorithm, as a function of the unbalanced factor u. Based on it, the results analysis is divided into two sections.

- Section I: it is possible to meet the grid code, providing active power and negative sequence currents.
- Section II: the active current becomes null and whole converter capacity should be used to delivering reactive current to the grid.

It is verified that the active current provided by the BPSC is always higher than the other strategies for the same value of u since there is no negative sequence no power injection, and the RPOC and AARC have the lowest level. This affirmation can be proved by the equation (4.27) replacing the values of k_p^+ and k_p^- of Table II. For strategies such RPOC and AARC, there is an addition of the square positive and negative voltages magnitudes in equation (4.27), thus, a lower active current value is required to produce the active power P^* in comparison to the APOC and PNSC, where there is a subtraction in equation (4.27).

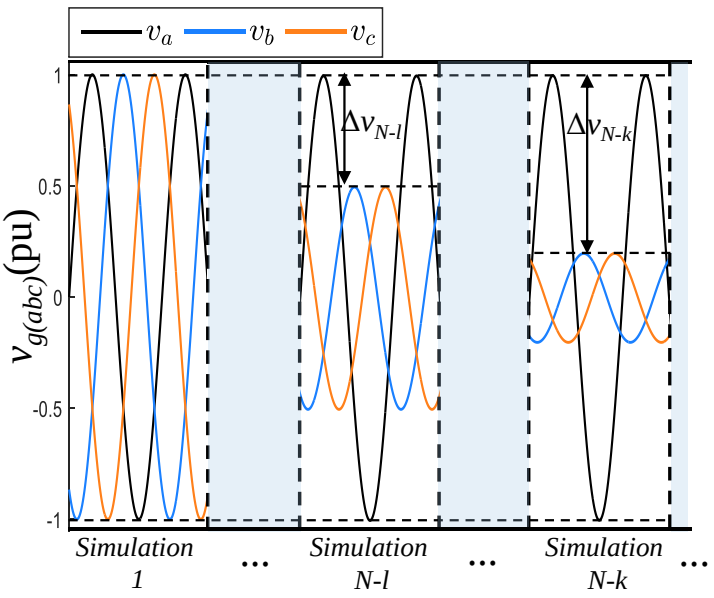

Fig. 4.21: Voltage variation for generalized analysis
Source: Elaborated by the author

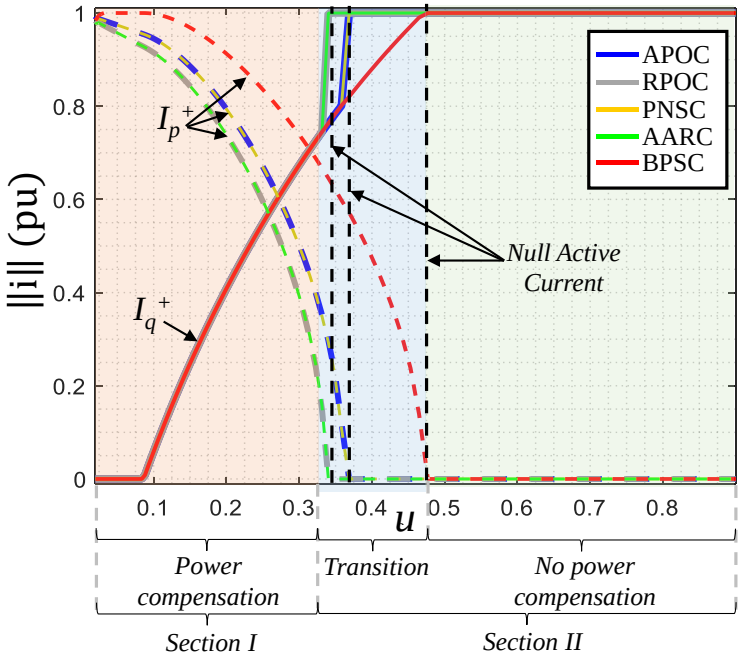

Fig. 4.22: Positive sequence reference currents magnitude
Source: Elaborated by the author

As described by equation (4.26), I_q^- is related to I_q^+ through the unbalance factor u. Thus, in the region of zero active current, due to the high value of I_q^+ and u, the converter would not be able to inject negative sequence currents without its capacity being exceeded. However, the remaining I_q value not provide the converter maximum current capacity during the LVRT, in accordance with GC [12]. Therefore, the power curtailment algorithm increases the I_q^+ to achieve this objective, explaining the sudden current value in the transition region.

Fig. 4.23 presents a comparison between the power oscillation magnitudes simulated (square markers) and calculated (continuous line) through the equations in the Table IV. The APOC and RPOC have complementary characteristics, in the same way, AARC and PNSC where the reduction of active power oscillation increases the reactive power ripple and vice-versa. Moreover, the BPSC strategy tends to be a compromise between all of them, where the active and reactive present similar power ripple magnitude.

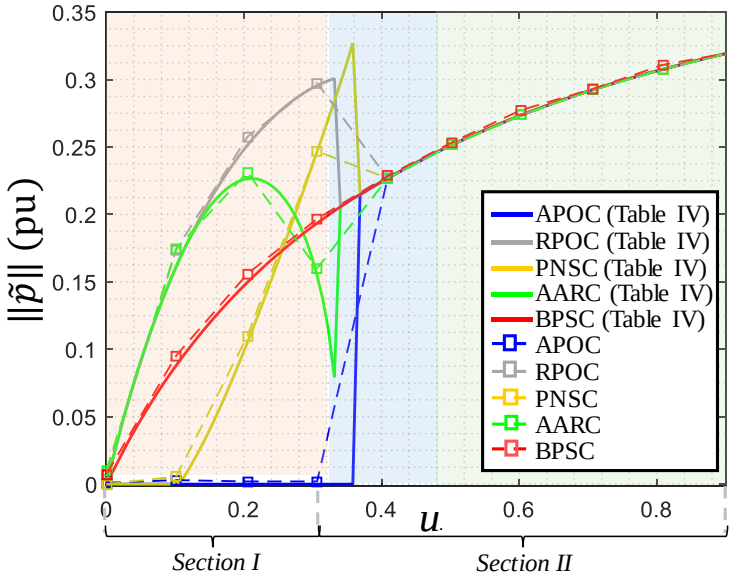

(a)

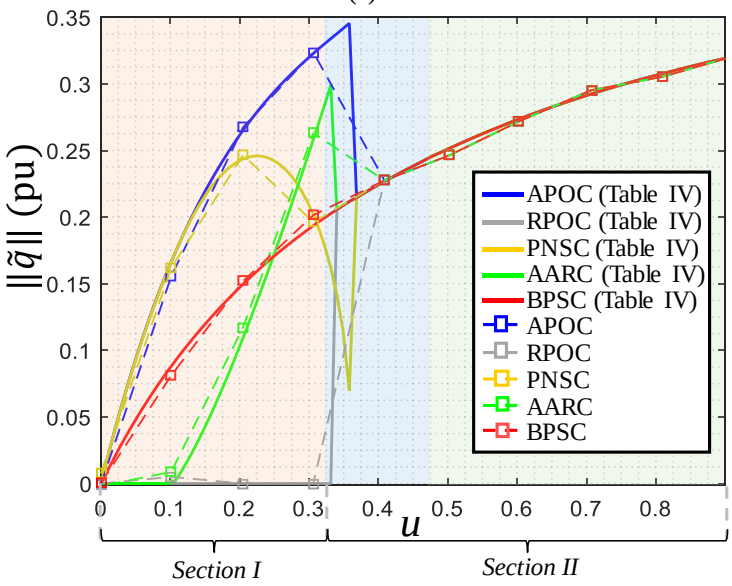

(b)

Fig. 4.23: (a) Active and (b) Reactive simulated and calculated power oscillation magnitude
Source: Elaborated by the author

The simulated (square markers) and calculated (continuous lines) values through equation (4.24) of the dc bus voltage ripple can be seen in the Fig. 4.24, where the the values are well approximated except for the APOC strategy, since the power ripple in the converter terminals is not null. In addition, the errors increase with the unbalanced factor, but the curves tendencies are similar. Comparing the results in Fig. 4.24 and Fig. 4.23(a) is possible to see the proportional relation between the active power oscillation and d.c. bus voltage ripple.

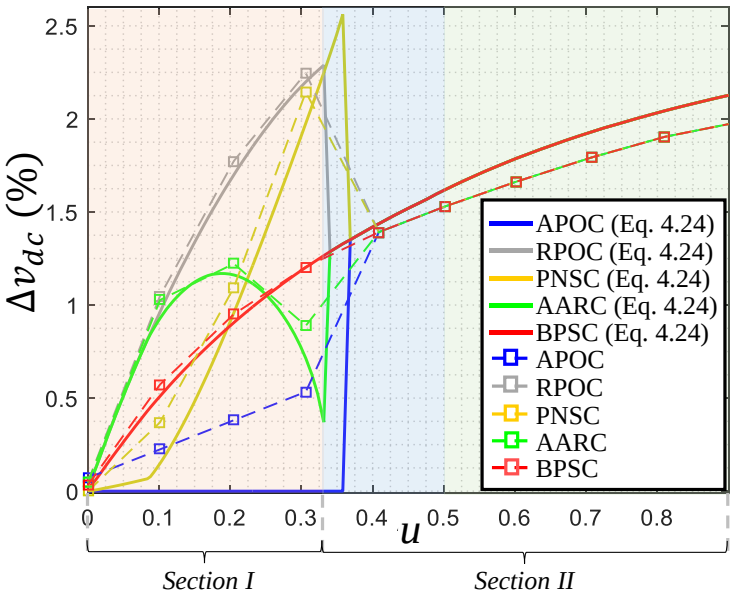

Fig. 4.24: simulated and calculated direct voltage oscillation
Source: Elaborated by the author

4.5 Chapter Conclusion

The aim of this chapter was discussing the effects of power oscillations, generated by the previously presented power control strategies, on the grid-connected converters. For this, equations that quantify the steady-state power oscillation magnitude for the sinusoidal strategies and equations that relate the active power oscillation and d.c. bus voltage ripple were proposed.

In the results obtained from the 2(MW) WEC study case, some observations can be done:

- The proposed magnitude power equations present values very accurate with the simulated strategies;
- The proposed magnitude direct voltage power ripple equation present results close to the simulated strategies, except to the APOC;
- During the voltage sag operation, it can be observed the direct voltage fluctuations and current ripple with the twice of fundamental frequency in the d.c. bus capacitors, that are proportional to the active power oscillations;

According to the proposed equation of direct voltage ripple (4.24), the active power ripple effects on the d.c. bus voltage can be reduced through three parameters:

- Increase of bus capacitance.
- Increase of the direct voltage operation value;
- Reduction of active power oscillation.

The first two points are related to technical limitations and costs increase. Therefore, the reduction of active power oscillation becomes the most viable alternative for the mitigation of direct voltage fluctuation during the LVRT operation.

Since the three-phase active and bus direct power are coupled, there will always be this tradeoff between d.c. bus ripple and a.c. power quality. Thus, an analysis of the power fluctuation impacts to the mains is necessary, and this will be done in the next chapter.

Chapter V

PCC VOLTAGE SUPPORT ANALYSIS

THE actual grid codes requires the reactive current injection during the voltage sag in order to increase the positive sequence voltage in the point of common coupling and help the voltage recovery. As previously discussed, grid-connected converters can mitigate other power quality issues simultaneously with the RCI requirement, through different power control strategies. In this chapter is discussed how the power control strategies, earlier presented, can affect the voltage support on the point of common coupling between the renewable power plant and the mains. Hence, a PCC voltage formulation as a function of the GFPC strategy is proposed, and a study case with a simulation of a 118(MW) RPP is performed.

5.1 Voltage orthogonal projection and reactive power flow

As discussed in Chapter 3: , the projection of the current vector **i** over the voltage **v** results in the active power transfer, while the projection of **i** over the orthogonal vector $\mathbf{v}_\perp$ results in reactive power flow, where $\mathbf{v}_\perp$ is obtained from **v** through the equation (3.10).

When the converter provides reactive current, from the GSC terminals point of view, the electrical mains behaves similar to an inductor. Hence, in the positive sequence the orthogonal vector $\mathbf{v}_\perp^+$ produced by the matrix (3.10) is lagging from the vector $\mathbf{v}^+$, as shown in Fig. 5.1(a). Therefore, the reactive current vector $\mathbf{i}_q^+$ aligned to $\mathbf{v}_\perp^+$ indicates a power flow from the converter to the grid and consequently, the vector $\mathbf{i}_q^+$ in opposite phase from $\mathbf{v}_\perp^+$ express the reactive power flow from the mains to the converter.

In the negative sequence the space vector rotates in contrary direction, in relation to the positive one. Hence, the orthogonal voltage vector $\mathbf{v}_\perp^-$ produced by the matrix (3.10) is leading from the vector $\mathbf{v}^-$, as presented in Fig. 5.1(b). Therefore, the reactive current vector $\mathbf{i}_q^-$ aligned to $\mathbf{v}_\perp^-$ indicate a power flow from the mains to the GSC, and thus, the $\mathbf{i}_q^-$ vector in opposite phase from $\mathbf{v}_\perp^-$express the reactive power flow from the converter to the mains.

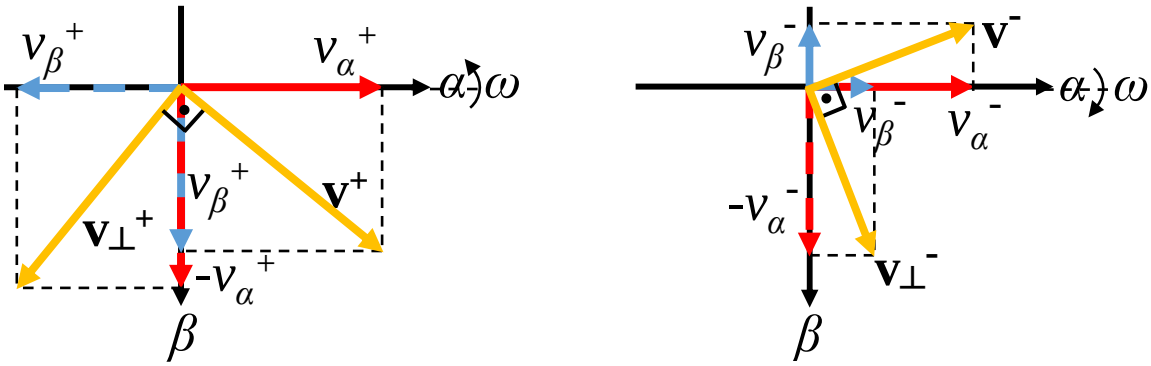

(a) (b)

Fig. 5.1: Orthogonal vector orientation in the (a) positive and (b) negative sequence
Source: Elaborated by the author

5.2 Dynamic model of the Point of Common Coupling voltage

The reactive current injection required by the actual GCs aims to support the PCC voltage recover, increasing the positive sequence voltage and helping to avoid the generating units disconnection during the voltage sag. In order to analyze the voltage support provided by the RPP, a PCC voltage mathematical model as a function of the GFPC is proposed. For this, the following considerations are made.

- **The fault occurs at a certain distance from the PCC, and the sequences coupling effects can be disregarded**. According to [35], voltages changes in the positive sequence also reflects in the negative and zero sequences at the faulted point and vice-versa. However, the electrical power systems protection philosophy has as priority to isolate the failure. Thus, disturbs occurrence of near to the plant connection will rapidly isolate it from the mains.
- **The positive and negative sequence impedances are equal**. The transmission lines transposition ensures this for most of the cases.
- **The net active and reactive delivered power during the LVRT operation is higher than zero**. As demonstrated in this section, in some strategies the positive and negative power present different flow direction. Nonetheless, the set points $P^* \geq 0$ and $Q^* \geq 0$ during the fault, which means no net active or reactive power consumption.

Fig. 5.2 presents a simplified equivalent circuit of the interface between the renewable power plant and the mains. $\mathbf{v}_g$, L_g and R_g are the grid Thevenin's equivalent voltage, inductance and resistance, $\mathbf{v}$ is the voltage at point of common coupling. Note that the PCC

representation does not have a connection with the ground due to the power transformer *Dy* winding connection, thus the zero sequence is not considered in the analysis.

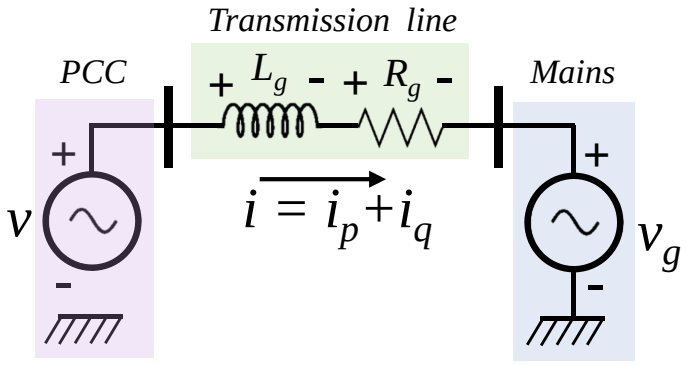

Fig. 5.2: Simplified model of grid connection point
Source: Elaborated by the author

Applying the Kirchoff's law to the circuit in the Fig. 5.2, the positive and negative voltage at PCC can be modeled by:

$$\mathbf{v}^+ = \mathbf{v}_g^+ + R_g\left(\mathbf{i}_p^+ + \mathbf{i}_q^+\right) + L_g\frac{d}{dt}(\mathbf{i}_p^+ + \mathbf{i}_q^+), \tag{5.1}$$

$$\mathbf{v}^- = \mathbf{v}_g^- + R_g\left(\mathbf{i}_p^- + \mathbf{i}_q^-\right) + L_g\frac{d}{dt}(\mathbf{i}_p^- + \mathbf{i}_q^-). \tag{5.2}$$

During the voltage ride through operation, the GSC and consequently the RPP, operates as a current source, because the GC establish the converter must provide its maximum current capacity, regardless the generated active power and RCI operational point. Therefore, in order to contemplate this behavior and perform a more general analysis, the power control strategies current notation in equations (4.25) and (4.26) are replaced in (5.1) and (5.2), as follows:

$$\begin{aligned}\mathbf{v}^+ = \mathbf{v}_g^+ + R_g\left(I_p\, k_p^+\,\frac{\mathbf{v}^+}{|\mathbf{v}^+|} + I_q\, k_q^+\,\frac{\mathbf{v}_\perp^+}{|\mathbf{v}^+|}\right) + \cdots \\ L_g\frac{d}{dt}\left(I_p\, k_p^+\,\frac{\mathbf{v}^+}{|\mathbf{v}^+|} + I_q\, k_q^+\,\frac{\mathbf{v}_\perp^+}{|\mathbf{v}^+|}\right),\end{aligned} \tag{5.3}$$

$$\begin{aligned}\mathbf{v}^- = \mathbf{v}_g^- + R_g\left(u\, I_p\, k_p^-\,\frac{\mathbf{v}^-}{|\mathbf{v}^-|} + u\, I_q\, k_q^-\,\frac{\mathbf{v}_\perp^-}{|\mathbf{v}^-|}\right) + \cdots \\ L_g\frac{d}{dt}\left(u\, I_p\, k_p^-\,\frac{\mathbf{v}^-}{|\mathbf{v}^-|} + u\, I_q\, k_q^-\,\frac{\mathbf{v}_\perp^-}{|\mathbf{v}^-|}\right).\end{aligned} \tag{5.4}$$

Using the stationary frame voltages equations (3.3), deriving and regrouping the correlated terms, the PCC voltages as a function of the GFPC strategy are given by:

$$\mathbf{v}^{+} = \mathbf{v}_g^{+} + R_{\boldsymbol{g}}\left(I_p\, k_p^{+}\, \frac{\mathbf{v}^{+}}{|\mathbf{v}^{+}|} + I_q\, k_q^{+}\, \frac{\mathbf{v}_{\perp}^{+}}{|\mathbf{v}^{+}|}\right) + \cdots$$
$$\omega L_g\left(-I_p\, k_p^{+}\, \frac{\mathbf{v}_{\perp}^{+}}{|\mathbf{v}^{+}|} + I_q\, k_q^{+}\, \frac{\mathbf{v}^{+}}{|\mathbf{v}^{+}|}\right), \tag{5.5}$$

$$\mathbf{v}^{-} = \mathbf{v}_g^{-} + R_{\boldsymbol{g}}\left(u\, I_p\, k_p^{-}\, \frac{\mathbf{v}^{-}}{|\mathbf{v}^{-}|} + u\, I_q\, k_q^{-}\, \frac{\mathbf{v}_{\perp}^{-}}{|\mathbf{v}^{-}|}\right) + \cdots$$
$$\omega L_g\left(u\, I_p\, k_p^{-}\, \frac{\mathbf{v}_{\perp}^{-}}{|\mathbf{v}^{-}|} - u\, I_q\, k_q^{-}\, \frac{\mathbf{v}^{-}}{|\mathbf{v}^{-}|}\right). \tag{5.6}$$

Based on the equations (5.5) and (5.6), it is possible to make some observations:

- The direct contributions to the PCC voltage magnitude $\mathbf{v}^{+}$ and $\mathbf{v}^{-}$ are associated to the active current flow over the resistive elements and reactive over the inductive ones.
- The impedance value and the current injection capacity define the RPP voltage support capability, i.e. how greater is the power plant in relation to the electrical power system.
- The *X/R* ratio has an important role in the voltage support through the reactive current injection proposed in the actual GCs.
- According to the equation (4.27), each strategy will require different values of I_p to provide the set-point power P^{*}. The reactive current I_q (assuming $k_q^{+} = 1$) is defined by the RCI requirement.

5.3 Power control strategies currents flow analyses

As presented in the Chapter 3: , several kinds of power control strategies can be used to mitigate other power quality issues simultaneously with the reactive current feed-in. Because they present different currents profile characteristics, the way of each strategy affects the PCC voltage also differs.

The ideal voltage restore is obtained by increasing the positive sequence to 1(pu) and reducing the negative sequence voltage to 0(pu) to obtain balanced voltages, and magnitudes close to the pre-fault condition [28,34]. However, according to the reference [34], to achieve the this objective, it is necessary to supply a considerable current through the negative sequence, generating high active and reactive power oscillations. Furthermore, this goal

cannot always be reached due to the low impedance (stiff grid) and RPP limited current capacity.

Some papers in literature aim to carry out the PCC voltage restore taking into account the converter power capacity, the grid impedance value and X/R ratio. However, the power control strategies discussed in this work have the focus in others power quality issues, such as reduction of power oscillations, sinusoidal balanced currents profile and etc. Hence, this section has the intention to evaluate how the power control strategies previously discussed can affect the voltage at the point of common coupling, take into account that the voltage restoration is not the main goal of power control strategies discussed in this work.

5.3.1 Positive and negative sequence compensation (PNSC)

Replacing the PNSC gains defined in Table II, i.e., $k_p^+ = k_q^+ = 1$ and $k_p^- = k_q^- = -1$, in the equations (4.25) and (4.26):

$$\mathbf{i}_p^* = I_p \frac{\mathbf{v}^+}{|\mathbf{v}^+|} - u\, I_p \frac{\mathbf{v}^-}{|\mathbf{v}^+|}, \tag{5.7}$$

$$\mathbf{i}_q^* = I_q \frac{\mathbf{v}_\perp^+}{|\mathbf{v}^+|} - u\, I_q \frac{\mathbf{v}_\perp^-}{|\mathbf{v}^-|}. \tag{5.8}$$

According to the equations (5.7) and (5.8), the PNSC strategy generates currents vectors $\mathbf{i}_p^+$, $\mathbf{i}_q^+$ that are parallel to $\mathbf{v}^+$, $\mathbf{v}_\perp^+$ and $\mathbf{i}_p^-$, $\mathbf{i}_q^-$ in opposite phase to $\mathbf{v}^-$ and $\mathbf{v}_\perp^-$, respectively, as can be seen in Fig. 5.3. This voltage and currents vectors disposition results in active and reactive power production thought the positive sequence and active consumption and reactive power production though the negative sequence.

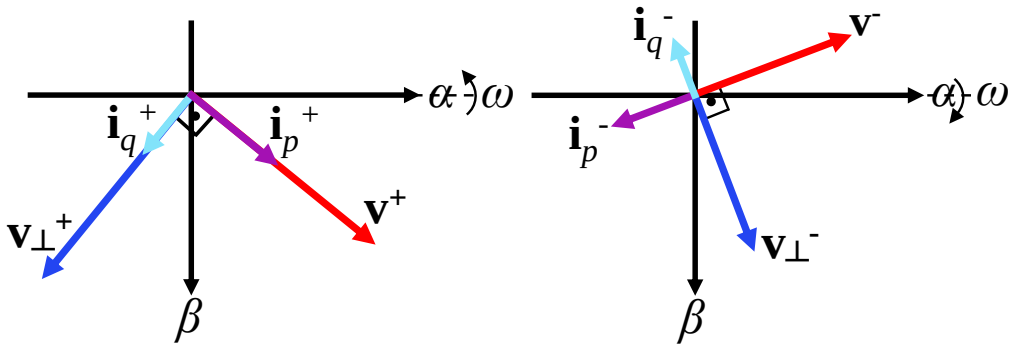

Fig. 5.3: (a) positive and (b) negative sequence current vector orientation in PNSC strategy
Source: Elaborated by the author

Therefore using the PNSC gains in the equations (5.5) and (5.6), it is obtained the PCC voltage expression for the PNSC, as follows:

$$\mathbf{v}^{+} = \mathbf{v}_g^{+} + R_g\left(I_p\ \frac{\mathbf{v}^{+}}{|\mathbf{v}^{+}|} + I_q\ \frac{\mathbf{v}_{\perp}^{+}}{|\mathbf{v}^{+}|}\right) + \cdots$$
$$\omega L_g\left(-I_p\ \frac{\mathbf{v}_{\perp}^{+}}{|\mathbf{v}^{+}|} + I_q\ \frac{\mathbf{v}^{+}}{|\mathbf{v}^{+}|}\right), \tag{5.9}$$

$$\mathbf{v}^{-} = \mathbf{v}_g^{-} + R_g\left(-u\ I_p\ \frac{\mathbf{v}^{-}}{|\mathbf{v}^{-}|} - u\ I_q\ \frac{\mathbf{v}_{\perp}^{-}}{|\mathbf{v}^{-}|}\right) + \cdots$$
$$\omega L_g\left(-u\ I_p\ \frac{\mathbf{v}_{\perp}^{-}}{|\mathbf{v}^{-}|} + u\ I_q\ \frac{\mathbf{v}^{-}}{|\mathbf{v}^{-}|}\right). \tag{5.10}$$

The PCC positive sequence voltage is increased for any value of I_p and I_q greater than zero. Nevertheless, the negative sequence voltage is decreased only if $\omega L_g/R_g < I_p^{-}/I_q^{-}$. Therefore, this strategy can increase the voltages unbalance for voltage sag conditions with high reactive current level.

5.3.2 Average active and reactive control (AARC)

Replacing the Table II AARC gains, $k_p^{+} = k_q^{+} = 1$ and $k_p^{-} = k_q^{-} = 1$, in the equations (4.25) and (4.26), the currents expressions are defined by:

$$\mathbf{i}_p^{*} = I_p\ \frac{\mathbf{v}^{+}}{|\mathbf{v}^{+}|} + u\ I_p\ \frac{\mathbf{v}^{-}}{|\mathbf{v}^{-}|}, \tag{5.11}$$

$$\mathbf{i}_q^{*} = I_q\ \frac{\mathbf{v}_{\perp}^{+}}{|\mathbf{v}^{+}|} + u\ I_q\ \frac{\mathbf{v}_{\perp}^{-}}{|\mathbf{v}^{-}|}. \tag{5.12}$$

Thus, second the equations (5.11) and (5.12), the currents vectors $\mathbf{i}_p^{+}$, $\mathbf{i}_q^{+}$, $\mathbf{i}_p^{-}$ and $\mathbf{i}_q^{-}$ are aligned with $\mathbf{v}^{+}$, $\mathbf{v}_{\perp}^{+}$, $\mathbf{v}^{-}$ and $\mathbf{v}_{\perp}^{-}$, respectively, as shown in Fig. 5.4. This behavior results in active and reactive power production through the positive sequence and active power production and reactive power consumption through the negative sequence.

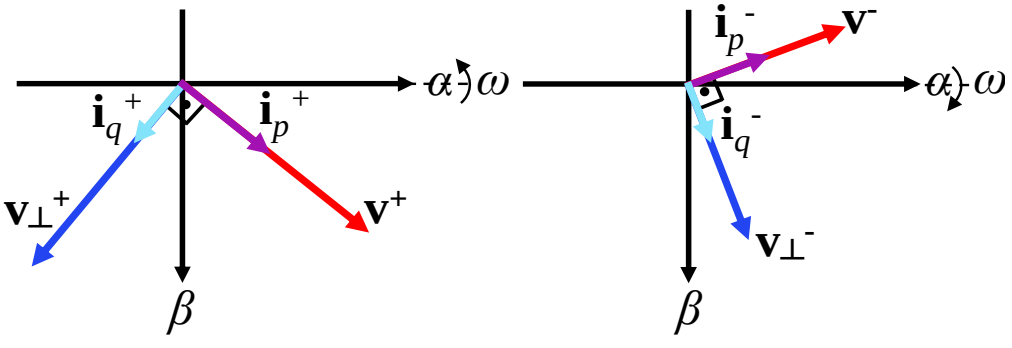

Fig. 5.4: (a) positive and (b) negative sequence current vector orientation in AARC strategy
Source: Elaborated by the author

The PCC voltage equations are obtained replacing the AARC gains in the equations (5.5) and (5.6), as follows:

$$\mathbf{v}^+ = \mathbf{v}_g^+ + R_g\left(I_p\ \frac{\mathbf{v}^+}{|\mathbf{v}^+|} + I_q\ \frac{\mathbf{v}_\perp^+}{|\mathbf{v}^+|}\right) + \cdots \\ \omega L_g\left(-I_p\ \frac{\mathbf{v}_\perp^+}{|\mathbf{v}^+|} + I_q\ \frac{\mathbf{v}^+}{|\mathbf{v}^+|}\right), \tag{5.13}$$

$$\mathbf{v}^- = \mathbf{v}_g^- + R_g\left(u\ I_p\ \frac{\mathbf{v}^-}{|\mathbf{v}^-|} + u\ I_q\ \frac{\mathbf{v}_\perp^-}{|\mathbf{v}^-|}\right) + \cdots \\ \omega L_g\left(u\ I_p\ \frac{\mathbf{v}_\perp^-}{|\mathbf{v}^-|} - u\ I_q\ \frac{\mathbf{v}^-}{|\mathbf{v}^-|}\right). \tag{5.14}$$

The currents flow decreases the negative sequence voltage only if $\omega L_g/R_g > I_p^-/I_q^-$, that is, this strategy can help in the voltage's equalization during the voltage sag when a high reactive current level is required, which is a complementary comportment in relation to the PNSC.

5.3.3 Balanced positive sequence control (BPSC)

In the BPSC strategy no other ancillary services than the reactive current injection is performed during the voltage sag. The BPSC instantaneous currents expressions, obtained through the gains $k_p^+ = k_q^+ = 1$ and $k_p^- = k_q^- = 0$, in the equations (4.25) and (4.26), are:

$$\mathbf{i}_p^* = I_p\ \frac{\mathbf{v}^+}{|\mathbf{v}^+|}, \tag{5.15}$$

$$\mathbf{i}_q^* = I_q\ \frac{\mathbf{v}_\perp^+}{|\mathbf{v}^+|}. \tag{5.16}$$

The current injection is performed only by the positive sequence, generating the current vectors $\mathbf{i}_p^+$, $\mathbf{i}_q^+$ parallel to $\mathbf{v}^+$, $\mathbf{v}_\perp^+$, respectively, and null negative sequence currents, as can be seen in the Fig. 5.5.

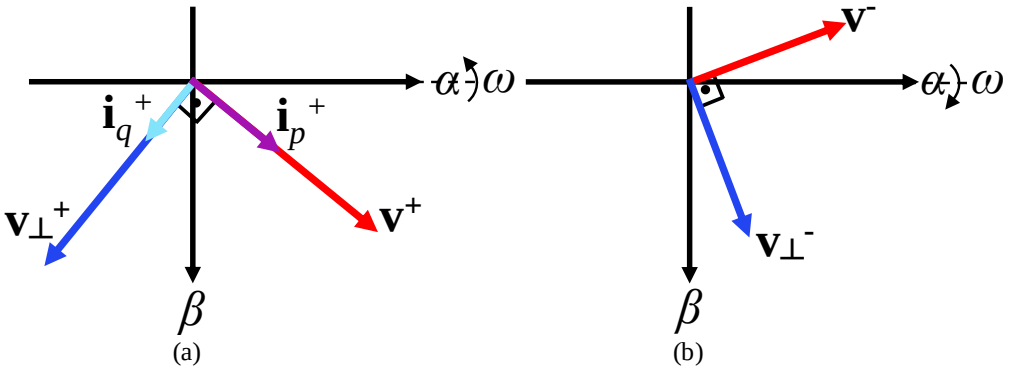

Fig. 5.5: (a) positive and (b) negative sequence current vector orientation in BPSC strategy
Source: Elaborated by the author

In a similar way to the zero sequence, from the mains point of view the RPP negative sequence is an open circuit, which can be better understood replacing the BPSC gains $k_p^+ = k_q^+ = 1$ and $k_p^- = k_q^- = 0$ in the equations (5.5) and (5.6), as follow:

$$\mathbf{v}^+ = \mathbf{v}_g^+ + R_g \left(I_p \frac{\mathbf{v}^+}{|\mathbf{v}^+|} + I_q \frac{\mathbf{v}_\perp^+}{|\mathbf{v}^+|} \right) + \cdots \omega L_g \left(-I_p \frac{\mathbf{v}_\perp^+}{|\mathbf{v}^+|} + I_q \frac{\mathbf{v}^+}{|\mathbf{v}^+|} \right), \tag{5.17}$$

$$\mathbf{v}^- = \mathbf{v}_g^-. \tag{5.18}$$

The magnitude of $\mathbf{v}^-$ remains the same regardless the value of I_p and I_q, i.e., it is not possible to reduce the voltage unbalance using the BPSC strategy.

5.3.4 Reactive power oscillation cancellation (RPOC)

The RPOC gains are defined by $k_p^+ = k_q^+ = 1$ and $k_p^- = 1$ and $k_q^- = -1$ in Table II. Replace them in equations (4.25) and (4.26), it is obtained the RPOC currents expressions:

$$\mathbf{i}_p^* = I_p \frac{\mathbf{v}^+}{|\mathbf{v}^+|} + u\, I_p \frac{\mathbf{v}^-}{|\mathbf{v}^-|}, \tag{5.19}$$

$$\mathbf{i}_q^* = I_q \frac{\mathbf{v}_\perp^+}{|\mathbf{v}^+|} - u\, I_q \frac{\mathbf{v}_\perp^-}{|\mathbf{v}^-|}. \tag{5.20}$$

Hence, RPOC generates currents vectors $\mathbf{i}_p^+$ and $\mathbf{i}_q^+$ are aligned to $\mathbf{v}^+$, $\mathbf{v}_\perp^+$, respectively, meanwhile the negative sequence $\mathbf{i}_p^-$ is aligned to $\mathbf{v}^-$ and $\mathbf{i}_q^-$ in opposite to $\mathbf{v}_\perp^-$, as shown in Fig. 5.6. It results in active and reactive power production through the positive sequence and the negative sequence.

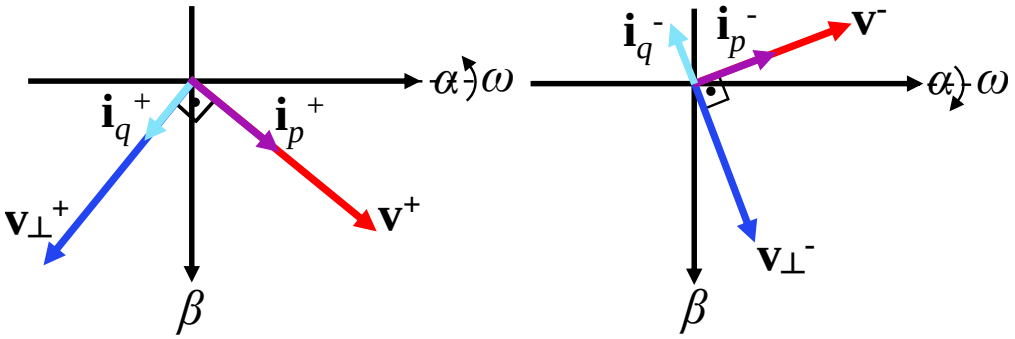

Fig. 5.6: (a) positive and (b) negative sequence current vector orientation in RPOC strategy
Source: Elaborated by the author

Therefore, using the RPOC gains in the generalized model of the PCC voltage (5.5) and (5.6):

$$\mathbf{v}^+ = \mathbf{v}_g^+ + R_g \left(I_p \ \frac{\mathbf{v}^+}{|\mathbf{v}^+|} + I_q \ \frac{\mathbf{v}_\perp^+}{|\mathbf{v}^+|} \right) + \cdots \\ \omega L_g \left(-I_p \ \frac{\mathbf{v}_\perp^+}{|\mathbf{v}^+|} + I_q \ \frac{\mathbf{v}^+}{|\mathbf{v}^+|} \right), \tag{5.21}$$

$$\mathbf{v}^- = \mathbf{v}_g^- + R_g \left(u \ I_p \ \frac{\mathbf{v}^-}{|\mathbf{v}^-|} - u \ I_q \ \frac{\mathbf{v}_\perp^-}{|\mathbf{v}^-|} \right) + \cdots \\ \omega L_g \left(u \ I_p \ \frac{\mathbf{v}_\perp^-}{|\mathbf{v}^-|} + u \ I_q \ \frac{\mathbf{v}^-}{|\mathbf{v}^-|} \right). \tag{5.22}$$

The active and/or reactive current injection can increase the negative sequence voltage and consequently, the cancellation of reactive power oscillation contributes to the phase voltages unbalanced intensification at PCC.

5.3.5 Active power oscillation cancellation (APOC)

Replacing the Table II APOC gains, $k_p^+ = k_q^+ = 1$, $k_p^- = -1$ and $k_q^- = 1$ in the equations (4.25) and (4.26), the currents expressions are:

$$\mathbf{i}_p^* = I_p \ \frac{\mathbf{v}^+}{|\mathbf{v}^+|} + u \ I_p \ \frac{\mathbf{v}^-}{|\mathbf{v}^-|}, \tag{5.23}$$

$$\mathbf{i}_q^* = I_q \ \frac{\mathbf{v}_\perp^+}{|\mathbf{v}^+|} - u \ I_q \ \frac{\mathbf{v}_\perp^-}{|\mathbf{v}^-|}. \tag{5.24}$$

The currents vectors generated by the APOC are shown in Fig. 5.7, where $\mathbf{i}_p^+$ and $\mathbf{i}_q^+$ are aligned to $\mathbf{v}^+$and $\mathbf{v}_\perp^+$, respectively, $\mathbf{i}_p^-$ antiparallel to $\mathbf{v}^-$ and $\mathbf{i}_q^-$ parallel to $\mathbf{v}_\perp^-$, resulting in the power production though the positive sequence and consumption of active and reactive power thought the negative sequence.

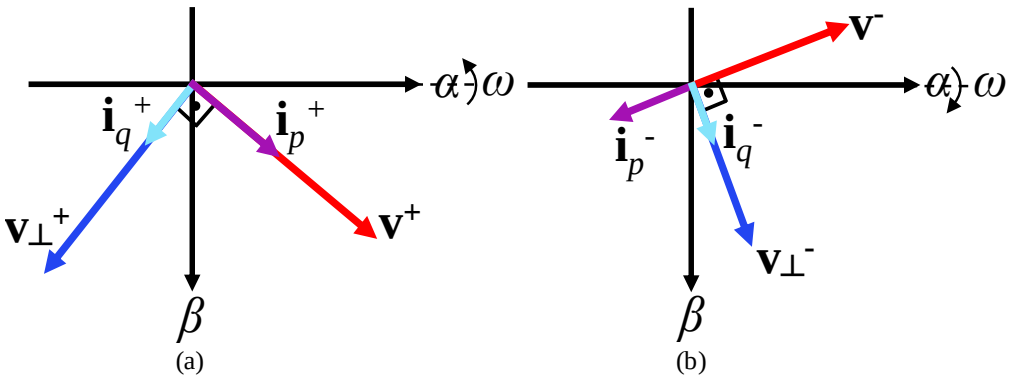

Fig. 5.7: (a) positive and (b) negative sequence current vector orientation in APOC strategy
Source: Elaborated by the author

Therefore, applying the APOC gains in the PCC voltage equations (5.5) and (5.6):

$$\mathbf{v}^+ = \mathbf{v}_g^+ + R_g\left(I_p\ \frac{\mathbf{v}^+}{|\mathbf{v}^+|} + I_q\ \frac{\mathbf{v}_\perp^+}{|\mathbf{v}^+|}\right) + \cdots \\ \omega L_g\left(-I_p\ \frac{\mathbf{v}_\perp^+}{|\mathbf{v}^+|} + I_q\ \frac{\mathbf{v}^+}{|\mathbf{v}^+|}\right), \tag{5.25}$$

$$\mathbf{v}^- = \mathbf{v}_g^- + R_g\left(-u\ I_p\ \frac{\mathbf{v}^-}{|\mathbf{v}^-|} + u\ I_q\ \frac{\mathbf{v}_\perp^-}{|\mathbf{v}^-|}\right) + \cdots \\ \omega L_g\left(-u\ I_p\ \frac{\mathbf{v}_\perp^-}{|\mathbf{v}^-|} - u\ I_q\ \frac{\mathbf{v}^-}{|\mathbf{v}^-|}\right). \tag{5.26}$$

The active and/or reactive power injection using the APOC strategy can reduces the negative sequence voltage magnitude, and consequently helps in the voltage equalization at PCC. Obviously, this voltage restoration support will be associated to the previously mentioned factors. However, this strategy presents two important contributions; the cancellation of active power oscillation, reducing the effects of voltage sag to the power electronic converter, and the improvement of PCC voltage profile.

5.4 Case study

In order to evaluate the discussion in relation to the voltage support provided by the power control strategies during the LVRT operation, simulations from a renewable power plant are performed using the Matlab/Simulink software. The simulated RPP present an arrangement similar to the Fig. 2.1 and its parameters are described in Table VI. The following restraints are imposed to the simulation:

- The generating units operate with rated power before the fault occurrence and return to this condition after the fault clearance.

- The fault occurs at a certain distance from the PCC, and the sequences coupling effects can be disregarded, i.e., the voltage sags are created by directly modifying the mains voltage [35].

All the graphs are in per unit in relation to the rated values of voltage, current, power, etc. The same RCI criteria for the study case in section 4.4 are adopted here.

Table VI: RPP and transmission line parameters

Parameter	Symb.	Value	Unity
Mains line voltage	$Vg_{ph\text{-}ph}$	138	kV
Transmission line reactance	X_u	0.4954	Ω/km
Transmission line resistance	R_u	0.0908	Ω/km
Transmission line length	l	20	km
PCC transformer power	P_{tr}	140	MW
PCC transformer impedance	Z_{tr}	0,1	pu
PCC transformer X/R	X/R_{tr}	100	-
POC line voltage	$Vpoc_{ph\text{-}ph}$	34.5	kV
Renewable power plant power peak	P_{RPP}	118	MW

5.4.1 Specific case analysis

Similar to the section 4.4.1, initially the voltage support are evaluated for a specific case, where the mains voltages are described by va = 1(pu), vb = vc = 0.4(pu) resulting in a positive sequence voltage $|\mathbf{v}^+| = 0.6$(pu) and an unbalanced factor u = 1/3, as shown in Fig. 5.8.

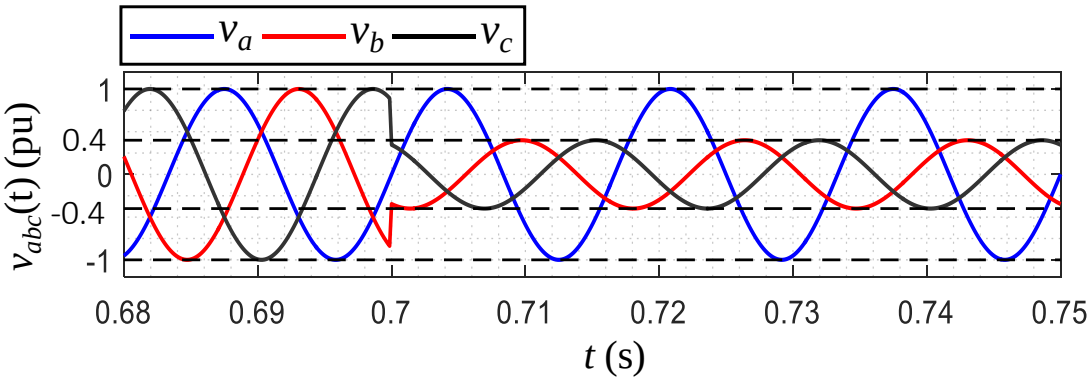

Fig. 5.8: Mains phase voltage during the LVRT
Source: Elaborated by the author

Fig. 5.9 presents a comparison between the grid and PCC voltage vectors trajectories for different sinusoidal power control strategies analyzed in this work. The PNSC (Fig. 5.9(a)) and AARC (Fig. 5.9(b)) strategies present slightly changes in the negative sequence voltage

magnitude. Since the $I_q > I_p$ for both strategies, the PNSC increase while the AARC decrease the negative sequence voltage magnitude. Consequently, the PNSC PCC voltage trajectory has greater eccentricity in relation to the AARC.

The BPSC (Fig. 5.9(c)) does not change the negative sequence voltage. Consequently, the PCC voltage vector is proportionally increased in all directions.

The RPOC (Fig. 5.9(d)) increase the PCC voltage negative sequence, increasing the eccentricity of the PCC voltage vector path in relation to the mains. The APOC (Fig. 5.9(e)) decrease the negative sequence, and the PCC voltage vector has a more circular shape, in comparison to the grid.

The effects of positive and negative sequence changes in the PCC voltages can be better understood through natural frame voltages in Fig. 5.10, Table VII and Table VIII. The positive and negative voltage increase in the PNSC (Fig. 5.10(a)) raise up all the voltages, generating an overvoltage of 0.125(pu) in the non-faulted phase. In the AARC (Fig. 5.10(b)) the negative sequence reduction, even small, helps in the overvoltage reduction, where the non-faulted phase increases 0.078(pu).

The BPSC (Fig. 5.10(c)) performs the feed-in power control exclusively through the positive sequence, in total agreement to the actual GCs. Thus, the magnitudes are raised in the same proportion in the three voltages and the healthy phase present an overvoltage of 0.121(pu).

In the RPOC (Fig. 5.10(d)), the negative sequence increase causes the raising of the healthy phase more than the faulted ones. It can be explained through RPOC currents magnitudes described in Table VII, where the highest voltage and currents magnitudes happen in the same phase.

The APOC (Fig. 5.10(e)) strategy is the closest strategy to the ideal voltage support condition, since there is an increase in the positive sequence voltage, and differently from the AARC the APOC negative sequence reduction is performed by the active and reactive current. It can be explained through the APOC currents magnitudes in Table VII, where the smaller phase voltages amplitudes have the highest currents magnitude and vice-versa.

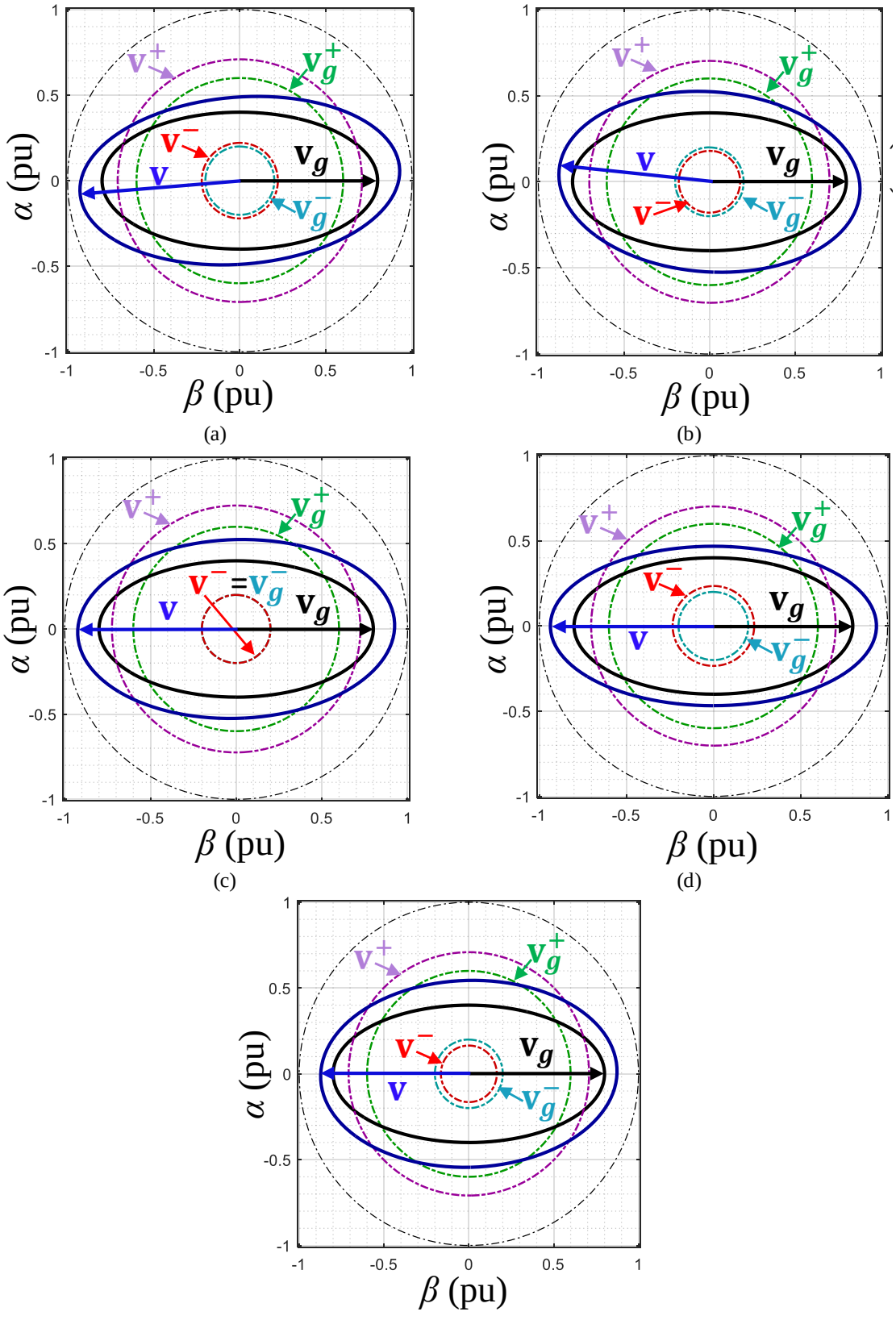

Fig. 5.9: Gird and PCC vector trajectory comparison for (a) PNSC, (b) AARC, (c) BPSC, (d) RPOC and (e) APOC.

Source: Elaborated by the author

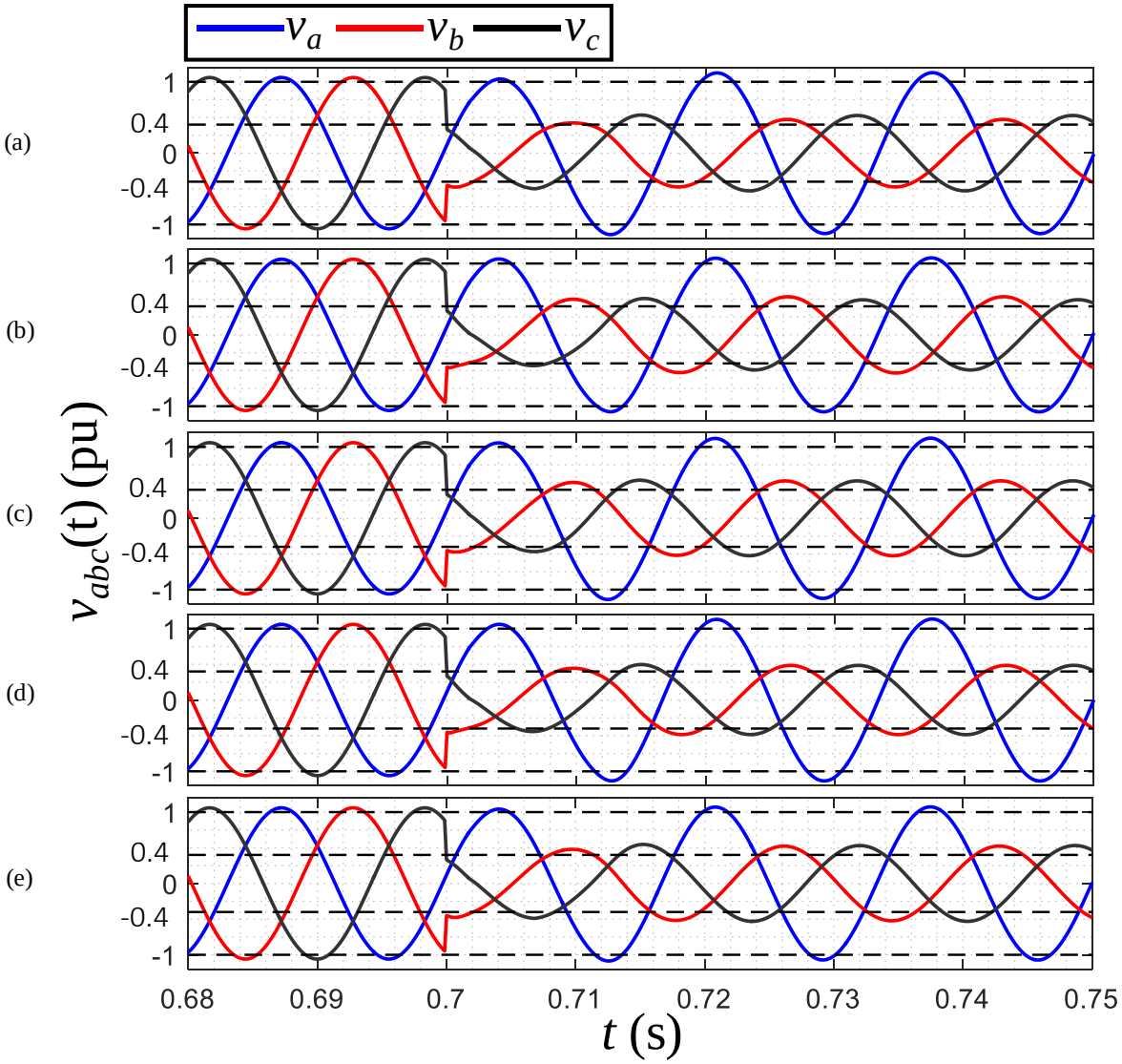

Fig. 5.10: Natural frame voltages at PCC for (a) PNSC, (b) AARC, (c) BPSC, (d) RPOC and (e) APOC
Source: Elaborated by the author

Table VII: Voltage magnitudes, unbalanced factor and PCC currents for different power control strategies

	va(pu)	*vb*(pu)	*vc*(pu)	*u*	*ia(pu)*	*ib(pu)*	*ic(pu)*
Mains	1.000	0.400	0.400	0.333	-	-	-
PNSC	1.125	0.472	0.527	0.312	0.952	0.552	1.000
AARC	1.078	0.535	0.491	0.255	0.612	1.000	0.722
BPSC	1.121	0.524	0.524	0.276	1.000	1.000	1.000
RPOC	1.132	0.484	0.486	0.334	1.000	0.661	0.662
APOC	1.073	0.523	0.531	0.232	0.560	0.990	1.000

Source: Elaborated by the author

Table VIII: PCC Voltage magnitudes increase in relation to the electrical mains

	Δva(pu)	Δvb(pu)	Δvc(pu)
PNSC	0.125	0.072	0.127
AARC	0.078	0.135	0.091
BPSC	0.121	0.124	0.124
RPOC	0.132	0.084	0.086
APOC	0.073	0.123	0.131

Source: Elaborated by the author

5.4.2 Generalized analysis

Similar to the section 4.4.2, the voltage support analyses can be extent to different points of RCI curve. For this, the voltage v_a is keeping in 1(pu), while v_b and v_c are decreased for each simulation interaction, as exemplified in the Fig. 4.21.

Fig. 5.11 presents a comparison between the positive and negative sequence voltages magnitude in the PCC and in the mains for different power control strategies. In the positive sequence (Fig. 5.11(a)), the PCC voltage is always greater than the mains. All the strategies present similar results, except by the BPSC, where the positive sequence magnitude is slightly greater than the others, since it does not perform the power injection through the negative sequence, thus a greater currents magnitude is necessary to inject the active power set-point.

The negative sequence magnitude is shown in Fig. 5.11(a). The APOC presents the best scenario in relation to the voltage restore, since it reduces the negative sequence voltage and increase the positive sequence. Despite The RPOC increases the positive sequence, it also increases the negative sequence voltage. The AARC and PNSC voltage support effects change with the reactive current level and as previously discussed and the BPSC does not change the negative sequence.

Fig. 5.12 presents a comparison between the grid and PCC unbalance factor for different power control strategies. The PNSC, AARC and BPSC reduce the PCC unbalance factor in relation to the grid. However, as the proportion of reactive current increases the PNSC tends to equalize to the grid value, whereas the AARC decreases. The RPOC practically keeps the imbalance between the PCC in relation to the mains, meanwhile the APOC provides the greatest reduction among the strategies analyzed in this work. For values of u_{grid} greater than 0.4, the generating units capacity should be used to feed-in balanced reactive currents to the mains, and no additional ancillary services can be performed.

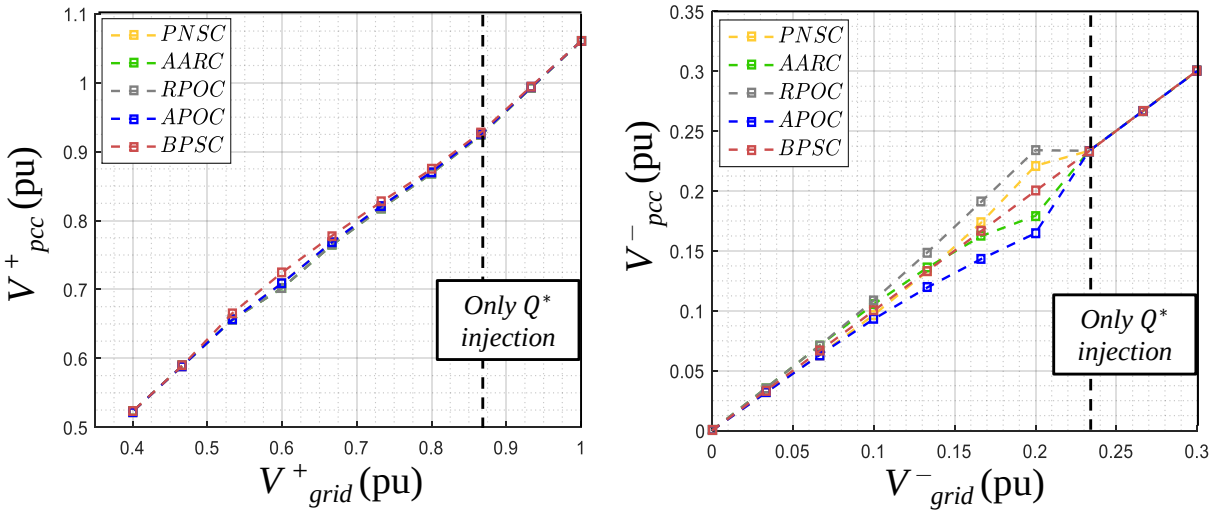

(a) (b)

Fig. 5.11: PCC and mains voltage comparison (a) positive sequence voltage and (b) negative sequence voltage for different power control strategies
Source: Elaborated by the author

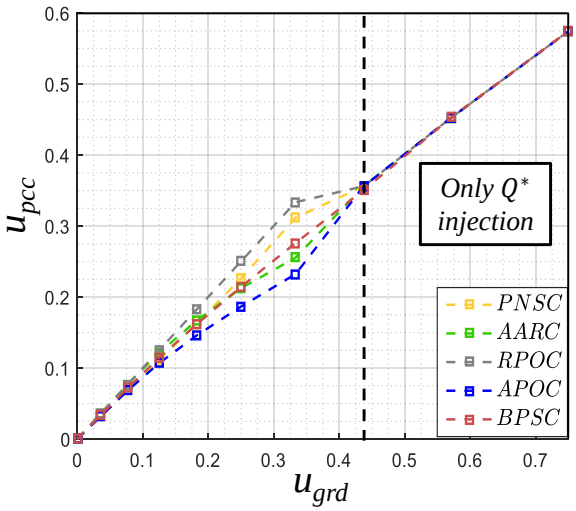

Fig. 5.12: PCC and mains unbalance factor comparison for different power control strategies
Source: Elaborated by the author

5.5 Chapter Conclusions

The objective of this chapter was discussing the voltage support provided by the power control strategies previously mentioned in this work. For this was proposed a PCC voltage formulation as a function of the GFPC strategy and a case study with simulation of 118(MW) RPP was performed.

The optimal voltage restore condition is achieved through the fulfillment of two conditions:

- Increasing of the PCC positive sequence voltages to 1(pu) and consequently restore the voltage magnitudes to pre-fault condition.
- Decreasing the PCC negative sequence voltages to 0(pu) and consequently reduce the unbalance between the phases.

The match of these objectives is associated with the grid stiffness in relation to the renewable power plant. Some papers in literature aim to carry out the PCC voltage restore taking into account the converter power capacity, the grid impedance value and X/R ratio. However, the power control strategies discussed in this work have the focus in others power quality issues, such as reduction of power oscillations, sinusoidal balanced currents profile, etc. Hence the objective of this chapter was discussing the effects of these power control strategies in the PCC voltage support.

The study case simulation results corroborate to the analyses performed through the proposed PCC voltage equations. Therefore, the voltage improvement provided by the AARC and PNSC depends on the operational point in the RCI curve.

The RPOC deteriorates the voltage at point of common coupling, since it increases the negative sequence voltage by means the production of active and reactive power through the negative sequence, generating overvoltage in the heathy phases.

The BPSC, which aligns with the actual GCs requirement, only changes the positive sequence, increasing the three PCC voltages with the same value, which may cause overvoltage in the non-faulted phases.

The APOC can reduce the negative sequence independently from the *X/R* ratio and increase the positive sequence voltage, becoming the closest strategy to the ideal voltage support condition.

Chapter VI

CONCLUSIONS

The aim of this work was evaluating the power control strategies AARC, PNSC, BPSC, RPOC and APOC in relation to the power qualities issues, such as active and reactive power oscillations and discuss their effects to the three-phase three-wire grid-connected converters and to the electrical mains, given focus to meeting the RCI grid code requirements.

The first contribution of this work is the development of formulations that allow quantifying the grid power oscillation magnitude generated by each sinusoidal reference currents power control strategies analyzed in this work. In the 2 (MW) case study, the proposed equations present values very accurate with the simulations in the different operation points over the RCI curve requirement.

As the second contribution was developed of an equation that approximate the d.c. bus voltage ripple as a function of power control strategies that generate sinusoidal currents. Due to the mathematical approximations to obtain an analytical expression, the direct voltage ripple equation presents a deviation in relation to the simulation results. A better accuracy can obtained if the LCL filter elements dynamics are taken into account. Moreover, it was not quantified how much the damping of active power oscillation can reduce the thermal stress in the d.c. link capacitors.

The third and fourth contributions are a time domain equation in that describes the point of common coupling voltage and the analysis of the positive and negative sequence power flow for the power control strategies that generate sinusoidal reference currents. The behavior predicted by the proposed equation is corroborated by the case study of the 118(MW) renewable power plant. However, the proposed model does not contemplate the coupling between the sequence components during a short circuit, for example.

6.1 Future works

In view of the gaps mentioned above, the following future works proposals are carried out:

- Elaboration of an equation that take into account the LCL filter dynamic, allow to achieve more accurate results including when the active power is null in the grid.
- Deeper study of the power control effects on the converter life time, quantifying the thermal stress during the voltage sags.
- Development of more complex PCC voltage models that contemplate a wide range of grid fault cases, in order to has a more precise analysis of the negative sequence currents injection in the power electrical system.

6.2 Author publications

The master's thesis results in the following publications:

- Silva, Rafael M.; Matos, Frederico F. V.; Silva, Joao L. ; Gonçalves, Waner W. A.; Rezende, Guilherme M.; Souza, Clodualdo V. ; Mendes, Victor F. . Parameter determination of permanent magnet synchronous machine and sensorless algorithm implementation based on sliding mode observer. In: 2018 *Simposio Brasileiro de Sistemas Eletricos* (SBSE) [*VII Brazilian Electrical Systems Symposium* (SBSE)], 2018, Niteroi. 2018 p. 1.
- Silva, Rafael M.; Paula, Camilo L. M.; Matos, Frederico F. V.; Rezende, Guilherme M.; Souza, Clodualdo V.; Mendes, Victor F.. Design and commissioning of wind generation system studies workbench using permanent magnet synchronous machine. In: *2017 Brazilian Power Electronics Conference* (COBEP), 2017, Juiz de Fora. p. 1.
- Some of the obtained results in this thesis were used in a paper elaboration that was submitted to "Electric Power System Research Journal" and currently is under review.

Moreover, the following articles were published in the work co-related areas:

- da Silva, J. L.; dos Reis, G. L.; Silva, R. M.; Seleme, S. I.; Meynard, T. A.; Llor, a. M.. Design, modeling and identification of the Mains Side Converter in an 11.7 kW wind/photovoltaic hybrid renewable generation system. In: *2017 IEEE 8th International Symposium on Power Electronics for Distributed Generation Systems* (PEDG), 2017, Florianopolis. p. 1.
- da Silva, J. L. ; dos Reis, G. L.; Silva, R. M.; Seleme, S. I.; Meynard, T. A.; Llor, a. M.. Design, modeling and identification of the Generation Side Converter in an 11.7 kW wind/photovoltaic hybrid renewable generation system. In: 2017 IEEE 8th

International Symposium on Power Electronics for Distributed Generation Systems (PEDG), 2017, Florianopolis. p. 1.

- Santos, Gilvan M.; Rezende, Guilherme M.; Souza, Paulo G.; Sousa, Clodualdo V. ; Ferreira, Tiago s.; Silva, Rafael M.; Mendes, Victor F. . Development of a 10 kVA wind energy conversion system prototype using the DFIG technology. In: *2018 Simposio Brasileiro de Sistemas Eletricos* (SBSE) [VII Brazilian Electrical Systems Symposium (SBSE)], 2018, Niteroi. p. 1.

REFERENCES

[1] REN21, Renewables 2018 - Global Status Report, (2018). http://www.ren21.net/wp-content/uploads/2018/06/17-8652_GSR2018_FullReport_web_final_.pdf.

[2] The impacts of wind and solar on grid flexibility requirements in the Electric Reliability Council of Texas, Energy. 123 (2017) 637–654. doi:10.1016/j.energy.2017.02.021.

[3] ONS - Operados Nacional do Sistema Elétrico, Resultados da Operação: Historico da Operação, ONS - Operador Nacional do Sistema Elétrico. (n.d.). http://ons.org.br:80/paginas/resultados-da-operacao/historico-da-operacao (accessed November 2, 2018).

[4] Danish Energy Agency, Annual and monthly statistics, Energistyrelsen. (2018). https://ens.dk/en/our-services/statistics-data-key-figures-and-energy-maps/annual-and-monthly-statistics (accessed November 2, 2018).

[5] Fraunhofer ISE, Annual Electricity Generation in Germany, Fraunhofer ISE. (n.d.). https://www.energy-charts.de/energy.htm?source=all-sources&period=annual&year=all (accessed November 2, 2018).

[6] Red Eléctrica de España (REE), National statistical series, Red Eléctrica de España (REE). (n.d.). https://www.ree.es/en/statistical-data-of-spanish-electrical-system/statistical-series/national-statistical-series (accessed November 2, 2018).

[7] M. Tsili, S. Papathanassiou, A review of grid code technical requirements for wind farms, IET Renewable Power Generation. 3 (2009) 308–332. doi:10.1049/iet-rpg.2008.0070.

[8] M. Altin, Ö. Göksu, R. Teodorescu, P. Rodriguez, B. Jensen, L. Helle, Overview of recent grid codes for wind power integration, in: 2010 12th International Conference on Optimization of Electrical and Electronic Equipment, 2010: pp. 1152–1160. doi:10.1109/OPTIM.2010.5510521.

[9] Operador Nacional do Sistema Elétrico (ONS), Requisitos técnico mínimos para a conexão às instalações de transmissão, (2015).

[10] Energinet, Technical Regulation for wind power plants above 11kW, (2016).

[11] Tennet, Grid Code for High and Extra High voltage, (2015).

[12] Red Eléctrica de España (REE), Requisitos de respuesta frente a huecos de tensión de las instalaciones eólica, (2006).

[13] X. Du, Y. Wu, S. Gu, H. Tai, P. Sun, Y. Ji, Power oscillation analysis and control of three-phase grid-connected voltage source converters under unbalanced grid faults, IET Power Electronics. 9 (2016) 2162–2173. doi:10.1049/iet-pel.2015.0804.

[14] P.. Rodriguez, A.V. Timbus, R.. Teodorescu, M.. Liserre, F.. Blaabjerg, Flexible Active Power Control of Distributed Power Generation Systems During Grid Faults, IEEE Transactions on Industrial Electronics. 54 (2007) 2583–2592. doi:10.1109/TIE.2007.899914.

[15] P. RodrÍguez, A. Timbus, R. Teodorescu, M. Liserre, F. Blaabjerg, Reactive Power Control for Improving Wind Turbine System Behavior Under Grid Faults, IEEE Transactions on Power Electronics. 24 (2009) 1798–1801. doi:10.1109/TPEL.2009.2014650.

[16] P. Rodriguez, A. Luna, J.R. Hermoso, I. Etxeberria-Otadui, R. Teodorescu, F. Blaabjerg, Current control method for distributed generation power generation plants under grid fault conditions, in: IECON 2011 - 37th Annual Conference of the IEEE Industrial Electronics Society, IEEE, Melbourne, Vic, Australia, 2011: pp. 1262–1269. doi:10.1109/IECON.2011.6119490.

[17] Fei Wang, J.L. Duarte, M.A.M. Hendrix, Pliant Active and Reactive Power Control for Grid-Interactive Converters Under Unbalanced Voltage Dips, IEEE Transactions on Power Electronics. 26 (2011) 1511–1521. doi:10.1109/TPEL.2010.2052289.

[18] M. Castilla, J. Miret, J.L. Sosa, J. Matas, L.G. d Vicuña, Grid-Fault Control Scheme for Three-Phase Photovoltaic Inverters With Adjustable Power Quality Characteristics, IEEE Transactions on Power Electronics. 25 (2010) 2930–2940. doi:10.1109/TPEL.2010.2070081.

[19] J.L. Sosa, M. Castilla, J. Miret, J. Matas, Y.A. Al-Turki, Control Strategy to Maximize the Power Capability of PV Three-Phase Inverters During Voltage Sags, IEEE Transactions on Power Electronics. 31 (2016) 3314–3323. doi:10.1109/TPEL.2015.2451674.

[20] A.F. Cupertino, L.S. Xavier, E.M.S. Brito, V.F. Mendes, H.A. Pereira, Benchmarking of power control strategies for photovoltaic systems under unbalanced conditions, International Journal of Electrical Power & Energy Systems. 106 (2019) 335–345. doi:10.1016/j.ijepes.2018.10.014.

[21] A.J. Roscoe, S.J. Finney, G.M. Burt, Tradeoffs Between AC Power Quality and DC Bus Ripple for 3-Phase 3-Wire Inverter-Connected Devices Within Microgrids, IEEE Transactions on Power Electronics. 26 (2011) 674–688. doi:10.1109/TPEL.2011.2105892.

[22] Ö. Göksu, R. Teodorescu, C.L. Bak, F. Iov, P.C. Kjær, Instability of Wind Turbine Converters During Current Injection to Low Voltage Grid Faults and PLL Frequency Based Stability Solution, IEEE Transactions on Power Systems. 29 (2014) 1683–1691. doi:10.1109/TPWRS.2013.2295261.

[23] M. Altin, Ö. Göksu, P. Sørensen, A. Morales, J. Fortmann, F.J. Buendia, Phase angle calculation dynamics of type-4 wind turbines in rms simulations during severe voltage dips, IET Renewable Power Generation. 10 (2016) 1069–1186. doi:10.1049/iet-rpg.2015.0501.

[24] P. Rodriguez, G. Medeiros, A. Luna, M.C. Cavalcanti, R. Teodorescu, Safe current injection strategies for a STATCOM under asymmetrical grid faults, in: 2010 IEEE Energy Conversion Congress and Exposition, 2010: pp. 3929–3935. doi:10.1109/ECCE.2010.5617794.

[25] A. Camacho, M. Castilla, J. Miret, A. Borrell, L.G. de Vicuña, Active and Reactive Power Strategies With Peak Current Limitation for Distributed Generation Inverters During Unbalanced Grid Faults, IEEE Transactions on Industrial Electronics. 62 (2015) 1515–1525. doi:10.1109/TIE.2014.2347266.

[26] E. Afshari, G.R. Moradi, R. Rahimi, B. Farhangi, Y. Yang, F. Blaabjerg, S. Farhangi, Control Strategy for Three-Phase Grid-Connected PV Inverters Enabling Current Limitation Under Unbalanced Faults, IEEE Transactions on Industrial Electronics. 64 (2017) 8908–8918. doi:10.1109/TIE.2017.2733481.

[27] M.A.G. López, J.L.G. de Vicuña, J. Miret, M. Castilla, R. Guzmán, Control Strategy for Grid-Connected Three-Phase Inverters During Voltage Sags to Meet Grid Codes and to

Maximize Power Delivery Capability, IEEE Transactions on Power Electronics. 33 (2018) 9360–9374. doi:10.1109/TPEL.2018.2792478.

[28] A. Camacho, M. Castilla, J. Miret, J.C. Vasquez, E. Alarcon-Gallo, Flexible Voltage Support Control for Three-Phase Distributed Generation Inverters Under Grid Fault, IEEE Transactions on Industrial Electronics. 60 (2013) 1429–1441. doi:10.1109/TIE.2012.2185016.

[29] J. Miret, A. Camacho, M. Castilla, L.G. de Vicuña, J. Matas, Control Scheme With Voltage Support Capability for Distributed Generation Inverters Under Voltage Sags, IEEE Transactions on Power Electronics. 28 (2013) 5252–5262. doi:10.1109/TPEL.2013.2246190.

[30] M. Castilla, J. Miret, A. Camacho, J. Matas, L.G. de Vicuña, Voltage Support Control Strategies for Static Synchronous Compensators Under Unbalanced Voltage Sags, IEEE Transactions on Industrial Electronics. 61 (2014) 808–820. doi:10.1109/TIE.2013.2257141.

[31] A. Camacho, M. Castilla, J. Miret, R. Guzman, A. Borrell, Reactive Power Control for Distributed Generation Power Plants to Comply With Voltage Limits During Grid Faults, IEEE Transactions on Power Electronics. 29 (2014) 6224–6234. doi:10.1109/TPEL.2014.2301463.

[32] J. Miret, A. Camacho, M. Castilla, J.L.G. de Vicuña, J. de la Hoz, Reactive current injection protocol for low-power rating distributed generation sources under voltage sags, IET Power Electronics. 8 (2015) 879–886. doi:10.1049/iet-pel.2014.0593.

[33] F. Nejabatkhah, Y.W. Li, B. Wu, Control Strategies of Three-Phase Distributed Generation Inverters for Grid Unbalanced Voltage Compensation, IEEE Transactions on Power Electronics. 31 (2016) 5228–5241. doi:10.1109/TPEL.2015.2479601.

[34] S.R. César A. Silva, Current reference strategy with explicit negative sequence component for voltage equalization contribution during asymmetric fault ride through, Int. Trans. Electr. Energ. Syst. 25 (2014) 3449–3471. doi:10.1002/etep.2045.

[35] O. Goksu, R. Teodorescu, C.L. Bak, F. Iov, P.C. Kjær, Impact of wind power plant reactive current injection during asymmetrical grid faults, IET Renewable Power Generation. 7 (2013) 484–492. doi:10.1049/iet-rpg.2012.0255.

[36] S.K. Chaudhary, R. Teodorescu, P. Rodriguez, P.C. Kjaer, A.M. Gole, Negative Sequence Current Control in Wind Power Plants With VSC-HVDC Connection, IEEE Transactions on Sustainable Energy. 3 (2012) 535–544. doi:10.1109/TSTE.2012.2191581.

[37] E.H. Camm, M.R. Behnke, O. Bolado, M. Bollen, M. Bradt, C. Brooks, W. Dilling, M. Edds, W.J. Hejdak, D. Houseman, S. Klein, F. Li, J. Li, P. Maibach, T. Nicolai, J. Patino, S.V. Pasupulati, N. Samaan, S. Saylors, T. Siebert, T. Smith, M. Starke, R. Walling, Wind power plant grounding, overvoltage protection, and insulation coordination: IEEE PES wind plant collector system design working group, in: 2009 IEEE Power Energy Society General Meeting, 2009: pp. 1–8. doi:10.1109/PES.2009.5275327.

[38] E. Muljadi, N. Samaan, V. Gevorgian, J. Li, S. Pasupulati, Different Factors Affecting Short Circuit Behavior of a Wind Power Plant, IEEE Transactions on Industry Applications. 49 (2013) 284–292. doi:10.1109/TIA.2012.2228831.

[39] A.A. Rockhill, M. Liserre, R. Teodorescu, P. Rodriguez, Grid-Filter Design for a Multimegawatt Medium-Voltage Voltage-Source Inverter, IEEE Transactions on Industrial Electronics. 58 (2011) 1205–1217. doi:10.1109/TIE.2010.2087293.

[40] P. Rodríguez, R. Teodorescu, I. Candela, A.V. Timbus, M. Liserre, F. Blaabjerg, New positive-sequence voltage detector for grid synchronization of power converters under faulty grid conditions, in: 2006 37th IEEE Power Electronics Specialists Conference, 2006: pp. 1–7. doi:10.1109/pesc.2006.1712059.

[41] Pedro Rodriguez, Alvaro Luna, Ignacio Candela, Ramon Mujal, Remus Teodorescu, Frede Blaabjerg, Multiresonant Frequency-Locked Loop for GridSynchronization of Power Converters UnderDistorted Grid Conditions, Trans. Indust. Electro. 58 (2010) 127–138. doi:10.1109/TIE.2010.2042420.

[42] Amirnaser Yazdani, Reza Iravani, Voltage-Sourced Converters in Power Systems : Modeling, Control, and Applications, Wiley-IEEE Press, 2010.

[43] R. Teodorescu, F. Blaabjerg, M. Liserre, P.C. Loh, Proportional-resonant controllers and filters for grid-connected voltage-source converters, IEE Proceedings - Electric Power Applications. 153 (2006) 750–762. doi:10.1049/ip-epa:20060008.

[44] V.F. Mendes, C.V. de Sousa, W. Hofmann, S.R. Silva, Doubly-fed induction generator ride-through fault capability using resonant controllers for asymmetrical voltage sags, IET Renewable Power Generation. 9 (2015) 783–791. doi:10.1049/iet-rpg.2014.0373.

[45] H.D. Tafti, A.I. Maswood, G. Konstantinou, J. Pou, F. Blaabjerg, A General Constant Power Generation Algorithm for Photovoltaic Systems, IEEE Transactions on Power Electronics. 33 (2018) 4088–4101. doi:10.1109/TPEL.2017.2724544.

[46] R.M. Silva, F.F.V. Matos, J.L. Silva, W.W.A. Gonçalves, G.M. Rezende, C.V. Souza, V.F. Mendes, Parameter determination of permanent magnet synchronous machine and sensorless algorithm implementation based on sliding mode observer, in: 2018 Simposio Brasileiro de Sistemas Eletricos (SBSE), 2018: pp. 1–7. doi:10.1109/SBSE.2018.8395767.

[47] V.F. Mendes, F.F. Matos, S.Y. Liu, A.F. Cupertino, H.A. Pereira, C.V. De Sousa, Low Voltage Ride-Through Capability Solutions for Permanent Magnet Synchronous Wind Generators, Energies. 9 (2016) 59. doi:10.3390/en9010059.

[48] J.F. Conroy, R. Watson, Low-voltage ride-through of a full converter wind turbine with permanent magnet generator, IET Renewable Power Generation. 1 (2007) 182–189. doi:10.1049/iet-rpg:20070033.

[49] IEEE Recommended Practice for Monitoring Electric Power Quality, IEEE Std 1159-2009 (Revision of IEEE Std 1159-1995). (2009) c1-81. doi:10.1109/IEEESTD.2009.5154067.

[50] M.H.J. Bollen, Characterisation of voltage sags experienced by three-phase adjustable-speed drives, IEEE Transactions on Power Delivery. 12 (1997) 1666–1671. doi:10.1109/61.634188.

[51] F.Z. Peng, J.-S. Lai, Generalized instantaneous reactive power theory for three-phase power systems, IEEE Transactions on Instrumentation and Measurement. 45 (1996) 293–297. doi:10.1109/19.481350.

[52] L.S. Czarnecki, Orthogonal decomposition of the currents in a 3-phase nonlinear asymmetrical circuit with a nonsinusoidal voltage source, IEEE Transactions on Instrumentation and Measurement. 37 (1988) 30–34. doi:10.1109/19.2658.

[53] Y. Yang, K. Ma, H. Wang, F. Blaabjerg, Instantaneous thermal modeling of the DC-link capacitor in PhotoVoltaic systems, in: 2015 IEEE Applied Power Electronics Conference and Exposition (APEC), 2015: pp. 2733–2739. doi:10.1109/APEC.2015.7104737.

[54] H. Wang, F. Blaabjerg, Reliability of Capacitors for DC-Link Applications in Power Electronic Converters—An Overview, IEEE Transactions on Industry Applications. 50 (2014) 3569–3578. doi:10.1109/TIA.2014.2308357.

[55] EPCOS, Film Capacitors:General Technical Information, (2009). https://www.tdk-electronics.tdk.com/en/web/%20generator/Web/Sections/ProductCatalog/Capacitors/FilmCapacitors/%20PDF/PDF__GeneralTechnicalInformation,property=Data__en.pdf;/PDF_GeneralTechnicalInformation.pdf.

[56] T. Hwang, S. Park, DC power ripple minimization of LCL filter based distributed generation inverter under unbalanced voltage conditions, in: 2013 Twenty-Eighth Annual IEEE Applied Power Electronics Conference and Exposition (APEC), 2013: pp. 321–328. doi:10.1109/APEC.2013.6520228.

Appendix A

CONTROLLERS PROJECT

Let the generic control loop presented in Fig. A.1.

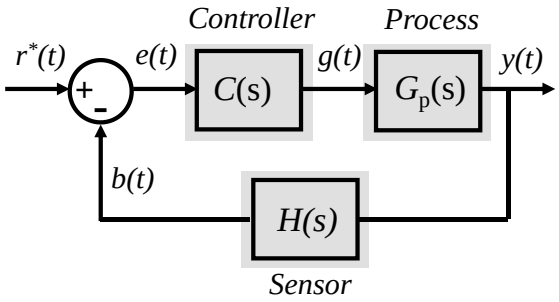

Fig. A.1: Generic control loop
Source: Elaborated by the author

- C(s) is the system control or compensator and its project will be discussed in this appendix.
- G_p(s) is the process or plant transfer function and it is the part of the system to be controlled.
- *H(s)* is the process sensor that converts the physical variables to a range or variable that can be processed by the controller.
- $r^*(t)$ is the control system reference or the desired process output.
- *g(t)* is the handled variable by the controller to obtain the desired response.
- *b(t)* is controller feedback
- *e(t)* is the error or the difference between the control variables and the control system reference.

Based in Fig. A.1, the closed loop transfer function is defined by:

$$T(s) = \frac{Y(s)}{R^*(s)} = \frac{G_p(s)C(s)}{1 + H(s)G_p(s)C(s)}. \quad \text{(A.1)}$$

The stability of a linear system is defined according to the poles (denominator equation roots) location in the in the *s* plane [A1]. Therefore, the stability margin of the control system (A.1) is defined by:

$$1 + H(s)C(s)G_c(s) = 0 \Longrightarrow H(s)C(s)G_c(s) = -1, \quad \text{(A.2)}$$

where $H(s)C(s)G_c(s)$ is the open loop transfer function, Rewriting the equation (A.2) in terms of modulus and phase, i.e.:

$$|H(s)C(s)G_c(s)| = 1, \tag{A.3}$$

$$\angle H(s)C(s)G_c(s) = \pm 180^o. \tag{A.4}$$

The equations (A.3) and (A.4) define the relative stability, that is, the limits where a linear control system becomes marginally stable. The transfer functions in control theory are approximate mathematical models to the physical phenomenon. Hence, due to inaccuracies in the mathematical model, it is desired that the control system not only be stable but also present stability margin [A1].

The controller design in this chapter is based on the frequency response, where the control loop behavior is evaluated to different frequencies sinusoidal inputs. Thus, the stability criterions are estimated using the bode diagram and the stability margin is related to the closeness to the point $|G(j\omega_{gc})| = 0$(db) in magnitude curve and $\angle G(j\omega_{pc}) = \pm 180^o$ in the phase curve, as demonstrated in the Fig. A.2(a) and Fig. A.2(b) respectively. Where ω_{gc} is frequency which the transfer function module becomes equal 1 or 0(db), and ω_{pc} is the frequency which the transfer function phase angle becomes equal to$\pm 180^o$.

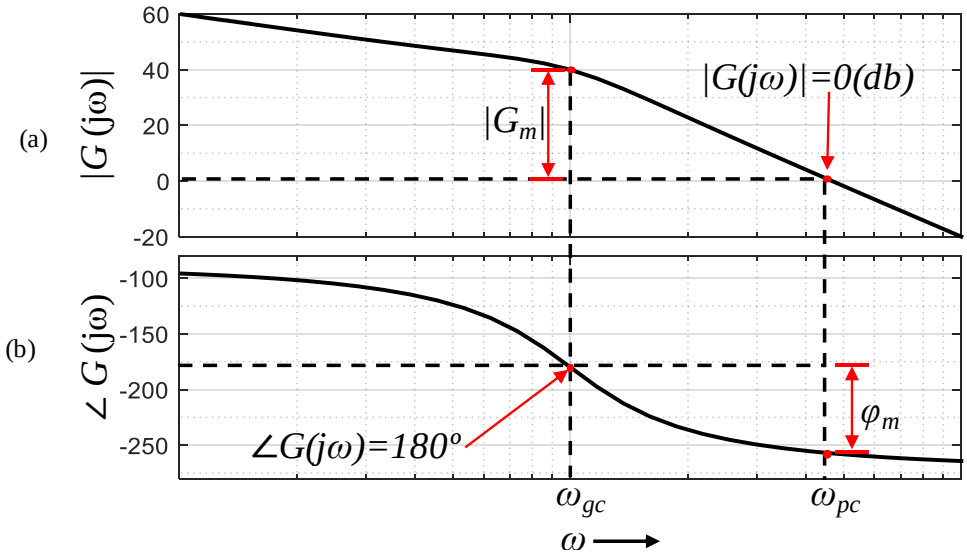

Fig. A.2: Open loop control frequency response
Source: Elaborated by the author

The purpose of the controller tuning is to designate the controller C(s) parameters, to impose in the open loop transfer function a certain phase margin ϕ_m at a given ω_{gc} frequency, that is:

$$\theta = -180^o + \phi_m + \angle H(j\omega_{gc})G_c(j\omega_{gc}) = \pm 180^o, \tag{A.5}$$

where θ is the lead or lag phase that the controller imposes to the control loop. Then, consider the standard second order transfer function:

$$G(s) = \frac{\omega_n}{s^2 + 2\zeta\omega_n\, s + \omega_n^2}, \tag{A.6}$$

where ζ is the damping coefficient, ω_n is the not-damped natural frequency. The temporal response of a second order system to a step input is described in Fig. A.3, where ov is the response overshoot and t_s is the settling time.

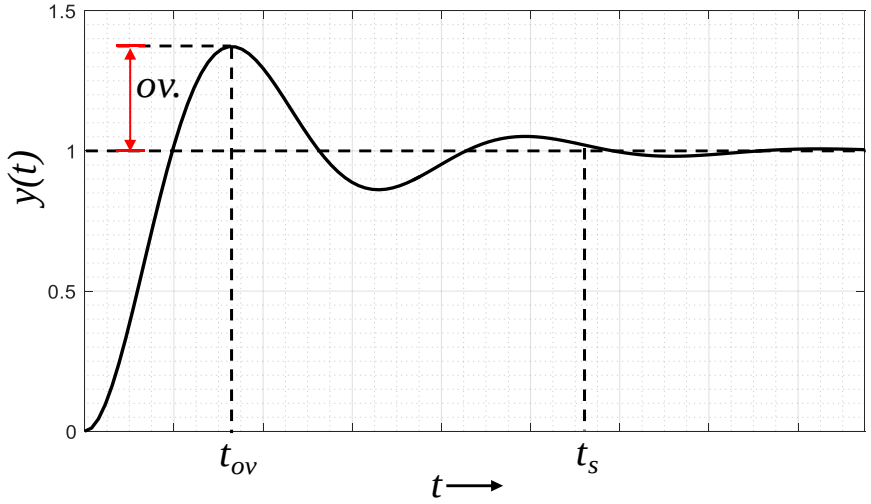

Fig. A.3: Second order system temporal characteristic response
Source: Elaborated by the author

Therefore, according to the reference [A1] is possible to establish a relationship between the relative stable margins and the temporal response characteristics, as follows:

$$\phi_m = \tan^{-1}\left(\frac{2\,\zeta}{\sqrt{\sqrt{4\,\zeta^4 + 1} - 2\,\zeta^2}}\right) \approx 100\,\zeta, \tag{A.7}$$

$$\omega_{gc} = \omega_n \sqrt{\sqrt{4\,\zeta^4 + 1} - 2\zeta^2} \approx \omega_n, \tag{A.8}$$

$$ov. = \exp\left(-\frac{\pi\,\zeta}{\sqrt{1-\zeta^2}}\right), \tag{A.9}$$

$$t_s = \frac{4}{\zeta\,\omega_n} = \frac{8}{\omega_{cg}\tan(\phi_m)}. \tag{A.10}$$

A.a Proportional-Integral controller tuning

Due to its simple implementation and well-behaved response, the PI (proportional integral) controller is one of the most employed in industrial process control systems, including in the

power electronic converters. The PI transfer function is defined in equation (A.11) where K_p is the proportional, and K_I is the integral gain.

$$C(s) = K_p + \frac{K_I}{s}, \tag{A.11}$$

Hence, from the previously established concepts, it is possible to develop a Matlab script that allows to calculate the PI controller gains according to the desired response criteria, as follows:

```
% Proportional integral controller project
%%
% ============================================================
% User entries
% ============================================================
% process trasfer function
Dp = xx;
Np = xx;
% sensor transfer function
Dh = xx;
Nh = xx;
% desired overshoor
ov = xx ;
% desired gain croosing frequency
wgc = xx;
% ================================================================== %
% minimum damping factor calculation
zeta = sqrt((log(ov))^2/(pi^2+(log(ov))^2));

% minimum phase margin calculation
phi_m = atand((2*zeta)/sqrt(sqrt(4*zeta^2+1)-2*zeta^2));

Gp  = tf(Dp,Np)   ; % process control transfer fnction
H   = tf(Dh,Nh)   ; % sensor transfer function
GMA = series(Gp,H); % open loop trnasfer fuction
                    % without compesation
% noncompesated system phase and magnitude in the
% desired crossing frequency
[Mag,ph] = bode(GMA,wgc);

% Compensator design
Mag_PI  =  1/Mag           ; % compesator agnitude
pha_PI  = -ph - 180 + phi_m; % compesator phase

tau_PI  = 1/(wgc) * tan((pha_PI+90)*pi/180);
Kpi     = Mag_PI * wgc/(sqrt(1+(wgc*tau_PI)^2));
Kp = Kpi * tau_PI; % proportional gain
Ki = Kpi         ; % Integral gain

Gc   = tf([Kp Ki],[1 0]) ; % Controller transfer function
GMAc = series(GMA,Gc);

opts = bodeoptions('cstprefs');
opts.FreqUnits = 'Hz';
```

```
figure()
bode(GMAc,GMA,opts)

T = Gp*Gc/(1+Gp*Gc*H);
figure()
step(T);
%%
```

PI controllers design routine
Source: Elaborated by the author

The control loops in power electronics converters normally are allocated in cascade. Thus, in order to guarantee the decoupling between their responses, the extern loop cut-off frequency must be ten-times slower than the inner loop.

It is worth to emphasizing that the values calculated through the equations developed routine do not ensure the controller pole dominance. Therefore, it is necessary to adjust the gains values in order to obtain a better response. Moreover, the controllers

A.b Resonant controller tuning

The PI controllers present a limited bandwidth, which is a significant drawback in the stationary frame control where the variables have frequencies different from zero in steady state.

Hence, to obtain a better dynamic response in steady state in the stationary frame, it will be used the proportional resonant (PR) controllers, since they can track arbitrary sinusoidal references in positive and negative sequence simultaneously, with zero steady state error. The damped PR transfer function is described in equation (A.13) [A2][A3].

$$C(s) = K_{Ih} \frac{\omega_b \, s}{s^2 + 2\omega_b + \omega_h^2} + K_p, \tag{A.12}$$

where K_{Ih} is the resonant gain, ω_b is the bandwidth and ω_h is the resonant frequency. In the resonance frequency the PR controller presents similar characteristics to a PI in relation to relative stability, consequently the controller tuning can follow a similar procedure to the earlier section.

In addition to the gains K_p and K_{Ih}, the bandwidth ω_b must be appropriately determined. Fig. A.4 shows the proportional resonant controller bode diagram for different bandwidth ω_b values. In the magnitude curve (Fig. A.4(a)) the increase of ω_b results in the compensation of larger range of frequency near to the resonance. In the phase curve (Fig. A.4(b)), near to the resonance point, small frequency deviations result in significant phase margin variations, which is improved with the increase of the ω_b. However, when it is used more than one PR controller, the bandwidth increase may cause the controllers response overlap, generating

stability problems. Thus the ω_b determination must take in account the phase margin deterioration (more than one controller) and frequency deviation that the controller can compensate.

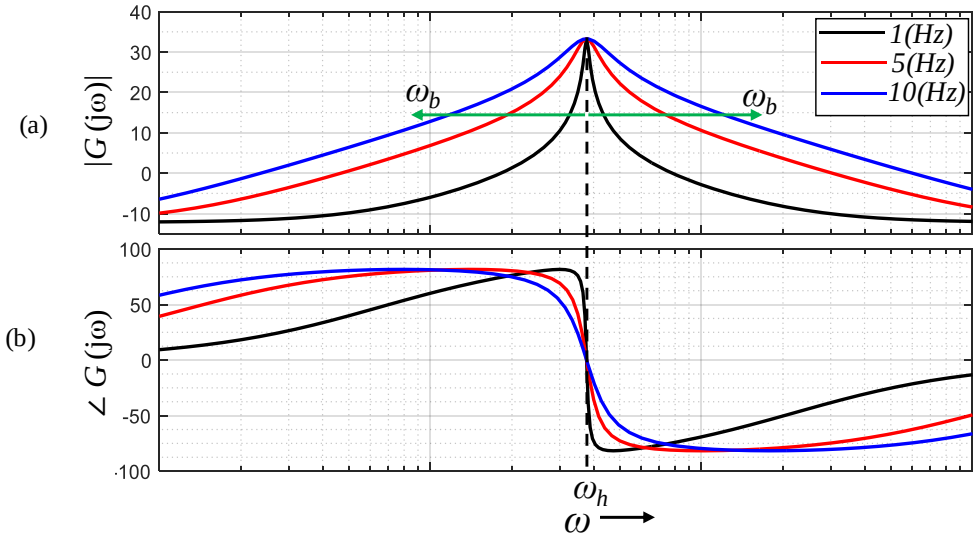

Fig. A.4: Resonant controller frequency response
Source: Elaborated by the author

A.c Controller discretization

A linear time-invariant system can be discretized through the mapping techniques of a continuous-time domain (s-plane) in a discrete time domain (z-plane). There are several mapping techniques and one of them is the bilinear transformation, defined in equations (A.13), where *Ts* is the sample-time. The bilinear transformation comes from the trapezoidal rule approximation, presenting a good matching between the system frequency response in continuous and discrete-time domain [A4].

$$s = \frac{2}{T_s}\frac{1 - z^{-1}}{1 + z^{-1}} \Leftrightarrow z = \frac{1 + (T_s/2)s}{1 - (T_s/2)s}, \tag{A.13}$$

. The relation between the s-plane and the z-plane, obtained through the bilinear transformation is shown in Fig. A.5, where $\omega_s = 2\pi/T_s$ is the sample frequency and Ω is the discrete unity-circle equivalent frequency.

- The imaginary axis in the *s*-plane is translated to the unity-circle bounds in the *z*-plane;
- The left ralph-plane corresponds to the inner of the unity-circle;
- The right ralph-plane corresponds to the outside to the unity-circle.

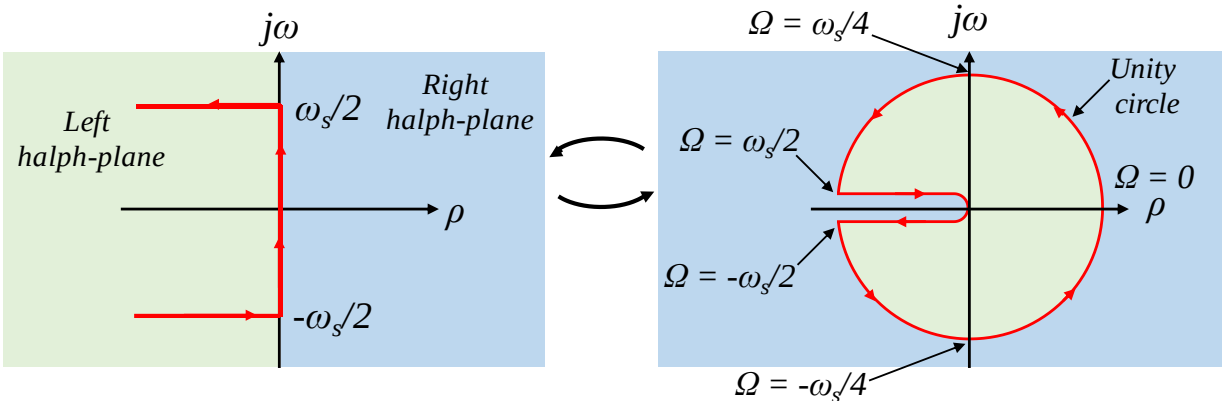

Fig. A.5: Bilinear mapping of s-plane in z-plane.
Source: Adapted from [A1]

The imaginary axis that comprises the interval $-\infty \leq \omega \leq \infty$ in the continuous-time domain, it is compressed to the interval $-\pi \leq \Omega \leq \pi$ in the discrete time domain. Thus, the relation between the continuous-time frequency ω and the discrete-time frequency Ω is not linear and it is defined by [A4]:

$$\omega = 2\,\mathrm{atan}\left(\frac{\Omega T_s}{2}\right) \Leftrightarrow \Omega = \frac{2}{T_s}\tan\left(\frac{\omega}{2}\right). \tag{A.14}$$

Therefore, in order to ensures the matching between the continuous and discrete-time system response in a specific frequency ω_d, it is necessary to use the frequency prewarping in the bilinear transformation, as follows.

$$s' = \frac{\omega_d}{\tan(\omega_d T_s/2)}\frac{1-z^{-1}}{1+z^{-1}} \tag{A.15}$$

A.c.i Proportional-integral controller discretization

The discretization of the proportional controller (equation (A.11)) results in the gain value:

$$C_p(z) = \frac{Y_p(z)}{E(z)} = K_p, \tag{A.16}$$

where $Y_p(z)$ and $E(z)$ are the proportional controller input and output (error) respectively. Thus, since $k \in \mathbb{Z}$, the proportional controller difference equation is given by:

$$y_p(k) = K_p\, e(k), \tag{A.17}$$

The integral controller (equation (A.11)) discretization is obtained through the bilinear transformation (equation (A.13)).

$$C_I(z) = \frac{Y_I(z)}{E(z)} = \frac{K_I\, T_s}{2}\frac{1+z^{-1}}{1-z^{-1}}, \tag{A.18}$$

$Y_I(z)$ is the integral output. The integral controller difference equation is given by:

$$y_I(k) = \frac{K_I\, T_s}{2}\big(e(k) + e(k-1)\big) + y_I(k-1), \tag{A.19}$$

The PI controller block diagram is presented in Fig. A.6.

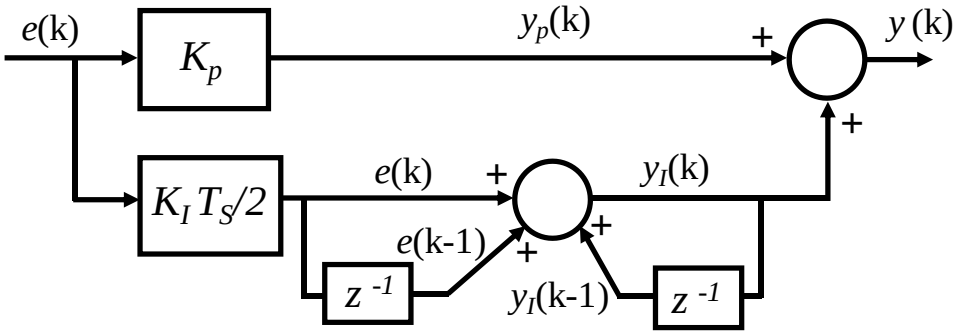

Fig. A.6: Discrete time PI controller block diagram.
Source: Elaborated by the author

A.c.ii Anti-wind-up implementation

In a large transition in the control system reference, the PI controller sill accumulates the error integration during all transient. Then, when a new set-point is established, the integral controller will be far from the actual reference and a transient overshoot will be generated.

The anti-wind-up is based on the dynamic saturation of the integral controller during the transitory operation. The proportional controller output is monitored and when its value becomes greater than the saturation limit L_p, the integral output is set to zero. The integration is resumed only when the proportional control falls below the saturation limit [A5].

The PI controller with anti-wind-up implemented in the present work was based in the algorithm presented in the reference [A5], where the discrete time block diagram is shown in Fig. A.7. The proportional (L_P) and integral (L_I) saturation limits relation is defined by the following equation.

$$L_I = L_P - \big(K_p\, e[k]\big). \tag{A.20}$$

A.c.iii Resonant controller discretization

Using $\sigma = \omega_d/\tan(\omega_d T_s/2)$ in the prewarping discretization (equation (A.15)) and replace it into the resonant part of the PR controller transfer function (equation (A.12)), the resonant controller discrete-time transfer function is given by:

$$C_R(z) = \frac{Y_R(z)}{E(z)} = \frac{a_2\, z^{-2} + a_1\, z^{-1} + a_0}{b_2\, z^{-2} + b_1\, z^{-1} + b_0}, \tag{A.21}$$

where:

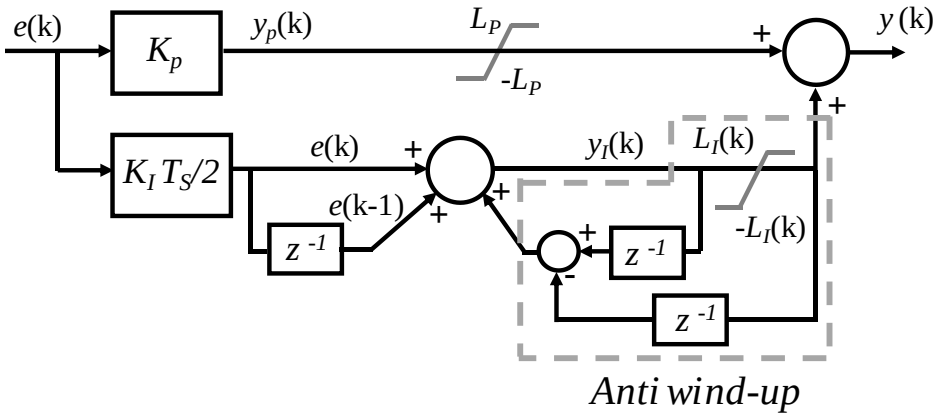

Fig. A.7: Discrete anti-wind-up diagram
Source: Adapted from [A5]

$$a_0 = -a_2 = \frac{2\sigma\omega_b K_{Ih}}{\sigma^2 + 2\sigma\omega_b + (9\omega_h)^2}, \qquad a_1 = 0. \tag{A.22}$$

$$b_1 = -b_2 = \frac{-2\sigma^2 + 2(\omega_h)^2}{\sigma^2 + 2\sigma\omega_b + (\omega_h)^2}, \qquad b_0 = 1.$$

A.d References

[A1] Charler L. Phillips, Royce D. Harbor. Feedback Control Systems. 3rd edition. Prentice Hall, 1996.

[A2] R. Teodorescu, F. Blaabjerg, M. Liserre, P.C. Loh, Proportional-resonant controllers and filters for grid-connected voltage-source converters, IEE Proceedings - Electric Power Applications. 153 (2006) 750–762.

[A3] Alejandro G. Yepes, Analysis and design of resonant current controllers for voltage-source converters by means of Nyquist diagrams and sensitivity function., IEEE Transactions on Industrial Electronics, v. 58, n. 11, p. 5231-5250, 2011.

[A4] A. V. Oppenheim, R. W. Schalfer. Discrete-time signal processing. 2nd edition. Pretience Hall, 1998.

[A5] Simone Buso, Paolo Mattavelli, Digital control in power electronics. 1st edition. Morgan & Claypool Publishers, 2006.

Appendix B

NON-SINUSOIDAL CURRENTS STRATEGIES

In this appendix is evaluated the harmonic content generated by the non-sinusoidal power control strategies in equations (3.13), (3.14), (3.20) and (3.21), for three different voltage sag situations.

In the first case, the voltages magnitude are $v_a = 1$(pu), $v_b = v_c = 0.6$(pu) resulting in $u = 0.182$, in the second $v_a = 1$(pu), $v_b = v_c = 0.4$(pu) with $u = 0.333$ and in the third one $v_a = 1$(pu), $v_b = v_c = 0.2$(pu) and $u = 0.571$.

The computational simulations were performed using scripts in the Matlab software. For the power saturation, reference [B1] proposes a generic scheme based on the IARC instantaneous conductance behavior, where the maximum current happens for the lowest voltage magnitude. Thus, the power set-points can be obtained by the equations (B.1) and (B.2), where I_q is the reactive current magnitude defined by the GC and I_p is the active current defined in (B.3), I_{rated} the system rated current.

$$Q^* = (V^+ - V^-)\, I_q, \tag{B.1}$$

$$P^* = (V^+ - V^-)\, I_p. \tag{B.2}$$

$$I_p = \sqrt{I_{rated}^2 - I_q^2} \tag{B.3}$$

B.a Instantaneous active and reactive power control (IARC)

For the IARC strategy, the currents vector paths are shown in Fig. B.1, they do not present a circular or elliptical shape, becoming more sinuous with the unbalance factor increasing. The currents vector irregular trajectory in the complex plane, increasing the harmonic distortion, which become more evident in the natural frame, as can be seen in the Fig. B.2(b). The active (Fig. B.2(c)) and reactive (Fig. B.2(d)) instantaneous powers **do not present oscillations**, even with simultaneous active and reactive power injection.

Finally, the IARC currents frequency spectrums are presented in Fig. B.3. The voltages unbalance results in the currents odd harmonics, mainly the third and fifth components, and the THD increases with the unbalance factor.

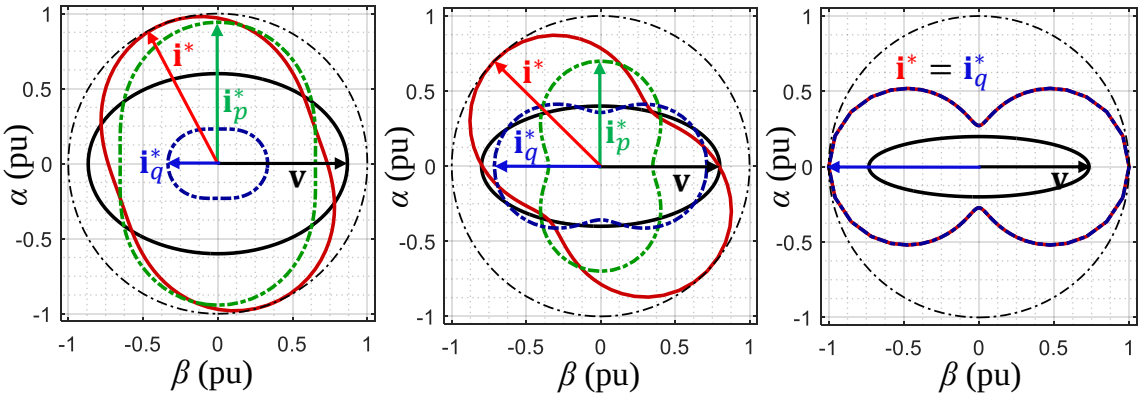

Fig. B.1: Current and voltage vector path during the voltage sag for (a) u = 0.182, (b) u = 0.333 and (c) u = 0.571 for IARC strategy.
Source: Elaborated by the author

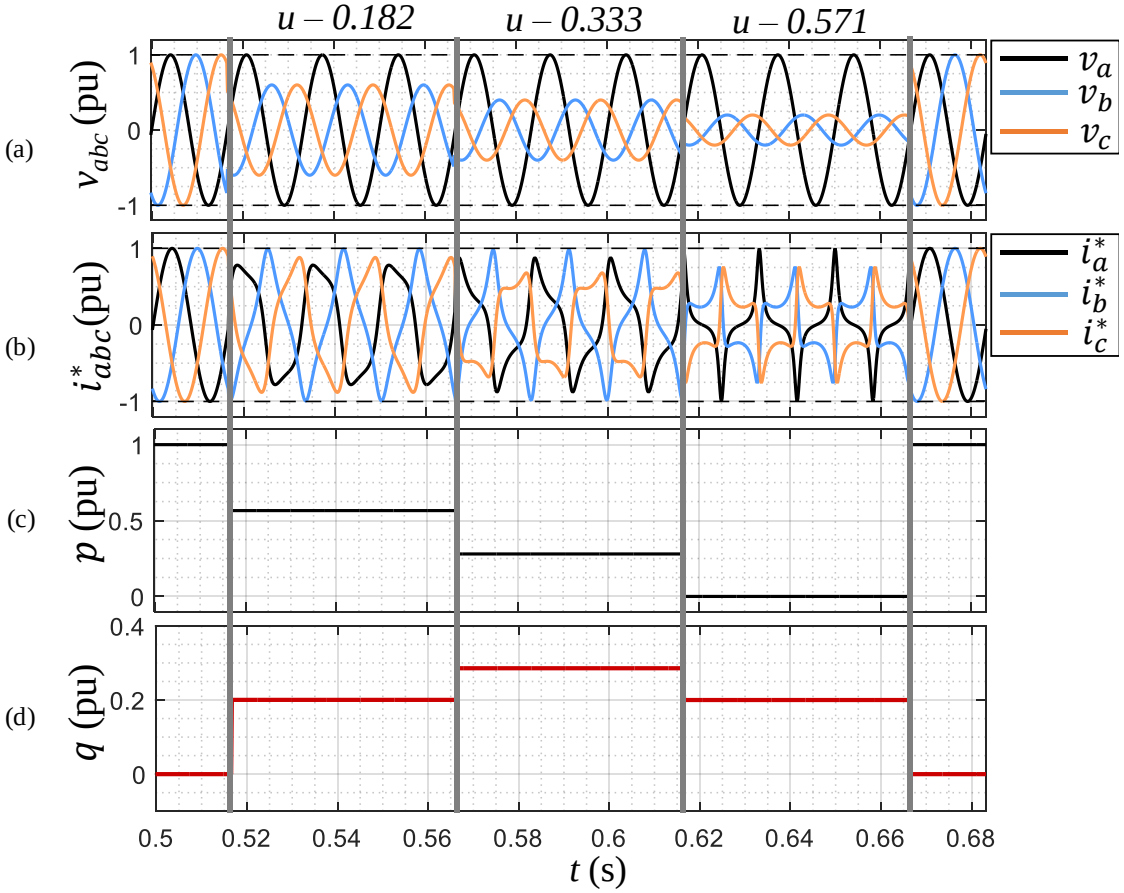

Fig. B.2: (a) voltages and (b) reference currents in natural frame, (c) active and (d) reactive instantaneous power for IARC strategy.
Source: Elaborated by the author

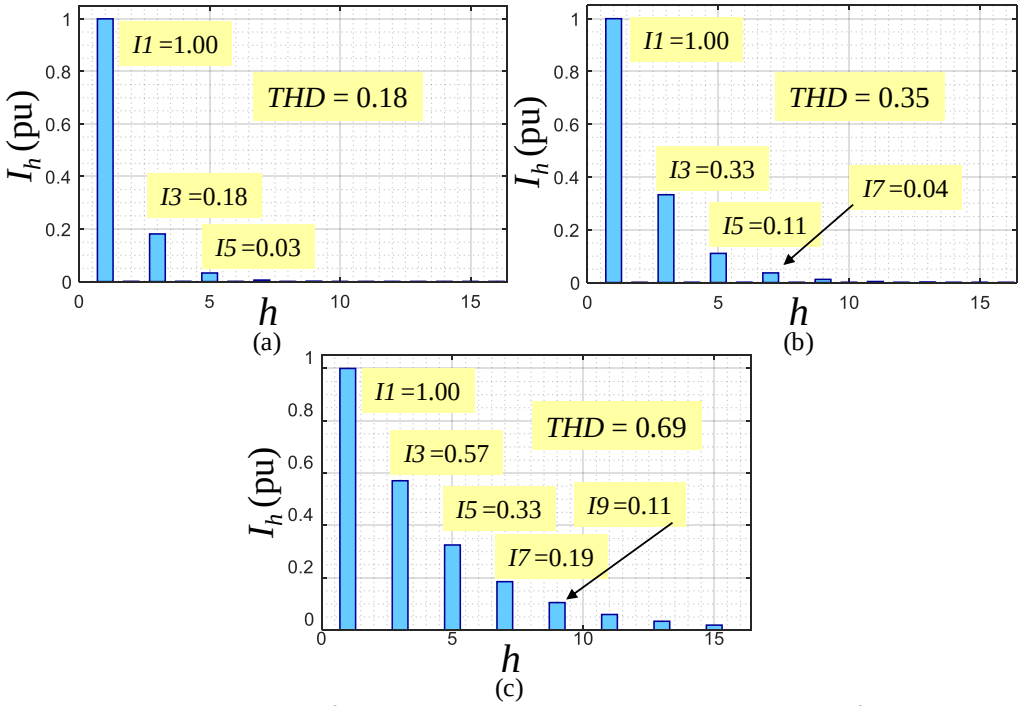

Fig. B.3: Harmonic distortion for (a) u = 0.182, (b) u = 0.333 and (c) u = 0.571 for IARC strategy.
Source: Elaborated by the author

B.b Instantaneously controlled positive sequence (ICPS)

The ICPS currents vector paths are shown Fig. B.4. Even only delivering currents through the positive sequence, they do not present a circular trajectory in the complex plane. The ICPS currents in Fig. B.5(b) present less irregular shape in relation to IARC. Moreover, the active (Fig. B.5(a)) and reactive (Fig. B.5(b)) power oscillation is not null and it is proportional to the orthogonal current component, i.e., active currents generates reactive power ripple and reactive currents generates active power oscillations. In the third case, where $u = 0.571$, since the active current is null, i.e., only reactive current injection, the ICSP does not present reactive power oscillations.

In Fig. B.6 it is possible to note that despite the high harmonic content the ICSP, it presents lower THD value in relation to the IARC in Fig. B.3. However, it cannot cancel the simultaneously active and reactive power oscillations.

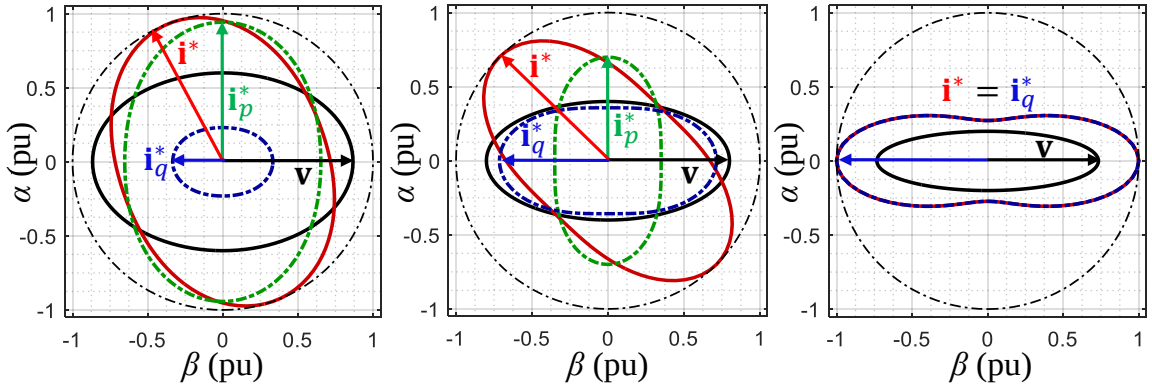

Fig. B.4: Current and voltage vector path during the voltage sag for (a) u = 0.182, (b) u = 0.333 and (c) u = 0.571 for ICPS strategy.

Source: Elaborated by the author

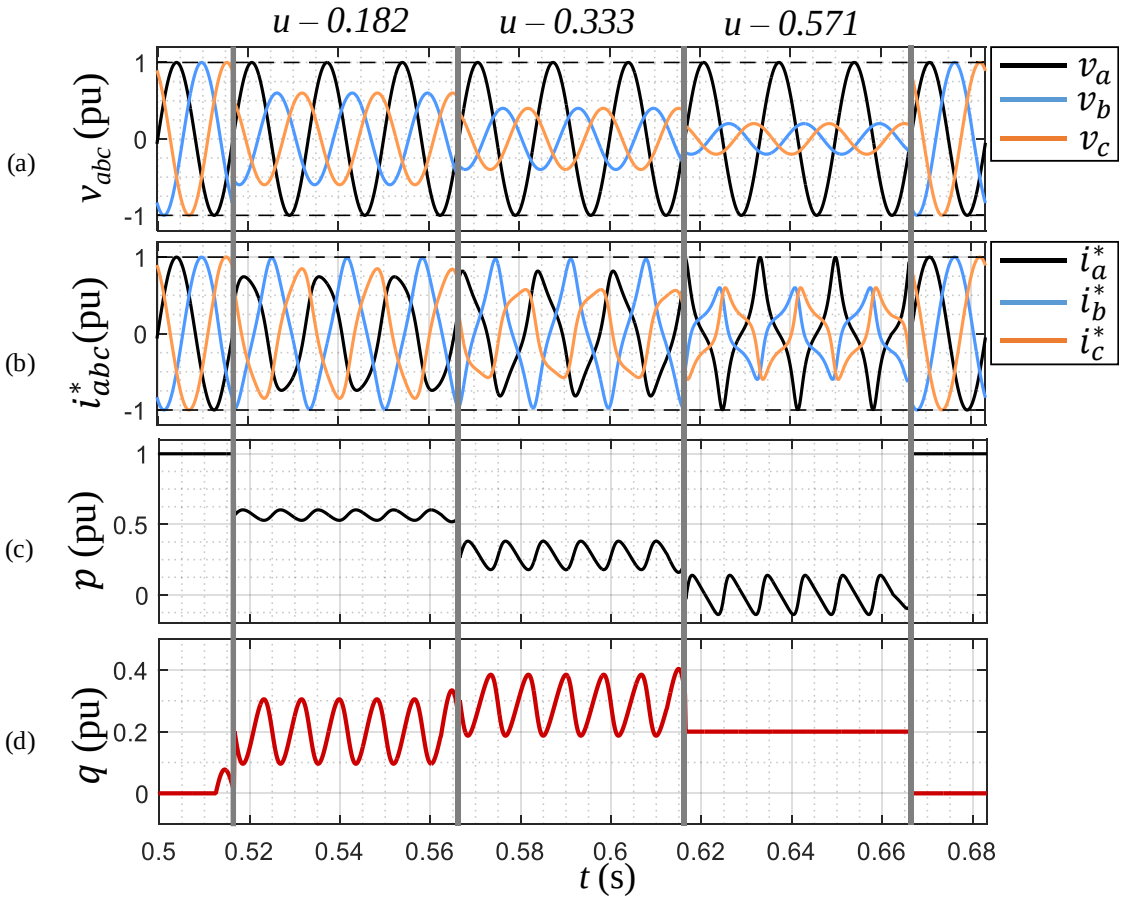

Fig. B.5: (a) voltages and (b) reference currents in natural frame, (c) active and (d) reactive instantaneous for ICPS strategy.

Source: Elaborated by the author

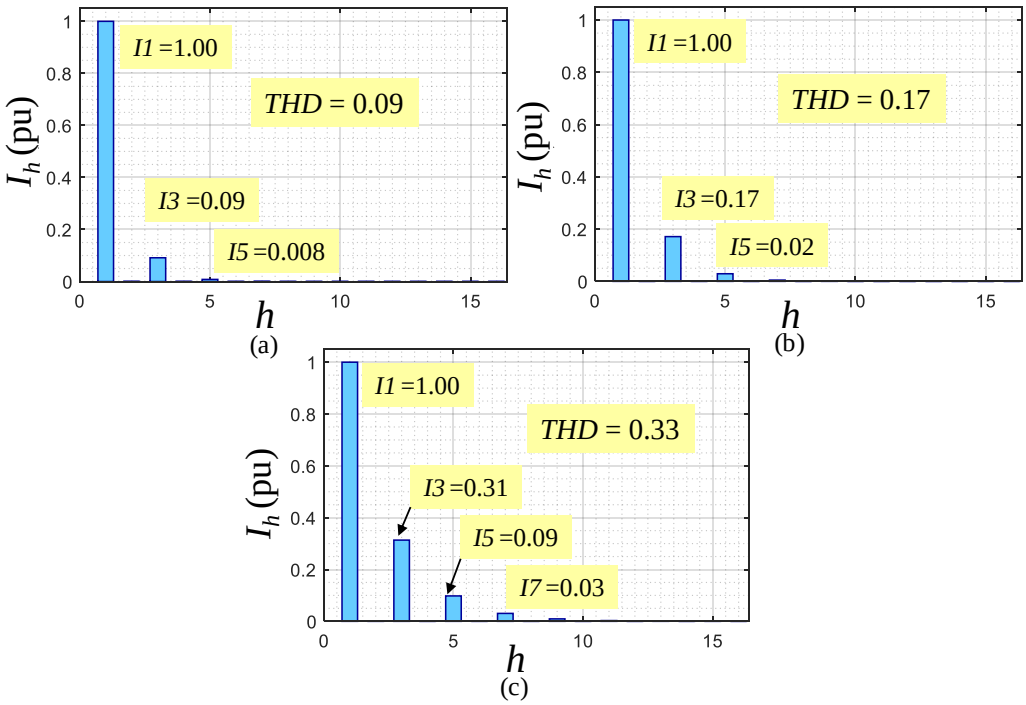

Fig. B.6: Harmonic distortion for (a) $u = 0.182$, (b) $u = 0.333$ and (c) $u = 0.571$instantaneous for ICPS strategy.

Source: Elaborated by the author

B.c Conclusions

Despite the power oscillation cancellation in IARC or reduction in ICSP, the control strategies with non-sinusoidal currents present relevant drawbacks:

- IARC and ICSP strategies generate multiple harmonics frequencies, requiring more complex control strategies such as multi-resonant structures.
- The capacity of harmonic currents synthesis is limited by the converter switching frequency, which is not high in multi-megawatts systems.
- The harmonic currents can generate resonances in the electrical mains or deteriorate the voltage at point of common coupling.

The technical limitations listed above shows that the implementation of power control with non-sinusoidal reference currents very difficult in multi-megawatts systems.

B.d References

[B1] C.H. Ng, L. Ran, J. Bumby, Unbalanced-Grid-Fault Ride-Through Control for a Wind Turbine Inverter, IEEE Transactions on Industry Applications. 44 (2008) 845–856. doi:10.1109/TIA.2008.921429.